UNIVERSITY OF CALGARY

Broadband Quantum Interface using a Thulium-doped Waveguide

by

Neil Sinclair

A THESIS

SUBMITTED TO THE FACULTY OF GRADUATE STUDIES

IN PARTIAL FULFILLMENT OF THE REQUIREMENTS FOR THE

DEGREE OF MASTER OF SCIENCE

DEPARTMENT OF PHYSICS AND ASTRONOMY

CALGARY, ALBERTA

September, 2010

UNIVERSITY OF CALGARY

FACULTY OF GRADUATE STUDIES

The undersigned certify that they have read, and recommend to the Faculty of Graduate Studies for acceptance, a thesis entitled "Broadband Quantum Interface using a Thulium-doped Waveguide" submitted by Neil Sinclair in partial fulfillment of the requirements for the degree of MASTER OF SCIENCE.

Supervisor, Dr. Wolfgang Tittel
Department of Physics and Astronomy

Dr. Alexander Lvovsky
Department of Physics and Astronomy

Dr. Nasser Moazzen-Ahmadi
Department of Physics and Astronomy

Dr. Yujun Shi
Department of Chemistry

Date

Abstract

Quantum communication allows one to perform tasks, such as provable secure key distribution, that are impossible in traditional communication. However, to increase the usefulness of implementations of quantum communication, the communication distance must be increased beyond its current limit of around one-hundred kilometers. To this end, a quantum memory must be constructed for use in a quantum repeater. This thesis concerns the spectroscopic characterization of a novel material candidate for quantum memory: a thulium doped lithium niobate waveguide cooled to 3 Kelvin. Furthermore, the possibility to reversibly transfer quantum states from sub-nanosecond, faint pulses of light in and out of this solid state device is demonstrated. This work extends the current benchmarks for storage bandwidth and multimode capacity, both required for high rate quantum communications. In addition, the integrated approach bridges the gap between fundamental and applied research into quantum memory.

Acknowledgements

Foremost, I want to thank all members of IQIS and PHAS who have made my time in graduate studies an enjoyable and fulfilling experience. This long list includes my classmates, colleagues, professors, students and the administration.

I also want to thank all the QC2 group members (for putting up with me) during my MSc. Each one of them has uniquely contributed to this thesis by offering me help both in and out of the lab. This includes: Michael Lamont, Xiaofan Mo, Chris Dascollas, Chris Healey, Itzel Lucio Martinez, Allison Rubenok, Randy Squires, Terence Stuart, Philip Chan, Steve Hosier, Vladimir Kiselyov, Sergey Moiseev, Thomas Apperley, Sean Blancher, Felix Bussieres, John Nguyen, Michael Underwood and Ahdiyeh Delfan. A special thank you goes to Daniel Oblak, Jeongwan Jin and Joshua Slater who have offered stimulating discussion while continually providing me with motivation during those all-night experiences, I mean experiments.

I especially want to thank Cecilia La Mela who has offered me exceptional guidance and patience. In addition, only her timeless work on the cryostat has made this thesis possible. Moreover, I am completely indebted to my colleague and friend Erhan Saglamyurek. His endless drive, willingness to educate, discuss, and provide help has been amazing during my MSc.

Of course, I want to thank my supervisor Wolfgang Tittel. Words cannot describe how lucky I feel to be working under such a supervisor. His endless energy, patience, guidance, motivation, and understanding is only saying too little of his character.

Most importantly, I want to thank my family and friends. They have always supported me and have been understanding of when I'm 'in the lab'.

Table of Contents

List of Figures

Chapter 1

Introduction

Quantum communication relies on exchanging quantum information encoded into quantum states between two (or more) parties. Robust communication is desired, so photons serve as the physical entity to encode the unit of quantum information: the qubit (shortened from quantum bit). Different photonic degrees of freedom can be exploited to encode qubits; these include polarization, frequency and time. For example, a qubit can be represented by a superposition of left and right circular polarization states. Considering transmission of photons through optical fiber, polarization fluctuations can occur in the channel due to environmental changes like temperature. Thus information may be scrambled upon transmission. It is then advantageous to construct a qubit by encoding a photon into a superposition of wavepackets that are localized in two temporal modes or 'bins'. This so-called time-bin qubit is used in this work.

1.1 Quantum key distribution

An important and widely researched application of quantum communication is quantum key distribution, which promises information-theoretic secure communication [1]. Its principles rely on axioms of quantum physics which include: (i) a measurement on a quantum system can not be done without perturbing it, (ii) an unknown quantum state can not be cloned perfectly [2], and (iii) nonorthogonal quantum states can not be distinguished perfectly. In quantum cryptography, two parties, usually called Alice and Bob, establish a shared secure key that they use for encrypting secret messages. To distribute the key, Alice encodes information into nonorthogonal quantum states (say, time-bin

qubits) and sends them to Bob. An eavesdropper cannot gain information without being caught by intercepting and measuring these states via principles (i) and (iii), and cloning will not assist the adversary by principle (ii). After the exchange of the photons, Alice and Bob verify the presence of the eavesdropper by comparing a randomly chosen subset of their data. Perturbed data received by Bob means that the information has not been secretly transferred and the presence of the eavesdropper is revealed. Succinctly, no perturbation means no eavesdropping. Afterwards, classical communication is employed between Alice and Bob to error-correct the key and to elimintate the key information shared with an adversary (i.e. privacy amplification). It should be noted that loss of data due to channel attenuation leads to the same result as discarding perturbed states, since consequences of both mean a reduction in secret key (production) rate.

Security of currently used classical ciphers relies on the assumption that an adversary has limited computational power. The result of using one-way functions, such as the multiplication of large prime numbers, constricts the eavesdropper to obtain little information about encrypted messages since factoring larger numbers grows exponential in cost (e.g. by the time an eavesdropper were to computationally obtain useful information about a message, the message would be irrelevant, rendering this eavesdropping fruitless). The assumption of adversaries having limited computational power was undisputed enough to secure existing communications until 1994, when Peter Shor proposed an algorithm to factor large numbers on relevant timescales using a so-called quantum computer (one that uses quantum effects to perform computations unable to be performed by purely classical means). Quantum cryptography allows to circumvent the threat of quantum computers to existing secure communications. Interestingly, by harnessing quantum means to break codes, the same means can be used to secure them.

After a first proposal of quantum cryptography in 1984 by Charles Bennett and Gilles Brassard [3], various demonstrations employing photonic transmission through free-space

or optical fiber followed [1]. Many quantum cryptography schemes employ qubits encoded into faint laser pulses [4], others use 'entangled' photon pairs towards the same end [1, 5]. Next we will introduce entanglement and its relation to quantum key distribution.

Quantum mechanical superposition, the principle upon which qubits are derived, can be generalized to multiparticle systems. For the case of two qubits, this can lead to formation of a non-separable quantum state (i.e. information is lost when considering each qubit individually). Due to their peculiar non-local properties, entangled states have been subject to numerous fundamental theoretical and experimental investigations, which were triggered by the seminal papers by Einstein, Podolsky and Rosen in 1935 [6], and Bell in 1964 [7]. The amount of entanglement posessed by these states quantifies their interaction with an external system . For instance, if an eavesdropper tampered with an entangled state, the amount of insecure information can be quantified from its remaining entanglement. Of particular interest, are the maximally entangled, so-called Bell states [8]. It has been shown [9] and recently demonstrated [10] that symmetrically distributing entangled pairs, rather than directly transmitting faint pulses, can increase the distances reached by quantum cryptography.

For distances up to a hundred kilometers or so, channel attenuation is low enough to allow the arrival of qubits encoded into attenuated laser pulses or entangled photons. However for practical quantum links, say over 1000 km of fiber (where attenuation is 0.2 dB/km at 1550 nm) the qubit transmission probability would be 10^{-20}. Assuming ambitious 10 GHz pulse generation rates, this translates into transmission of one temporal qubit every 300 years- this is obviously impractical! In classical communication schemes, amplifiers are used to overcome loss and achieve long distance communication. However principle (ii) restricts one from using these means for extending quantum communication. One could imagine having stations along the channel in which the message is decoded and encoded again, however, the key would be known at each of the nodes and this would

allow security loopholes. However, using many pairs of Bell states, in a so-called *quantum repeater* architecture, one can extend the distance of quantum cryptography far beyond the status quo. The principles behind the quantum repeater, which includes a need for a quantum memory, will be discussed in the following section.

1.1.1 Quantum repeaters

To help understand the operation of a quantum repeater, assume for the moment that we have one pair of qubits in a known Bell state, and a single qubit in an unknown state. We can then make a joint measurement (a so-called Bell state measurement) on the single qubit and one qubit out of the entangled pair, i.e. we project the joint state onto the basis spanned by the four Bell states. This measurement allows teleporting the unknown quantum state from the single qubit onto the other qubit of the Bell pair [11]. Let's turn now to a case where the qubit to be teleported is entangled with another qubit, i.e. we have initially two maximally entangled pairs. The joint measurement on two qubits from different pairs then leads to entanglement between the two remaining qubits in one of the four Bell states. This is generally referred to as entanglement swapping or teleportation of entanglement [12]. Since the theoretical proposal, various experimental demonstrations having been reported in and out of the laboratory [13, 14].

Consider now a long distance L. The basic idea of the quantum repeater [15] is that entanglement over the distance L can be heralded by entanglement swapping, starting from two entangled pairs, each of which covers a link of only half the distance, $L/2$. Moreover, these entangled states can themselves be created starting from states covering a distance $L/4$ and so on. For long distances, the described protocol allows for much higher entanglement distribution rates than without a repeater.

An essential ingredient for implementing a quantum repeater is that one has to be able to store the created elementary entanglement until entanglement has been estab-

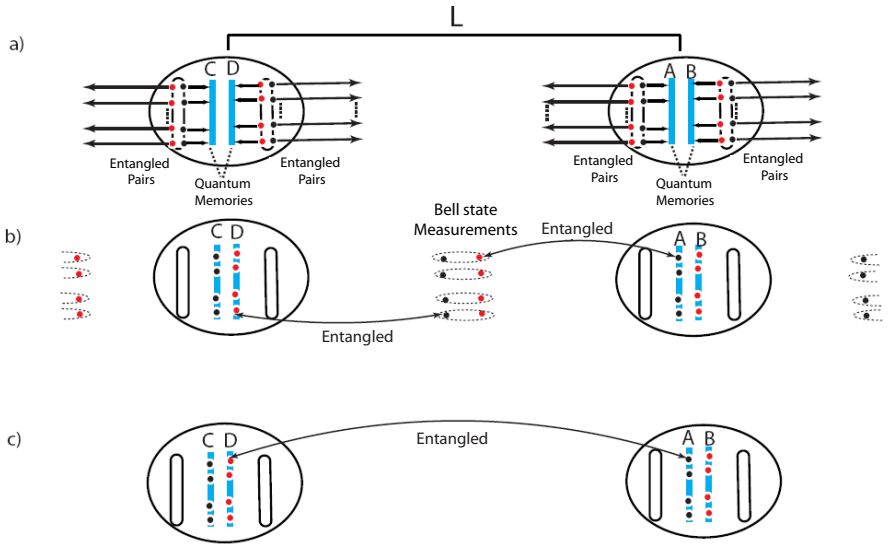

Figure 1.1: Possible implementation of a quantum repeater. a) each node has $2N$ sources of entanglement and two multimode quantum memories b) a Bell state measurement is done on two photons coming from neighboring nodes c) heralded entanglement is established between the photons stored in the memories.

lished in the neighboring link as well. This is required in order to be able to perform the required entanglement swapping operation. The resulting higher-level entanglement again needs to be stored until the neighboring higher-level link has been established and so on. Thus quantum repeaters require the existence of *quantum memories* [16, 17, 18]. If these memories are not available, one would need to create entanglement in all links simultaneously. Repeaters absent of memories, called 'quantum relays', therefore do not help to overcome the problem of channel losses as the swapping probability (and thus data rates) would decrease exponentially with the overall distance. Finally one has to be able to perform the required entanglement swapping operations between the quantum memories, i.e. each neighbouring memory releases its photon and then a Bell state measurement is performed on the pair. See Fig. 1.1. In addition the original Briegel repeater scheme contains 'entanglement purification' [19] steps that allow one to purify the effects of decoherence.

A popular proposal for realizing quantum repeaters is known as the DLCZ protocol after its authors Duan, Lukin, Cirac and Zoller [20]. DLCZ showed how to meet all the above requirements for a quantum repeater by using well-studied systems and processes: atomic ensembles as quantum memories, and linear optical techniques in combination with photon counting. In this proposal a laser 'writes' the memory, and produces a memory-photon entangled state. These photons are used in entanglement swapping, establishing the entangled memories. At this point, a 'read' pulse is used which causes each neighbouring memories to emit an entangled photon, which is then swapped.

In this scheme, and others that rely on probabilistic sources of entanglement, there is trade-off between the distribution rate and generation of high fidelity entanglement [21]. For higher rates there is a larger probability to create multi-pair states, which reduces the output state's useful entanglement. In order to suppress this effect, one must work with low emission probability, limiting the achievable distribution rate.

Using quantum memories that are capable of recalling multiple photonic qubits allows to increase the entanglement distribution rate over the repeater [21] since more possibilities of a successful Bell state measurement are allowed. To this end, one can use a source of Bell states beside a memory that allows on-demand storage and recall of (time multiplexed) photonic states. The idea is that one photon from the pair is stored in the memory, and the other is sent for swapping [22]. At this point, the memory recalls the stored entangled photon, which is then itself swapped. This emulates the DLCZ scheme but with the advantage that many temporal modes can be stored per round of swapping (i.e. incorporates multimode memories). This promises greatly improved distribution rates.

With this background in mind, the primary goal of this MSc project is to characterize and demonstrate a quantum light-matter interface towards use in a quantum repeater. This work will further one of the ultimate goals of my team in the quantum cryptography

and communication (QC2) laboratory- to construct and operate a practical quantum cryptography network using quantum repeaters. A natural question arises from this discussion: how does one know if a quantum memory is suitable to be incorporated into a quantum repeater? The next section addresses this question by introducing the reader to quantum memories and figures of merit which aid in assessing viability of a memory for extending quantum communication.

1.2 Optical quantum memory

A quantum memory serves essentially as a synchronization device in quantum repeaters. This characteristic also serves in linear optical quantum computing architectures where a quantum state is required to be delayed, for example until an array is filled or until the arrival of an input from a user. Interestingly, quantum memories have been shown to perform both storage *and manipulation* of quantum data [23, 24, 25] simultaneously. Most quantum memories are atomic based, since atoms can be spatially confined, and rely on the well-understood interfacing of light with matter. This interfacing could be interpreted in reverse, since excited atoms can also be used as deterministic single photon sources [26]. In addition, atom light interfaces have been used for precision measurements (e.g. for precise atomic clocks) [27]. These applications motivate research in understanding sometimes intricate quantum interactions between photons and atoms. Moreover, it gives a reason to study complicated dynamics of some promising atomic systems for a purpose other than spectroscopic cataloguing.

There are many different proposals for a quantum memory for light. Popularized for its ability to 'stop' light, electromagnetically induced transparency (EIT) has been explored to store pulses of light for seconds in praseodymium doped into Y_2SiO_5 [28]. Off-resonant schemes have been proposed and used for potential high speed repeaters [29].

Most proposals have used atomic ensembles in vapour or solids, although some work has been done with (single) atoms in cavities [30]. Other interesting system proposals include atoms in optical lattices [31], semiconductor quantum dots [32] and nitrogen-vacancy diamond centres [33].

An attractive proposal employs rare-earth ion ensembles doped into crystals and fibers [34]. These materials have been studied for uses in solid state lasers, fiber optical amplifiers, scintillators and lighting applications [35, 36]. These studies along with fundamental investigations [37] have provided a broad understanding of the structure and interactions of rare-earth-ion doped solids. These materials have static ions that, when cooled to cryogenic temperatures, have long coherence times. This results in a long storage time when used as a material for quantum memory. They also have inhomogeneously broadened absorption profiles, appropriate for storing very short photon pulses, which is required for high rate communications. The quantum storage mechanism in these materials is governed by the principle of the photon echo process [38, 39]. The idea behind photon echo is to utilize the inhomogeneously broadened absorption profiles to store a pulse of light in a collective atomic ensemble state. Once photons are absorbed by the ensemble the created atomic macroscopic dipole moment begins to dephase due to the inhomogeneous broadening. Photons can be recalled by forcing all individual absorbers to rephase so that the intial macroscopic dipole moment is recreated causing emission of light. This emitted radiation is called an echo. In its original form, photon echo protocols suffer limitations when applied to single photon storage. However, modified versions suitable for storage and recall of quantum states have been proposed and recently realized [40, 41]. This work studies photon echo quantum memory using thulium ions doped into lithium niobate crystal waveguides. In chapters two and three we will introduce more details pertaining to this material and our approach taken towards quantum state storage.

It is important to realize that all of the above mentioned systems have yet to allow a demonstration of a fully functional quantum memory, since each proposal can only satisfy certain subset of properties that quantum memories require. Approaches with rare-earths have been promising, for example achieving long storage times and paramount efficiencies (69%) [42]. In the next section, we discuss the requirements a quantum memory should have to be considered in a quantum repeater.

1.2.1 Figures of merit

With inspiration from Ref. [43] we now discuss a number of figures of merit (evaluation criteria) for a quantum memory for light in a quantum repeater. Of course, criteria can vary depending on the quantum repeater protocol. In the following discussion, we look to identify lower bounds on each of the relevant figures of merit. This is not a straightforward task, however, as many criteria are interrelated and research towards creating robust quantum repeaters is still ongoing. Consider the following criteria a quantum memory must have to implement a quantum repeater:

- On-demand readout
- Wavelength
- Storage time
- Efficiency
- Bandwidth
- Multimode capacity
- Fidelity
- Robustness and simplicity

On-demand readout: A quantum memory must have on-demand readout capabilities. In other words, one must be able to trigger the memory to release its stored quantum state. The on-demand property is required because in a quantum repeater, the storage time of a quantum state varies depending upon establishment of entanglement in a neighbouring link.

Wavelength: It is important that memories have wavelengths matching those of available sources of entanglement. In turn, this may limit the wavelengths available for distribution of photons between the links (e.g. determined by pumping laser and energy conservation for sources based upon spontaneous parametric down-conversion). As to avoid unnecessary propagation loss the wavelength of the transmitted photons must be within the region of low absorption in optical fibers (around 1550 nm) or free space (around 800 nm). Conveniently, single photon sources are available at these wavelengths [44]. Moreover, highly efficient and low noise single photon detectors that operate at the mentioned wavelengths are required (in Bell state measurements) to achieve reasonable distribution rates, and hence data rates (e.g. secret key rate) [21].

Storage time: To assess this criteria, consider the communication time between ends of a repeater. This imposes a lower bound on the required storage time. Fig. 1.1 presents a repeater scheme where a source of entangled pairs is sitting directly adjacent to a memory. A distance L away sits the other repeater node with the same configuration. Now, one photon from each entangled pair must be stored in the memory for at least a time needed for each free photon to travel, at the speed of light c, half way towards the adjacent node, where a Bell state measurement takes place, plus the time required for classical information regarding the outcome of the entanglement swap to travel back to the memory node.

$$t_{min} = \frac{L/2}{c} + \frac{L/2}{c} = \frac{L}{c} \tag{1.1}$$

For segments of length $L = 300$ km, t_{min} is one millisecond. Keep in mind we have neglected any delays related to entanglement purification procedures or classical data processing times. In light of multimode availability and material limitations on storage time, seconds storage time are currently sought for long distance communication.

Efficiency: When a photon is sent to be stored by the memory, the probability for a quantum memory to absorb and release a photon is denoted as the efficiency. To bound the minimum efficiency on a link containing a memory compared to that without one, consider a quantum relay where entanglement sources are placed at the centre of each segment. The probability, P, of a successful entanglement distribution is governed by the transmission loss of the channel, giving $P = 10^{\frac{-\alpha L_0}{10}}$. The channel length is L_0 with attenuation $\alpha = 0.2$ dB/km. Having a memory, each with efficiency η, at each adjacent node storing an entangled photon would happen with efficiency η^2. Therefore a repeater would serve as a benefit over conventional distriubtion if $\eta^2 > 10^{\frac{-\alpha L_0}{10}}$. For L_0 = 50 km and $L_0 = 200$ km of telecom fiber, the minimum efficiency would be 32% and 1% respectively. However, by considering full repeater schemes in detail, recent studies [21] have shown that greater than 90% memory efficiency must be employed to achieve reasonable key rates over long distances.

Bandwidth: Considering high data rate quantum communications exploiting only temporal degrees of freedom, the qubit's temporal duration Δt should match the limitations of current technology (i.e. $<$ 1 ns). Small temporal durations of the qubits cause them to have a large bandwidth $\Delta\omega$ since $\Delta\omega \propto \frac{1}{\Delta t}$. In order for the memory to store a state with 500 ps duration, the memory bandwidth must cover the spectrum of the input qubit, thus a memory bandwidth of 2 GHz would suffice. It is important to consider matching source and memory bandwidth when constructing sources of entangled photons (e.g. via parametric down-conversion), and to facilitate maximal spectral overlap with other components in a repeater.

Multimode capacity: The capacity to store several modes is a natural capability for certain ensemble implementations (e.g. in certain quantum memory protocols using rare-earth ions doped into crystals). As discussed, robust quantum repeater schemes are based on the assumption of having multimode memories that allow storage and retrieval of many temporal modes. Consider the probability of successful entanglement distribution of one entangled particle in a segment of a repeater to be P_1. The probability of a successful entanglement distribution using a multimode memory will be $1-(1-P_1)^N \approx NP_1$ for N qubit modes. Since P_1 decreases exponentially with increasing channel length, one needs N to increase significantly to achieve $NP_1 \sim 1$ for long distance communications. In addition, each mode must be recognizable and all N should be absorbed into the memory within a time shorter than the storage time. This causes an interrelation between multimode capacity, storage time and bandwidth. For a given storage time, the memory bandwidth must increase with increasing N. Another view is to have the bandwidth constant, but the storage time must increase with N. To increase multimode capacity, each of these approaches will be limited by the material properties of the memory. Studies have assumed hundreds or so of modes in simulations to produce reasonable distribution rates [21].

Fidelity: The precise meaning of the fidelity depends on the specific approach to quantum state storage. For memories that store and re-emit single photons (what we consider in this work) the fidelity, F, is defined as the overlap between the quantum state that is written into the memory and the state that is read out, averaged over all possible input states.

$$F = \Sigma_i p_i Tr_i(\rho_i^{in}\rho_i^{out}) \tag{1.2}$$

Here ρ_i^{in} and ρ_i^{out} denote the density matrix of the input and output states respectively, and p_i is the probability of having ρ_i^{in} as the input state. This is also denoted conditional (or post-selected) fidelity, because it is conditional on the re-emission a photon, not to be

confused with the efficiency (the probability to actually recover a photon). For memories that are meant to store general states of light, such as squeezed states, the conditional fidelity is not an appropriate concept, and one has to consider unconditional fidelities.

A lower bound for the fidelity of the quantum memory can be obtained by comparing it with the best classical strategy for storing quantum states. The classical strategy consists of a measurement on the quantum state, storage of the classical information corresponding to the outcome of the measurement and finally optimal reconstruction of the quantum state. On average, the maximum fidelity for the best classical strategy for qubits has been derived to be $F_{class} = \frac{2}{3}$ [45], thus a quantum memory must have a state with output fidelity higher than this value.

Another relevant lower bound on the fidelity is derived from the possibility to (imperfectly) clone an arbitary qubit state. We consider here the case where one qubit is cloned into two. For instance, a quantum memory could require the output state fidelity to be greater than a bound established by an optimal symmetric universal cloning machine. Note that there are other cloning machines, such as the phase covariant cloner, but this is the most universal one. To be precise, optimal and universal defines a strategy which maximizes the the average fidelity of the clones over all possible input qubit states, while symmetric implies that both clones have the same fidelity with the input qubit. Using this approach the maximum fidelity is $F_{clone} = \frac{5}{6}$.

This bound is not a purely theoretical construct as one can achieve this fidelity using an excited atomic ensemble of two level atoms (e.g. erbium amplifiers) [46]. It is interesting to consider the link between cloning machines, atoms and memories in this context. Furthermore, it has been shown when examining output state fidelities using conventional photon echoes that the fidelity saturates the quantum-classical bound of 2/3 for two-pulse echoes, and is smaller when considering three-pulse echoes [47].

Robustness and simplicity To bring a quantum memory out of the lab and into a real-world quantum repeater, the memory must be highly robust, stable and of simple design. Quantum memories based upon rare-earth-ions doped into crystals offer some advantages over other systems. The memory is in the solid state, it can be cast into fibers or waveguides which are easily integrated with existing telecommunication equipment. Although requiring low temperatures, cooling methods are well understood and apparatus can be compactified.

1.3 This thesis

1.3.1 Motivation

As introduced above, the future of long distance quantum communication, quantum networks and linear optical quantum computation relies on the possibility to temporally store quantum information encoded into single photons. This task is generally pursued by means of reversible state transfer into and out of atoms.

Studying rare-earth-ions doped into waveguide crystals is beneficial as waveguides can be easily integrated with optical fibers and current network infrastructure. Rare-earth ion doped crystals have both a well-studied past as well as many avenues to explore still unexplained possible interactions. Interestingly, the 'mix-and-match' flexibility of combining rare-earths in different hosts lead to a vast palette of possibilites for memories with varying properties. For these reasons, a large amount of work remains to be done to characterize the spectroscopic properites of rare-earth crystals to assess their suitability for quantum memory.

In this thesis, we first focus on characterizing a novel device, a thulium-doped lithium niobate waveguide, for a quantum memory. This material combines interesting features from the rare-earth dopant, the host material and the waveguide structure. After this

characterization, we demonstrate the material as a first light-atom quantum interface at the single photon level in a waveguide. Moreover, this study serves as a first demonstration of a challenging 1 GHz-bandwidth interface and storage of 128 modes of weak coherent pulses.

1.3.2 Organization

This thesis is organized as follows.

The coherent interaction between two-level atoms and light is introduced in chapter two. Along with a theoretical foundation, the chapter also describes the methods of spectral hole burning and traditional photon echoes. These techniques are used to study material properties. This section also describes photon echo quantum memory protocols based on controlled reversible inhomogeneous broadening protocol (CRIB) and atomic frequency combs (AFC), the protocol used in this work. This includes how materials are prepared (e.g. through optical pumping) to implement these protocols.

Rare-earth-ions doped into crystals is introduced in chapter three. This includes the atomic level structure and broadenings of these levels. Interactions of these ions with static external fields is discussed. This will give a structure for understanding how we achieve light storage in these materials as well as introduce nomenclature.

Chapter four introduces the first part of the experimental work presented during this thesis. After a brief discussion of the waveguide fabrication, experimental setup and equipment, we move on to the spectroscopic characterization of a thulium doped lithium niobate waveguide (Ti^{4+}:Tm^{3+}:$LiNbO_3$). This involves measuremens of the inhomogeneous broadening, population relaxation dynamics, coherence properties and the Stark effect. This chapter also includes the part of the experimental work that demonstrates broadband data storage at the single photon level. First, classical data storage is shown using the AFC protocol. Next high fidelity storage of broadband weak coherent states

is shown, along with a demonstration of currently the largest number of simultaneously stored modes at the single photon level.

In chapter 5 a summary of the results is included along with considerations of the future directions.

Chapter 2

Light-matter interaction

This thesis involves studies of the interactions between coherent light and rare-earth ions doped into a crystalline host. For quantum state storage, it is imperative that the reversible mapping of quantum light to atomic ensembles is a coherent process as to preserve quantum information. In addition, photon echo quantum memory protocols rely on preparation of inhomogeneous broadening of the sample prior to implementing storage. This involves usually interaction of coherent laser light and atoms within the ensemble. In some cases, incoherent interactions take place, e.g. long-term laser interaction for optical pumping. It is necessary to understand both coherent and incoherent interactions, not only in the context of quantum memory, but also for spectroscopic measurements. Thus, light-matter interactions are key in understanding how information about atomic species is gained. These interactions are even more important in regards to the sample studied in this thesis, due to its highly coherent properties and sometimes intertwined mechanisms.

The coherent interaction of photons and two-level atoms in materials is described through the *Maxwell-Bloch equations*. Understanding the two-level model is enough to explain the basic interactions. The wave equation, derived from Maxwell's equations, describes electromagnetic field evolution through a polarized medium. The Bloch equations examine the evolution of a two-level atomic system coupled with applied fields. By combining the two equations, one has the ability to describe the evolution of the combined atom-photon system in the materials under study here. This theoretical framework is essential for describing photon echo based quantum memory protocols. It provides quantitative meaning to physical parameters which are measured through experiment and enables us to predict important values such as memory efficiency and fidelity.

Taking a more mathematically rigorous stance, the first section of this chapter derives the Maxwell-Bloch equations. We then turn back to a methodological approach to explain the light-atom interactions pertaining to spectroscopic measurements performed for studying thulium doped lithium niobate. The two important, and simple, measurement procedures, namely *spectral hole burning* and *photon echo*, are common ways to measure properties of any atomic system. Hole burning and photon echo experiments allow efficient extraction of population dynamics, coherence properties, level structures, effects from applications of external fields and more [48] by probing inside an inhomogeneous aborption line. Spectral hole burning can be used to selectively remove absorbers from an inhomogeneously broadened absorption line. This process, called *spectral tailoring*, is introduced as an application of hole burning.

Next we introduce the two pulse echo and stimulated echo protocols from which the topic naturally flows to introducing photon echo based quantum memory protocols. This is because the basis behind these protocols relies upon reversible dephasing of the optical atomic dipoles, which is at the heart of every photon echo protocol, classical or quantum. Description of these protocols provides the background necessary to interpret the main result of this work: a broadband demonstration of the AFC protocol at the single photon level.

2.1 Maxwell-Bloch equations

2.1.1 Maxwell's equation

The starting point for the description of light as an electromagnetic wave is the set of equations known as Maxwell's equations (see any advanced electromagnetics textbook, e.g. Ref. [49]). Rare-earth doped crystals typically contain no free currents or charges, thus Maxwell's equations can be simplified and combined (as described in Ref. [49]) into

a wave equation:

$$\nabla^2\mathbf{E} - \mu\epsilon_o\frac{\partial^2}{\partial \mathrm{t}^2}\mathbf{E} = \mu\frac{\partial^2}{\partial \mathrm{t}^2}\mathbf{P} \tag{2.1}$$

where $\mathbf{E}$ is the electric field. Vector quantites are denoted by bold font. Considering a travelling wave in one dimension (i.e. a laser pulse in a waveguide), the electric field can be written as

$$\mathbf{E}(z,\mathrm{t}) = \mathcal{E}(z,\mathrm{t})e^{-i(\omega_L \mathrm{t} - kz)}\hat{e} + \text{c.c.} \tag{2.2}$$

where z is the defined direction of propagation, $k = \omega_L/c$ is the wavenumber with c being the speed of light and laser frequency ω_L, $\hat{e}$ is the unit vector denoting the direction of the electric field, and $\mathcal{E}$ is the (complex) envelope amplitude. In the wave equation, $\mathbf{P}$ is the induced atomic polarization, and $(c/n)^2 = 1/(\mu\epsilon)$ where n and ϵ is the material index of refraction and permittivity, respectively.

Generally the envelope of a light pulse varies much more slowly than the field itself. For example, with a wavelength of 800 nm, the frequency of the electromagnetic oscillation is 375 THz, while the envelope changes at most GHz frequencies in this work i.e. 5 orders of magnitude slower. Thus the second order derivatives are very small compared to the first order. This gives a simplified form of the wave equation:

$$\frac{\partial}{\partial z}\mathcal{E} + \frac{n}{c}\frac{\partial}{\partial \mathrm{t}}\mathcal{E} = \frac{ik}{2\epsilon}\mathcal{P} \tag{2.3}$$

We will revisit this form of Maxwell's equation after we combine it with the Bloch equations, which are introduced next.

2.1.2 Bloch equations

After looking at the interactions from the point of view of the light field propagating in a polarized medium, we turn to the Bloch equations which describe an intuitive picture of atomic evolution. We begin by defining an arbitrary pure state of a two-level atomic

system:

$$|\psi(\mathrm{t})\rangle = c_g(\mathrm{t})|g\rangle + c_e(\mathrm{t})|e\rangle \tag{2.4}$$

where $|c_g|^2$ and $|c_e|^2$ are the probabilities of finding the atom in the ground $|g\rangle$ and excited $|e\rangle$ states, respectively. In general, this state can be represented by a density matrix, $\rho(\mathrm{t})$:

$$\rho(\mathrm{t}) = |\psi\rangle\langle\psi| = \begin{pmatrix} \rho_{11} & \rho_{12} \\ \rho_{21} & \rho_{22} \end{pmatrix} = \begin{pmatrix} |c_g|^2 & {c_g}^* c_e \\ c_g {c_e}^* & |c_e|^2 \end{pmatrix} \tag{2.5}$$

The diagonal elements correspond to the population distribution within the levels and the off-diagonals describe the degree of coherence between the levels. To relate the density operator to the Bloch sphere picture, we need to define a Bloch-vector, $\mathbf{r(t)} = \sum_i^3 r_i(\mathrm{t})\hat{e}_i$, specified by the three components:

$$\begin{aligned} r_1 &= \rho_{21} + \rho_{12} = 2Re(\rho_{12}) \\ r_2 &= -i(\rho_{12} - \rho_{21}) = 2Im(\rho_{12}) \\ r_3 &= \rho_{22} - \rho_{11} \end{aligned} \tag{2.6}$$

The vectors r_1 and r_2 correspond to the coherence created between the excited and ground states, while r_3 quantifies the transparency (or inversion) of the medium. Since the state of the atomic system is defined by Bloch-vectors, changes in the state can easily be depicted graphically. For example, as shown in Fig. 2.1 an equal superposition state is given by the vector lying in the equator of the sphere, and a completely mixed state lies at the centre of the sphere. The completely mixed state $\rho_m = \frac{1}{2}|e\rangle\langle e| + \frac{1}{2}|g\rangle\langle g|$ lacks coherence information and describes a situation where population is equally distributed between the excited and ground states.

The atomic state, described by the Bloch-vector, is governed by the coupling between the atom, given by the transition dipole moment $\hat{\boldsymbol{\mu}}$, and the external light field $\mathbf{E}(\mathrm{t})$. In the semi-classical interpretation, the energy of this interaction is quantified by the

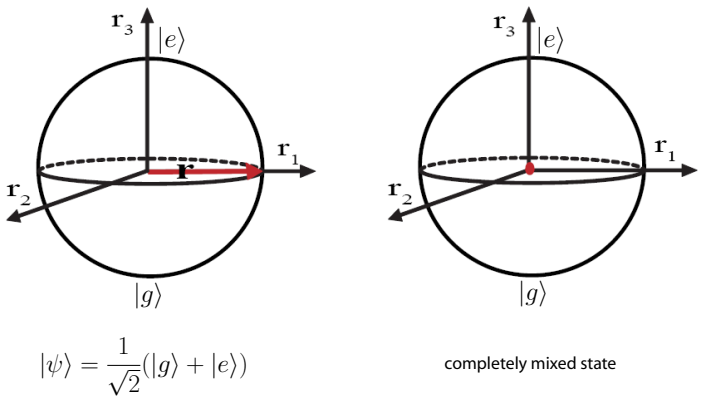

Figure 2.1: Bloch-vector representation of the quantum state of a two level atom.

Hamiltonian:

$$H_I(\mathrm{t}) = -\hat{\boldsymbol{\mu}} \cdot \mathbf{E} \tag{2.7}$$

The time evolution of the atomic system is described by inserting the density matrix into the Liouville equation with Hamiltonian $\hat{H} = H_o + H_I$:

$$\frac{\partial \rho}{\partial \mathrm{t}} = \frac{1}{i\hbar}[\rho, \hat{H}] \tag{2.8}$$

where H_o is the Hamiltonian of the unperturbed atom. Equation 2.8 can be expanded into four equations governing the evolution of each component of the atomic density matrix. Under the rotating wave approximation, which neglects rapidly oscillating components that vanish over relevant timescales, and assigning the electric field a given polarization (as would be the case with laser radiation), the equations of motion can be derived [50]. These equations describe evolution in the absence of decay, so effects from atomic coherences (T_2) and population relaxation (T_1) must be added [50], giving:

$$\begin{aligned}
\frac{\partial r_1}{\partial \mathrm{t}} &= -\Delta r_2 - \frac{r_1}{\mathrm{T}_2} \\
\frac{\partial r_2}{\partial \mathrm{t}} &= \Delta r_1 - \frac{r_2}{\mathrm{T}_2} + \Omega r_3 \\
\frac{\partial r_3}{\partial \mathrm{t}} &= -\frac{r_3 + 1}{\mathrm{T}_1} - \Omega r_2
\end{aligned} \tag{2.9}$$

where the detuning is $\Delta = \omega_L - \omega$, with ω being the atomic transition frequency. The 'Rabi frequency' Ω, is defined as

$$\Omega = \frac{\hat{\boldsymbol{\mu}} \cdot \mathbf{E}}{\hbar} \tag{2.10}$$

It characterizes the coupling strength of the light-atom interaction. Since this paramter only differs from the electromagnetic field by a constant, it is common practice to refer to Ω as the light field. To understand the significance of the Rabi frequency, consider the vector $\mathbf{\Omega} = (-\Omega, 0, \Delta)$ and an atomic system without decoherence, then Eq. 2.9 can be simplified to

$$\frac{\partial \mathbf{r}}{\partial \mathrm{t}} = \mathbf{\Omega} \times \mathbf{r} \tag{2.11}$$

This equation shows that, when coherent radiation interacts with a two level atom, the Bloch-vector (i.e. the atomic state) precesses around $\mathbf{\Omega}$ at a rate proportional to its length $||\mathbf{\Omega}|| = \sqrt{\Delta^2 + \Omega^2}$ (this is the generalized Rabi frequency). As an example, consider an atom in the ground state ($\mathbf{r} = (0, 0, -1)$) that is resonantly driven ($\Delta = 0$). If $\mathbf{\Omega} = (-1, 0, 0)$ then the atomic state will rotate around r_2 causing the atom to evolve from the ground into the excited state and back again in oscillation. This phenomena, called Rabi oscillations, happens with frequency Ω. Thus, a larger light-atom coupling strength corresponds to larger oscillation frequencies.

To quantify how much an atomic state changes with exposure to an electric field Ω for time t, the 'pulse area' can be defined as

$$\Theta = \int_0^{\mathrm{t}} \Omega(\mathrm{t}')d\mathrm{t}' \tag{2.12}$$

which corresponds to the angle by which the Bloch-vector rotates during atom-light interaction. For example, a π pulse, having $\Theta = \pi$, causes a 180° rotation of the Bloch-vector. For a square pulse, $\Theta = \Omega\mathrm{t}$, thus a 3.14 μs square pulse, having a field amplitude which causes a Rabi frequency of 1 MHz, allows for complete population transfer if an atom begins in the ground state.

2.1.3 Combining Maxwell and Bloch equations

Combining the Maxwell and Bloch equations allows to define a starting point in calculations when analyzing photon echo based quantum memory protocols. From here, atomic evolution is dictated thus it can be analyzed for deeper understanding and optimized to predict achievable limits for important parameters. Simple experimental parameters can be included, for example T_1 or Ω, such that the Maxwell-Bloch equations can be used to predict the outcomes of experiments to determine if they have value in being performed. In our case, atomic evolution involves an inhomogeneously broadened array of absorbers, this must be taken into account. Inhomogeneous broadening is also found in other atomic systems (e.g. atomic vapours) other than rare-earth-ion doped solids. This absorption profile can be described by a distribution function $g(\Delta)$ satisfying

$$\int_{-\infty}^{\infty} d\Delta g(\Delta) = 1 \tag{2.13}$$

where Δ is the detuning of the atomic transition from the light carrier frequency. Thus the medium can be thought of as a continuum of two-level atoms with a corresponding Bloch-vector at each position z, and for each detuning Δ, distributed according to $g(\Delta)$, which gives a continuous field of Bloch-vectors $\mathbf{r}(z, t, \Delta)$. The polarization of the medium can then be written as

$$\mathbf{P}(z, \mathrm{t}) = \frac{N}{2} \int_{-\infty}^{\infty} d\Delta g(\Delta) \boldsymbol{\mu_{ge}} [r_1(z, \mathrm{t}, \Delta) - i r_2(z, \mathrm{t}, \Delta)] + c.c. \tag{2.14}$$

where N is the density of atomic dipoles, and the transition dipole moment $\boldsymbol{\mu_{ge}} = \langle g|\hat{\boldsymbol{\mu}}|e\rangle$ is the off diagonal element of the dipole operator $\hat{\boldsymbol{\mu}}$. Only the off-diagonal terms of the density matrix carry contributions from the atomic dipole, which determines microscopic polarization, therefore only r_1 and r_2 along with $\boldsymbol{\mu_{ge}}$ are considered to contribute to the polarization. Thus each atomic dipole is summed and weighted according to their spectral distribution to give the macroscopic polarization $\mathbf{P}(z, \mathrm{t})$ appearing in Maxwell's

equations. Now combining Eq. 2.14 with the simplified wave equation 2.3 results in the Maxwell equation

$$\frac{\partial}{\partial z}\Omega + \frac{n}{c}\frac{\partial}{\partial \mathrm{t}}\Omega = \frac{ia}{2\pi}\int_{-\infty}^{\infty} d\Delta g(\Delta)[r_1(z,\mathrm{t},\Delta) - ir_2(z,\mathrm{t},\Delta)] \tag{2.15}$$

where the constant $a = \frac{\pi N \mu^2 \omega_L}{2\hbar\epsilon c}$. This equation and the Bloch equations 2.10 form the Maxwell-Bloch equations which well-describe the interaction of coherent light with two-level inhomogeneously broadened absorbers.

2.2 Spectral hole burning

An inhomogeneously broadened line Γ_{inh} is composed of a spectrum of different absorbers each with their own homogeneous (individual) linewidth Γ_h. Thus, with a narrowband light source, it is possible to excite a specific ensemble of ions absorbing at the source frequency. This interaction transfers ion population from their ground state and into their excited state, in other words, changing the Bloch-vector component r_3. This population imbalance causes a decrease in material absorption at the excitation frequency, as seen as a spectral hole in the inhomogeneous broadened profile, see Fig. 2.2. Spectral hole burning is a powerful spectroscopic tool as it makes it possible to probe population dynamics within the inhomogeneous broadening. It also provides the basis for spectral tailoring which involves modifying optical depth at different spectral locations in the inhomogeneous broadening. This is important for preparing a rare-earth doped crystal for implementing quantum data storage. An overview of hole-burning spectroscopy studies in rare-earth ion doped samples are found in Ref. [48].

2.2.1 Hole burning spectroscopy

In a hole-burning experiment, a laser selectively excites a narrow portion of the inhomogeneous line, and the absorption is 'bleached' as absorbers are removed from the ground

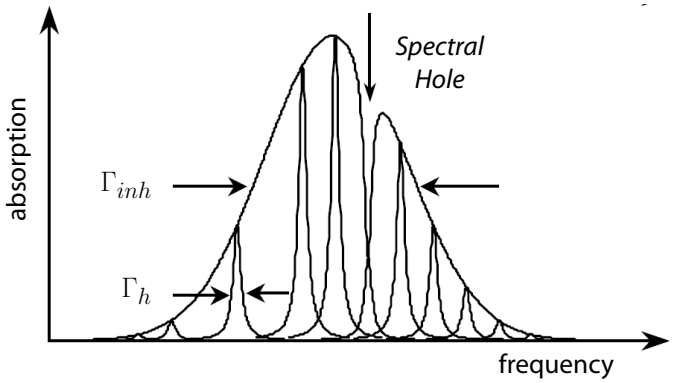

Figure 2.2: Line broadening and spectral hole burning. The envelope over all homogeneous linewidths Γ_h defines the inhomogeneous line Γ_{inh}. A spectral hole is created at the laser frequency and can be seen as a reduction in absorption. Figure taken from Ref. [51].

state. This effect can be observed by scanning the laser frequency across the original excitation frequency while monitoring the transmission of light diffracted off the spectral hole [52, 53]. This results in observation of a spectral hole $\Gamma_{hole} = 2\Gamma_h$ in the limit of negligible laser linewidth or power broadening. By measuring the hole width for a set of different pump powers one can extract the homogenous linewidth in the limit of zero power broadening [54], which is given by (for optically thin samples):

$$\Gamma_{hole} = \Gamma_h(1 + \sqrt{1 + \frac{I}{I_s}}) \tag{2.16}$$

where I is the intensity of the burning pulse, I_s is the saturation intensity. In the case where the laser linewidth is larger than Γ_h, twice the laser linewidth will be observed at zero burning power. The spectral hole remains as long as the population difference between the ground and the excited state differs from that in thermal equilibrium, i.e. until all absorbers have returned to the original ground state.

So-called 'persistent' holes occur if some absorbers are transferred to a reservoir state and can no longer absorb at their original frequency. For example, in thulium-doped crystals, if ions are optically excited from the ground $^3H_6$ into the $^3H_4$ and then decay into the metastable $^3F_4$ state, a hole would last much longer than if ions are mostly placed

into their excited level only, e.g. the $^3H_4$ level in thulium, then the hole is considered to be 'transient'. See Fig. 4.4 for an energy level diagram. In a material where the ground state is split into sublevels (e.g. rare-earth materials with hyperfine splitting or nuclear Zeeman levels) with an energy separation larger than the homogeneous linewidth, persistent hole-burning may occur due to population redistribution among the sublevels.

The width, shape and decay of the hole reveals much information about an ion that would otherwise be hidden by the inhomogeneous broadening of the optical transition. The simplest case of time-resolved spectral hole burning gives information about population dynamics. Since a spectral hole decays in time according to how much population remains in excited or auxillary states after pumping, one can recover T_1 of the levels involved. For the persistent hole burning sequence described above, the spectral hole depth will decay according to:

$$d(\mathrm{t}) \sim A\mathrm{e}^{-\mathrm{t}/\mathrm{T}_{1A}} + Be^{-\mathrm{t}/\mathrm{T}_{1B}} \tag{2.17}$$

where $d(\mathrm{t})$ is the hole depth; T_{1A} and T_{1B} are the lifetimes of the $^3H_4$ (denoted A) and $^3F_4$ (denoted B) respectively; A and B are constants that depend on population in the $^3H_4$ or $^3F_4$ states respectively at $\mathrm{t} = 0$.

If the level splittings are not at optical wavelengths, but hyperfine states then a more complex hole burning structure can be seen, see Fig. 2.3. If there are several sublevels in the excited state, 'side-holes' will appear at frequencies corresponding to each of the transitions from the ground state level with depleted population, in addition to the hole at the burning frequency. 'Anti-holes', i.e. increased absorption, will occur at frequencies corresponding to transitions from the ground state hyperfine levels with increased population, i.e. levels to which ions have been optically pumped into. Since the optical transition usually has a large inhomogeneous broadening, different subsets of ions will have different transition frequencies between ground hyperfine and excited hyperfine

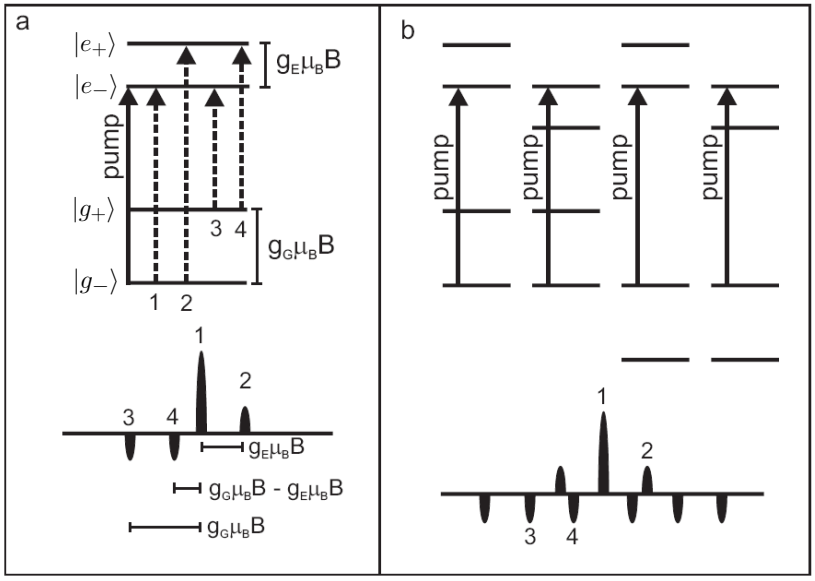

Figure 2.3: a. Four-level hole burning spectrum (Zeeman levels) for the class of ions where the laser is in resonance with the $|g_-\rangle$ to $|e_-\rangle$ transition. B is the applied magnetic field, g_i and μ_i are constants. The pump transition (solid line) and possible probe transitions (dashed lines) between the four levels are shown in the energy diagram and labelled on the corresponding transmission spectrum of holes and anti-holes. b. Four-level hole burning spectrum with inhomogeneous broadening. Figure is taken from Ref. [55].

state levels, and any laser frequency inside the inhomogeneous line will be resonant with all possible optical transitions, but for different subsets of absorbers. Thus, burning at a single frequency creates a pattern of side-holes and anti-holes (see for e.g. Ref. [56]). Relative hole sizes quantify the relative transition strengths between different hyperfine levels.

Much more can be learned from this structure if parameters such as temperature or magnetic field (strength and angle) are changed since material parameters are influenced by these changes. Similar information can be extracted if nuclear Zeeman levels are activated, including a Zeeman shift of the hole when different magnetic fields are applied. In non-centrosymmetric crystals under application of an elctric field, spectral holes will be displaced as a consequence of the DC Stark effect [57]. Using spectral hole burning, the magnitude and quality of the hole shift tells how much a transition can be shifted for a

given applied electric field. Moreover, if level splittings arise from superhyperfine interactions then the effects of different nuclear moments can be isolated, telling information about crystal structure (i.e. where different atoms are nearby in the lattice). Hole burning can be used for applications other than spectroscopic measurements, these include frequency domain classical data storage [58] where occurence or absence of a hole defines logical zero or one, frequency stabilization of lasers for spectroscopic and metrological reasons [51].

2.2.2 Spectral tailoring

Coherent laser light interacting with a portion of the inhomogeneous broadened line produces a measurable Lorentzian shaped transparency windows which we know to be a spectral hole. This procedure can be generalized to produce more complex frequency profiles (e.g. a periodic modulation of the inhomogeneous broadening). This is the central idea of spectral tailoring, to modify the inhomogeneous line by selectively adding and removing absorbers of particular frequencies thus creating a new spectral profile. Usually this involves *optical pumping*, which raises ions from the ground state into an excited state, with subsequent decays redistributing population into other energy levels (e.g nuclear Zeeman levels). Efficient pumping into ground state sublevels is required for photon echo quantum memory as it allows creating a persistent spectral profile due to the long lifetimes of these levels.

One basic spectral feature is a narrow absorption peak, resulting from an ensemble of selected ions with a specific absorption frequency, on a background of zero absorption. For example, this allows isolation of a specific transition to be studied. More relevant to quantum memory, this prepared line, which must be optically thick, is the starting point in CRIB (discussed later in the chapter). A straightforward method for creating this structure, is to simply burn away the ions in the surrounding spectral interval (i.e.

repeatedly exciting them until they decay into a long lived). Another way is to first empty a wide spectral interval, say by pumping population into a long-lived nuclear Zeeman level, then shift the laser frequency, and reversibly hole burn to pump back a narrow interval of ions absorbing at a narrow spectral interval as in Ref. [59]. Both approaches are limited by the laser jitter, pumping dynamics (depth of peak on non-absorbing background). A spectral feature important for AFC quantum memory is to prepare not only one, but many narrow evenly spaced peaks in frequency, with large optical thickness, on a non-absorbing background (discussed later in the chapter).

2.3 Photon echo

While standard hole burning usually involves incoherent light-matter interaction, and thus concerns itself with population transfer (i.e. diagonal elements of the density matrix) this section focuses on photon echoes, which arise from coherent light-matter interactions (i.e. off-diagonal elements). For this reason, photon echoes are a vital ingredient for many experiments in spectroscopy.

Much of the theory of photon echo stems from coherently driven two-level systems originally developed for nuclear spins driven by radio-frequency (RF) fields within the context of nuclear magnetic resonance (NMR). Upon the advent of the laser, optical equivalents of these ideas were realized. Many textbooks provide a thorough treatment of photon echo and related phenomena in two-level atoms (for example see Ref. [60]). Here we focus on the central ideas behind photon echo for interpreting spectroscopic measurements performed for this thesis, and providing a prerequisite for describing photon echo based quantum state storage. We start with the simplest version i.e. the two-pulse photon echo, followed by the three-pulse echo (or stimulated echo) which sets the stage for introducing quantum memory protocols.

Photon echo is tied to the fact that an ensemble of atoms oscillating in phase emits strong coherent radiation, in contrast to the radiation emitted by atoms with a random distribution of phases. When atoms emit incoherently, as in spontaneous emission, the intensity is proportional to the number of emitters, N. However, if the phases of the emitted light fields are such that the field amplitudes interfere constructively, then the electric field amplitude is proportional to N, and the emitted intensity will thus be proportional to N^2. If the emitting atoms are distributed in space, their emission can only add coherently in specific directions, given by phase matching. The 'in-phase' coherent emission is short-lived in a medium such as rare-earth-ions in a crystal, as they will dephase due to their differences in frequency. However, by preparing atoms at specific frequencies and with specific phases, the medium can be programmed to rephase and emit coherently (i.e. producing an echo) at a particular time, or even to emit a complicated sequence of pulses. The magnitude of coherent emission in time is decreased due to decoherence goverened by T_2, which eventually results in atomic phases being randomized, this means that their dipole moments do not add constructively.

The simplest, 'two-pulse photon echo' is observed after two strong brief laser pulses, separated by τ_{12}, are sent into a rare-earth-ion doped solid beginning in its ground state, see Fig. 2.4. The first pulse sets up coherence between the ground and the excited state. Ideally, this should be a $\frac{\pi}{2}$-pulse, placing the atoms in the r_1-r_2 plane of the Bloch sphere (see Fig. 2.4 a). Initially all the atoms are phase aligned with the excitation light, with their Bloch-vectors all pointing in the same direction. Due to the inhomogeneous broadening, the atoms dephase (i.e. acquire a phase difference relative to the laser that is proportional with their detuning). The second (π) pulse rotates the phase of the atomic states by π. Atoms which have acquired a negative phase difference relative to the laser will now have a positive phase, which starts to decrease (Fig. 2.4 c). After some time, all atoms again oscillate with the same phase (in a forward propagating frame), which

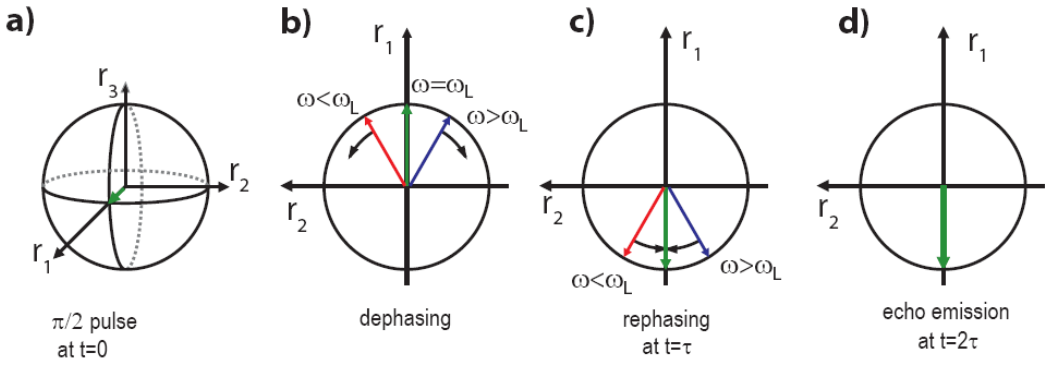

Figure 2.4: Two-pulse photon echo process. a) shows the Bloch-vector on the Bloch sphere after applying the first pulse, b)-d) show the evolution of the Bloch-vector on the equator of the Bloch sphere during the two-pulse echo protocol.

re-establishes the original dipole moment and causes the emission of light known as the photon echo (Fig. 2.4 d). It is not necessarily required that the pulses be $\pi/2$ or π but rather these values maximize the echo intensity. Importantly, the two pulse photon echo allows access for measuring the coherence time, as delaying the two excitation pulses in time results in an echo of less intensity. In a two-level system the echo intensity, I, will decay according to:

$$\mathrm{I(t)} \sim \exp(-4\tau_{12}/\mathrm{T_2}) \tag{2.18}$$

where $\mathrm{T_2}$ is the coherence time of the transition.

The 'three-pulse photon echo' is another pulse sequence that produces an echo. An intuitive description has the second pulse in the two-pulse echo being split into two $(\pi/2)$ parts delayed by τ_{23} from one another, which produces an echo at a time τ_{12} after the third pulse. As in the two-pulse echo the first pulse sets coherence between ground and excited states, but now has the second pulse rotates the quantum state into the plane defined by the ground and excited states. The third pulse causes the atoms to be rotated into the plane as in the two-pulse case, at that point rephasing occurs and an echo is emitted. The three pulse echo is often also called 'stimulated echo'. In a two level system,

the echo will decay according to:

$$\mathrm{I(t)} \sim \exp(-4\tau_{12}/\mathrm{T_2})\exp(-2\tau_{23}/\mathrm{T_1}) \tag{2.19}$$

where $\mathrm{T_2}$ is the coherence time, and $\mathrm{T_1}$ is the lifetime of the transition. Within the $\mathrm{T_1}$ time, many pulses can be sent into the sample, with corresponding echoes being achieved. Therefore, the effect of the first two pulses is to create a frequency-dependent periodic modulation of the population in the ground and excited states, i.e. a population 'grating' containing full information about the relative phase and time separation between the two pulses. The period of the grating, inversely proportional to the time interval between the first two pulses τ_{12}, dictates the delay time of the echo. If more than two levels are involved, a grating can be persistent. Thus stimulated echoes can be created within, for example, a ground state lifetime- long after optical excitations have decayed. Stimulted echo has been used as a powerful spectroscopic tool, for example to assess population relaxation dynamics, the long-term homogeneous linewidth in spectral diffusion measurements, and instantaneous spectral diffusion (by extrapolating measurements to zero pulse intensity). A more efficient stimulated echo can be achieved by preparing the grating on a non-absorbing background, since the comb structure is composed of absorbers that contribute to rephasing, while background absorption only contributes to absorption of light. This background can be removed by sending multiple pulse pairs to interact with the inhomogeneous profile which acts to carve the grating down to lesser optical depths. This accumulation of pulses by the absorbers coined the the so-called 'accumulated photon echo' sequence [61].

2.3.1 Quantum memory protocols

At first sight, one may try to use stimulated (accumulated) echo directly reversibly map single photons. However, one must approach this type of data storage with caution

as traditional photon echoes are produced along with much *photoluminescence* coming from the optically excited states due to population inversion from the preparation pulses. Any decaying optical transitions will add noise to the output signal and decrease storage fidelity. For this reason, two or three pulse photon echo is not appropriate for quantum state storage [47]. However for conventional photon echoes, this population inversion is an added benefit as greater than unit echo efficiencies can be achieved [62].

Indeed, a population grating must be created outside of the lifetime of the optical transitions involved in storing the single photon of interest, or without allowing population into the excited level of this transition. This is typically achieved by first preparing the grating, then waiting for a time (much) longer than the optical lifetime. Waiting allows for population to relax away from the excited level and into other metastable levels such as hyperfine ground states. As described here, this preparation method identifies a way to prepare an atomic frequency comb (AFC) for quantum state storage.

In the spirit of stimulated echo, the AFC quantum memory protocol, proposed and demonstrated in 2008 [40, 41], is used to store multimode *quantum* states of light. Thus a quantum mechanical apprach must be used to explain its mechanism, including its on-demand recall capability. This is done in the following paragraphs. We then introduce the controlled reversible inhomogeneous broadening protocol, which also relies upon controlled dephasing/rephasing with the added unique feature that it exploits a time-reversal symmetry in the equations of motion in the photon-atom system.

Atomic frequency comb: Consider an ensemble of ions with an optical transition formed by two levels, $|g\rangle$ and $|e\rangle$ as shown in Fig. 2.5. This transition has a narrow homogeneous linewidth Γ_h and a large inhomogeneous broadening Γ_{inh} ($\Gamma_{inh}/\Gamma_h \gg 1$). The excited state $|e\rangle$ is optically connected to another state $|s\rangle$. The states $|g\rangle$ and $|s\rangle$ are typically ground-state hyperfine or nuclear Zeeman states. The $|g\rangle \leftrightarrow |e\rangle$ transition is spectrally shaped such that the absorption profile consists of a series of narrow peaks

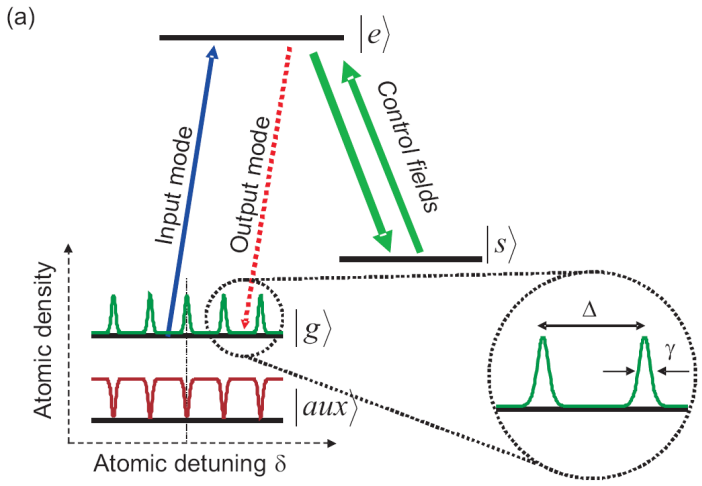

Figure 2.5: The principle level structure for the AFC quantum memory. An inhomogeneously broadened optical transition $|g\rangle$ to $|e\rangle$ is shaped into an AFC by frequency-selective optical pumping to the $|aux\rangle$ level. The peaks in the AFC have width (FWHM) γ and are separated by Δ. Figure taken from Ref. [40].

spanning a large frequency range, i.e a frequency comb, on a non-absorbing background. In this description, this can be done by frequency-selectively transferring atoms from $|g\rangle$ to a metastable state $|aux\rangle$, for instance a third hyperfine state, through optical pumping techniques.

Consider now a single-photon input which is in resonance with the $|g\rangle \leftrightarrow |e\rangle$ transition, having a spectral distribution γ_p larger than the AFC peak separation Δ, but narrower than the total width of the AFC, Γ. If the integrated absorption over γ_p is high enough, the photon can be completely absorbed by the AFC. This effect can be interpreted in terms of the Heisenberg energy-time uncertainty relation. Over the time scale of the absorption, which is on the order of the input pulse duration $\tau = 1/\gamma_p$, the comb will have an uncertainty of the order of $\gamma_p \gg \Delta$. This causes the photon to see spectrally averaged AFC structure resulting in a smooth distribution, thus allowing for uniform absorption over the photons bandwidth [40].

After absorption, at t = 0, the photon is stored as a single excitation distributed coherently over all the atoms in the ensemble that are in resonance with the photon. The

state is described by a collective Dicke state [63]:

$$|\psi\rangle = \sum_{j=1}^{N} c_j e^{i\delta_j \mathrm{t}} e^{-ikz_j} |g_1 \cdots e_j \cdots g_N\rangle, \tag{2.20}$$

where z_j is the position of atom j, k is the wave-number of the light field (consider a single spatial mode defined by the direction of propagation of the input field, as would be in a waveguide), δ_j the detuning of the atom with respect to the laser frequency and the amplitudes c_j depend on the frequency and on the spatial position of the particular atom j.

The collective state, $|\psi(\mathrm{t} = 0)\rangle$, can be understood as a coherent excitation of a large number of AFC modes by a single photon which are intially in phase with respect to the spatial mode k. As time evolves, the collective state will dephase, since each term acquires a phase $\exp(i\delta_j \mathrm{t})$ depending on the detuning δ_j of each excited atom. Considering an AFC with sharp peaks, the detunings δ_j are approximately a discrete set such that $\delta_j = m_j \Delta$, where m_j are integers. The comb discreteness allows for rephasing to occur, thus establishing the collective intitial state, after a time $\mathrm{t} = 2\pi n/\Delta$ for integer $n > 0$, leading to a coherent photon-echo [64, 65] reemission in the forward direction. In general, depending on the quality of the comb, complete rephasing may not be achieved for $n = 1$, thus energy may still remain in the comb absorbers, allowing for probabilities of photon reemission at times where $n > 1$.

Up to now, we have discussed the AFC having a fixed storage time. To allow for on-demand readout of the stored input, the single collective excitation in $|e\rangle$ is transferred to the ground state spin level $|s\rangle$. This can be done by applying an optical control field on $|e\rangle \leftrightarrow |s\rangle$, for instance a short π pulse or via a direct Raman transition. The excitation is thereafter stored as a collective spin wave, and as an added advantage, allows for long-lived storage since spin coherence lifetimes are generally longer than the optical coherence lifetimes. If the spin transition does not have a comb structure (e.g. in

rare-earth-ion doped crystals), this means that the evolution of the phases in Eq. (2.20) will be frozen during the storage in the spin wave. To retrieve the input field, a second counter-propagating control field is applied after a time T_s. The directionality of this control field allows phase matching conditions to be satisfied, resulting in a backward propagating output photon after a total time $T_s + 2\pi n/\Delta$ [40]. Notably, AFC with on-demand recall has been shown recently in $Pr^{3+} : Y_2SiO_5$ [66].

The efficiency of the AFC protocol can reach 54% in the forward direction (limited only by re-absorption), and if the re-emission is forced to propagate in the backward direction, the process can reach 100% efficiency (provided the photon is completely absorbed into the comb, i.e. $\alpha L >> 1$). Note that recently it has been proposed that by placing the sample inside an asymmetric impedance-matched cavity, unit efficiency can be achieved under the conditions of forward recall [67, 68]. The storage efficiency, for both forward and backward recalls, can be quantified by the quality of the prepared atomic frequency comb. Assuming an AFC is composed of a sum of Gaussian peaks, then it can be characterized by its finesse $\mathrm{F} = \Delta/\gamma$, its peak comb absorption depth d and the background d_0. The absorption background arises from imperfect optical pumping. Using the theory of an AFC memory reported in Refs. [40, 41], the retrieval in the forward and backward directions can be calculated:

$$\eta_f{}^{AFC} \approx \tilde{d}^2 \mathrm{e}^{-\tilde{d}} \mathrm{e}^{-7/\mathrm{F}^2} \mathrm{e}^{-d_0} \tag{2.21}$$

$$\eta_b{}^{AFC} \approx \left(1 - \mathrm{e}^{-\tilde{d}}\right)^2 \mathrm{e}^{-7/\mathrm{F}^2} \mathrm{e}^{-d_0} \tag{2.22}$$

where $\tilde{d} = d/\mathrm{F}$ is the effective absorption depth of the comb. In backward retrieval, high finess and optical depth leads to $\eta_b \to 1$.

An advantage of a quantum memory based on atomic frequency combs, is its large multimode capabilities independent of the available optical depth, in contrast to other quantum memory protocols such as CRIB and EIT. To illustrate this, imagine that the

AFC has an input of many temporally distinguishable modes containing approximately a single photon in each mode, and the storage efficiency is uniform over all the modes. If the control fields are applied as late as possible, the total duration of the input can be close to $T = 2\pi/\Delta$, the time it takes to rephase the first mode that was absorbed. The shortest duration τ of one mode, however, is only limited by the total frequency bandwidth $\tau \sim 1/(N_p\Delta)$, where N_p is the number of peaks in the comb. The number of modes $N = T/\tau \sim N_p$ is then proportional to N_p, such that adding more peaks in the AFC allows one to store more modes. Thus one can increase the multimode capacity by increasing the number of peaks within the bandwidth covered by the stored photonic field. This means either Δ is reduced, thus increasing the storage time, or the bandwidth of the stored light is increased which allows for storage of shorter pulses (since N is only limited by Γ_{inh}). For comparison, to store N modes, EIT requires an optical depth varying as $d \sim \sqrt{N}$ [17] with CRIB requiring $d \sim N$ [22]. As an example, CRIB requires $d = 30N$ for 90% efficiency [22], with an even higher d for EIT, while the AFC only requires $d = 40$ to reach the same efficiency, independently of N.

Controlled reversible inhomogeneous broadening: The initial idea for CRIB begins with a paper by S. Moiseev and S. Kroll in 2001 [69], as an approach to time-reverse the photon-echo storage process in atomic vapor. In 2005 and 2006 three groups then described how the quantum memory scheme could be extended to solid state materials storing photonic wave packets [70, 71, 72]. This reincarnation is what is generally referred to as CRIB, and relies on triggering a *time-reversal* of the absorption process thus allowing for on-demand storage and recall of an input single photon field.

To implement CRIB, one must begin with a narrow absorption line on a non-absorbing background, see Fig. 2.6. This can be achieved by spectrally tailoring the inhomogeneous absorption profile using optical pumping techniques (described in section on spectral tailoring). As in AFC, the spectral feature must be persistent, so ions must be transferred

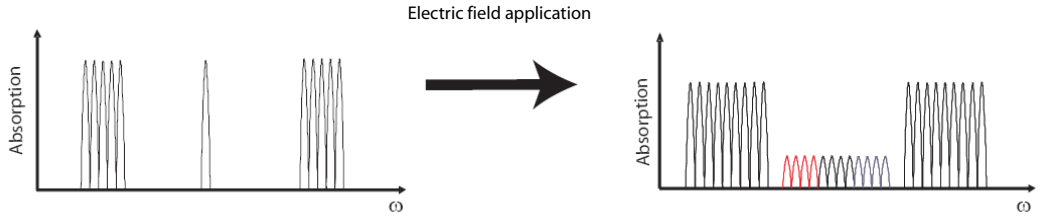

Figure 2.6: Broadening the narrow absorption line in CRIB. Left: CRIB begins with a narrow absorption line on a non-absorbing background. Right: application of an inhomogeneous electric field broadens the line.

to a long-lived auxillary state, such as hyperfine levels. Next this narrow line must be artificially broadened in a controlled way so that the incoming wave packet can be absorbed. If the rare-earth doped crystal is non-centrosymmetric, this can be done via Stark shifts (other materials, such as atomic vapours use magnetic fields for the same purpose). The application of an inhomogeneous, or position-dependent, electric field introduces a different frequency shift for each atom in the crystal lattice depending upon its position, see Fig. 2.6. This allows for broadening of the intitially prepared narrow line, resulting in a large bandwidth, and setting the stage for absorption of the input field. The electric field has produced a large inhomogeneous broadening, thus allowing for all frequency components of the photon can be absorbed, and the state of the photon is transferred to the atomic ensemble. After absorption, the ions begin to dephase as described in conventional photon echo, and their collective dipole moment decays at a rate which goes as the inverse of the linewidth of the initially prepared peak. Before coherences are lost, the stored photon can be forward recalled on-demand by rephasing the atomic dipoles. This is accomplished by simply reversing the polarity of the applied electric field, resulting in the artificially broadened profile being reversed. The storage time of this scheme is limited by the optical coherence time. Yet coherence can be transferred to a long-lasting spin state, similar as AFC (e.g. using a π pulse). Similarly again, for recall, another counter-propagating π pulse transfers the coherence back to the optical

transition. These two pulses must be implemented before the electric field polarity is reversed. More importantly, these counter-propagating fields complete the time-reversal of the absorption process allowing for backwards retrieval of the input photon, with unit efficiency possible provided complete absorption of the input field. More details on the theoretical description CRIB can be found in Ref. [72]. Again, efficiencies can be calculated for forward and backward retrieval, resulting in equations of similar form to those predicted from the AFC protocol:

$$\eta_f{}^{CRIB} \approx d^2 \mathrm{e}^{-d} \mathrm{e}^{-d_0} \tag{2.23}$$

$$\eta_b{}^{CRIB} \approx \left(1 - \mathrm{e}^{-d}\right)^2 \mathrm{e}^{-d_0} \tag{2.24}$$

where d denotes the peak optical depth of the intially prepared absorption line and d_0 is the background absorption. Thus large optical depths are again required for efficient storage. It is easy to see that, like AFC, the maximum forward efficiency in CRIB is limited to 54% (where $d = 2$). A recent approach to CRIB, called longitudinal CRIB or gradient echo memory, has an absorption line that is narrow, but spectrally varies monotonically through the medium when a field gradient is applied in the light propagation direction [71, 73]. Upon reversing the polarity of the gradient, an echo is produced in the forward direction which can occur with unit efficiency, since each frequency component of recalled light is detuned from any absorbers upon exiting the material. This approach has allowed for quantum storage of wave packets containing up to hundreds of photons with record 69% efficiency using a quantum memory protocol [42]. To conclude this section, it important to point out that intial demonstrations of these protocols in rare-earth crystalline hosts has established evidence that photon echo based quantum memories may have the capabilities to satify the challenging performance criteria for a quantum memory in quantum repeaters, see Fig. 12 in Ref. [43].

Chapter 3

Rare-earth-ion doped crystals

This thesis is concerned with the interactions between coherent light and rare-earth-ions doped into optically transparent crystal solids. When the host crystal is cooled down below 4 K, these ions acquire optical properties, such as long dephasing and relaxation times, that make them suitable to use as a quantum memory. One effect of the low temperature is to reduce crystal lattice vibrations (i.e. phonons) which can act to reduce the optical coherence time.

The rare-earth elements, also known as rare-earth metals or the Lanthanides, are comprised of 14 elements from Lanthanum (atomic number 57) to Ytterbium (atomic number 70). The term rare-earth was given to the group because they were initially discovered in small quantities in oxide mixtures, which were once called 'earth' mixtures. Despite the name, the rare-earth elements are not rare [74, 75].

Spectroscopy of the Lanthanides are unique in that the 4f orbital is shielded from the external (crystal) environment by the 5s and 5p outer orbitals as shown in Fig. 3.1. This shielding results in spectrally narrow transitions. The rare-earth elements share the same bonding electrons, that of the 6s, 5s and 5p shells and hence share many chemical properties. When doped into inorganic crystals, they generally occur as triply charged ions, RE^{3+}, where 'RE' denotes the rare-earth element abbreviation. This results in Lanthanum taking the stable electronic configuration of Xenon. Configurations of each subsequent element in the Lanthanide series are achieved by adding another electron to the f-shell. Therefore the triply charged Lanthanides are in the configuration $[Xe]4f^n$ where $n = 0$ for Lanthanum and $n = 14$ for Lutetium.

Since coherent interactions with light involve the 4f transitions, the optical properties

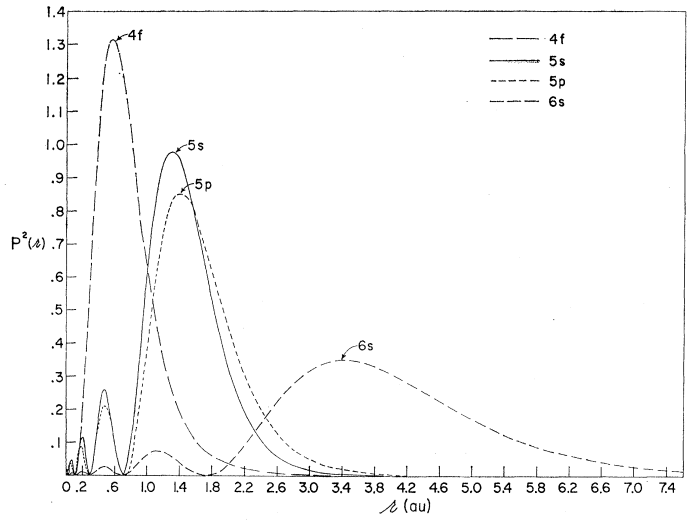

Figure 3.1: Radial electron charge densities for the 4f, 5s, 5p and 6s electrons in Gd^+. Electron probability density is plotted against atomic radius. The 4f electrons lie inside the 5s and 5p shells, being partially shielded from external perturbations. This figure is taken from [76].

of these ions resemble those of free ions, except here the embedded ions have fixed positions in space. For this reason rare-earth-ions doped into a transparent solid can be thought of as a frozen gas or as naturally occuring trapped ions. The analogy should be used with some caution, however, since the optical properties of these ions are still affected by their interaction with the surrounding crystal environment.

In the following I introduce spectroscopic fundamentals and nomenclature behind rare-earth-ions doped into crystals. This includes describing the energy level structures, splittings, and broadenings. Interactions with electric and magnetic fields are described as they impact heavily on the system dynamics and act as control parameters for implementations of photon echo based memories. This section serves as a prerequisite to understand the experimental results presented in chapter four.

3.1 Level structure

The energy levels of a rare-earth-ion in a crystal host is generally approximated by starting from the free-ion levels, described through spin-orbit interactions, and then taking the crystal field into account and treating the remaining interactions as small perturbations. Levels are denoted using the term symbol which takes the form of: $^{2S+1}L_J$. S is the total spin quantum number, J is the total angular momentum quantum number, and L is the total orbital angular momentum quantum number in spectroscopic notation (e.g L = 1 denotes P, L = 5 denotes H). A set of energy levels having the same electronic structure, i.e. the same values of L, S and J, splits into at most 2J+1 'Stark levels' by the electrostatic crystal field, with level separations typically around 0.1-1 THz. The crystal field also causes mixing of the electronic states, which can cause transitions that would be forbidden in a free ion to become weakly allowed [77]. Therefore conventional labelling of free ion states ($^3H_4$, $^1S_0$ etc.) is slightly misleading, but is still used in this context. The ions excited to higher lying levels of a Stark manifold usually relax very rapidly through phonon emission to the lowest lying Stark level, and in this work only the transition from the lowest Stark level of the ground state to the lowest level of an optically excited state is used, as is the case for most works employing rare-earths for quantum memories. Since this transition does not involve the absorption or emission of phonons, it is known as the 'zero phonon line'.

The magnetic properties for the rare-earth-ions are different according to whether the ion has an even or odd number of f electrons (after being incorporated into the crystal lattice). Rare-earth-ions with an odd number of 4f electrons, after forming RE^{3+} are called Kramers ions. Due to their unpaired electron, they tend to have large magnetic moments. If an ion with an even number of electrons placed into crystal sites with lower than axial symmetry, the crystal field levels are 'quenched' of their angular momentum

(i.e. zero angular momentum). These ions are called non-Kramers ions. Generally speaking, the energy and structure of the levels depend strongly on the host material and the symmetry properties of the site in which the rare-earth-ion has substituted a host material ion (i.e. its position within a unit cell). For example, Nd^{3+} is strongly paramagnetic due to its unpaired electron and crystal structure [78].

3.1.1 Hyperfine splittings

The next level of detail in the level structure beyond the crystal field splitting comes from the magnetic hyperfine interaction, which represents the magnetic interaction between the nuclear magnetic dipole moment and an 'effective' electronic magnetic dipole moment. This acts to cause a hyperfine splitting of the nuclear states, which is usually on the order of megahertz to several hundred MHz (e.g. in Eu^{3+}:Y_2SiO_5 [79]). The effective electronic moment arises from a coupling of the free-ion electronic magnetic moment and other nearby electronic states, which can result in an enhanced hyperfine interaction [37]. Another perturbation at these energies is an interaction of the nuclear quadrupole moment with the electric field gradient due to the neighboring ions in the crystal lattice. This perturbation is only available for ions which have a nuclear magnetic moment larger than 1/2.

When considering applications in quantum memory, it may be possible to use ground state hyperfine levels for long-term population storage, or for mapping of optical coherences since relaxation may be slow between these levels (depending on temperature, magnetic field). This relaxation may involve a spin-exchange with surrounding nuclei, or a phonon-assisted process. In Eu:Y_2SiO_5 the hyperfine level lifetime is several days, and the ground state hyperfine coherence time of praseodymium can be as long as 30 s [74].

In other cases it is necessary to consider a superhyperfine splitting, due to the additional energy of the interaction between the electronic states of the ion and the nuclear

magnetic moment of the surrounding atoms in the host material.

3.2 Line broadening

As in any atomic system, there is a probability that an excited state will decay, thus any resonance feature has an associated non-zero linewidth. This linewidth is characteristic to a given atomic transtion, but when considering rare-earth-ions doped into crystals, the width and location of the line depends not only on the atomic species but on an atom's environment and crystal properties (e.g. site symmetry and doping concentration). In the context of this work, it is important to understand the mechanism behind spectral line broadening for foundational reasons and to assess physical limitations of the memory, e.g. for memory preparation (spectral tailoring). Two important broadening mechanisms are prevalent in rare-earths doped into crystals: homogeneous and inhomogeneous broadening.

3.2.1 Homogeneous broadening

The homogeneous linewidth characterizes the width of the line of each particular ion at a particular temperature and magnetic field, and is the narrowest line one will find in rare-earth-ions doped into crystals. Homogeneous broadening is due to relaxation and dynamic processes (e.g. phonon-assisted processes, ion-ion interactions). The linewidth, Γ_h, is related through the time-frequency Fourier transform to the coherence time, T_2, of an ion, according to

$$\Gamma_h = \frac{1}{\pi T_2} = \frac{1}{2\pi T_1} + \frac{1}{\pi T_2^*} \tag{3.1}$$

Included here is the relationship between the coherence time T_2, the relaxation time, T_1 and a 'pure dephasing' time T_2^* [80]. The coherence time is reduced by decoherence such as coupling of levels by emission, absorption or scattering of lattice phonons. The density

of phonon states, dictated by temperature governs the effects of these vibrations. At low temperatures the photon numbers are small, but if the temperature is increased above a few Kelvin, the lattice phonon density contributions to the homogeneous linewidth will dominate and limit coherence time to nanoseconds at best. In the absence of this dephasing mechanism, the minimum homogeneous linewidth is determined by spontaneous relaxation alone, so in general $2T_1 \geq T_2$. Linewidths approaching this limit can be seen in materials where all other dephasing processes have been minimised, such as in Er^{3+}:Y_2SiO_5, where the narrowest optical resonance in any solid-state material of 73 Hz (T_2 = 4.38 ms) was measured (compare to T_1 = 11.4 ms, giving a linewidth of 14 Hz) [81]. The narrow homogeneous linewidths are an important reason behind the attention these materials have recieved towards constructing a quantum memory.

The homogeneous linewidth as described here determines the narrowest spectral feature. It is important to consider longer timescales for applications in quantum memory. In this regime, the homogeneous linewidth is typically broadened over time by so-called *spectral diffusion*. This effect is caused by fluctuations of each ion's transition frequency due to dynamic fluctuations of the ion's environment, such as fluctuating fields due to spin flips in neighbouring atoms. This effect can be minimised by choosing host materials where all host atoms have small or zero nuclear magnetic moments, e.g. silicates such as Y_2SiO_5. Spin flipping can also be inhibited by applying a static magnetic field (to be discussed in section 3.3), and increasing the coherence time of the optical transition [82].

Another mechanism known to broaden homogeneous lines is called instantaneous spectral diffusion [83]. This occus when an ion in the material changes state through optical excitation or decay, which in turn changes their electric dipole moment. As a result these ions will change their interaction with neighbouring ions, leading to an instantaneous shift of these ions resonance frequencies. To limit the effects of instantaneous spectral diffusion, one can decrease the dopant concentration in the crystal, thus increasing the

average distance between the ions.

3.2.2 Inhomogeneous broadening

Zero phonon lines are inhomogeneously broadened. Combining this feature with atomic frequency combs offers possibilities for ultra-large bandwidth storage. If rare-earth crystals had absorption profiles dictated only by homogeneous broadening, this material would serve as a challenging candidate. However, this is not the case. Since rare-earths doped into crystals is not an ideal lattice of infinite extent, the ions will have slightly different surroundings in the crystal due to local stresses and strains on each ion. This causes the energy levels and transition frequencies to differ slightly from ion to ion. This variation in resonance frequency leads to inhomogeneous broadening of the absorption line. This resultant absorption profile can be seen as the sum of the homogeneously broadened lines of the individual ions. Therefore this gives a material that posesses properties of narrow spectral features, yet having a bandwidth that one can map single photons onto (using photon echo approaches).

A similar kind of broadening occurs for free atoms in a gas, where the resonance frequency of an atom is Doppler shifted, depending on whether the atom is moving towards or away from the light source. In rare-earth materials with a low dopant concentration, the inhomogeneous widths of absorption lines are typically a few GHz, but range from less than 1 GHz up to hundreds of GHz. The linewidth generally increases with increasing dopant concentration [84] as more impurity ions lead to more interactions and to crystal strain. At low temperatures the inhomogeneous broadening dominates the homogeneous broadening, meaning that an individual ion only interacts with light within a narrow part of the inhomogeneous absorption line and that different groups of ions can be addressed by tuning the light source to a particular frequency.

Since the inhomogeneous line is composed of many homogeneous absorbers, the line

has a frequency dependent optical depth. The optical depth at a given frequency, αL, is described by α, the material absorption coefficient, and the crystal interaction length L. Optical depth is given by the population difference in the ground and excited state of the transition of interest (optical here). At a frequency within the inhomogeneous broadening, the amount of absorption is dictated by how many atoms lie within one homogeneous linewidth of the specified frequency. In rare-earth-ions doped into crystals considered for quantum memory applications, high optical depth ($\alpha L >> 1$) is required. One may increase the optical depth by increasing the dopant concentration (at the expense of increasing ion-ion interactions) or sample interaction length.

3.3 Interactions with static fields

It is often necessary to consider the effects of applying static electric or magnetic fields across rare-earth-ion doped crystals. Field application is an important tool in constructing a robust quantum memory as they allow for control of decoherence or triggering re-emission of an absorbed photon. Specifically, application of these fields will cause a shift of the energy levels of the rare-earth-ions, due to their electric and magnetic dipole moments. This can be used to split degenerate levels and to shift spectral features in a controlled way.

The Zeeman shift of an energy level is caused by the interaction of a magnetic moment with a magnetic field. In materials with a quenched electonic magnetic moment, the shift is due to the interaction of the field with the nuclear magnetic moment (i.e. nuclear Zeeman effect) [37]. In materials where an electronic magnetic moment exists in addition, the splitting is enhanced through nuclear spin interactions with the electronic magnetic moment. These shifts may be useful if one were to store atomic population within a nuclear Zeeman level, much in the same way as done using hyperfine levels, as they tend

to have long lifetimes (and coherences) which are increased with larger field strength (i.e. energy level separation larger than phonon excitation energy).

The dependence of magnetic field directions on population dynamics, is a well studied phenomena in rare-earth crystals. For instance in $Tm:Y_3Al_5O_{12}$ (Tm:YAG) [56, 85, 86, 87, 88, 89] for the development of a Λ system (i.e. an excited state coupling two ground states) for mapping of optical coherences or optical pumping. Understanding the interrelationship between field direction, population dynamics, level splittings and decoherence mechanisms is an ongoing task for developing existing materials, and constructing new materials, into quantum memories.

In addition to effects of level splittings due to the electrostatic crystal field (i.e. Stark levels), the Stark effect can enable desirable effects such as reversible dephasing in CRIB and engineering of quantum states through pulse compression and decompression [90]. Free atoms possess a centre of inversion and hence can have no permanent electric dipole moments. However if ions are embedded into a low symmetry site in a crystal, they acquire a permanent electric dipole moment with a given magnitude and direction due to a mixing between electronic states, in general giving the ground and excited electronic states different electric dipole moments.

If an external electric field, $\mathbf{E}$, is applied, the energy of the electronic eigenstates will shift, and if two states have different dipole moments the energy difference between the states will change according to:

$$\Delta\omega = \frac{\chi}{\hbar}\Delta\hat{\boldsymbol{\mu}}_{\boldsymbol{e}} \cdot \mathbf{E} \tag{3.2}$$

where χ is the Lorentz correction factor. This phenomena is known as the DC Stark effect [57]. The largest values of the Stark shift of optical transitions are around 100 $\mathrm{kHz/V{\cdot}cm^{-1}}$ [34].

Chapter 4

Experiments

This chapter presents the main results of the work during my MSc thesis. Since the laboratory was relatively new when I started, I assembled, along with a Ph.D. candidate Erhan Saglamyurek and postdoctoral associate Dr. Cecilia La Mela, the experimental setups described in this chapter. The measurements presented in this chapter were carried out by Erhan and myself. Since this is a quantum optics experiment requiring low temperatures, the setup includes a cryostat along with apparatus used to create, process and detect light. Details of setup construction will be discussed first in this chapter, accompanied by a brief description of the relevant devices used. The subsequent section presents specrtoscopic characterization of a new material for quantum memory: a Ti^{4+}:Tm^{3+}:$LiNbO_3$ waveguide. This includes measurements of the relaxation rates, optical coherence properties, and the Stark effect. It has led to a configuration that permits its use for quantum state storage. Lastly, the second main result of this work is presented: a demonstration of the AFC protocol using broadband light at the single photon level. This includes storage of sub-ns classical and quantum bits, measurements of high fidelity preservation of output modes, and storage of 128 modes at the single photon level. Each result will be accompanied by an analysis, discussion and a brief conclusion.

4.1 Setup

Experimental construction and assembly begins with its heart, the Ti^{4+}:Tm^{3+}:$LiNbO_3$ waveguide that was studied and employed for quantum state storage. Growth and initial characterization of the waveguide sample performed by our collaborators at the University

of Paderborn is mentioned first in this section. The waveguide was operated at three Kelvin so details of the cryostat assembly are introduced next. Light is interfaced with the waveguide via fiber optics connected with apparatus outside the cryostat. This interface is not directly accessible at low temperatures, so a method (developed by our group) of how light was coupled to the waveguide is described. The section concludes with a description of all other important devices employed in the experiments desccribed after this section.

4.1.1 Crystal fabrication

The Ti^{4+}:Tm^{3+}:$LiNbO_3$ waveguide was grown by the group of Professor Wolfgang Sohler at the University of Paderborn in Germany that specialize in producing integrated optics in lithium niobate [91]. To construct the sample, they began with commercially available 0.5 mm thick Z-cut wafers of undoped optical grade congruent lithium niobate (CLN), and cut samples of 12 mm x 30 mm size from these wafers. Tm doping was achieved by in-diffusing a vacuum-deposited (electron-beam evaporated) Tm layer of 19.6 nm thickness. The diffusion was performed at 1130°C during 150 h in an argon-atmosphere followed by a post treatment in oxygen (1 h) to get a full re-oxidization of the crystal. Tm occupies regular Li-sites similar to Er-ions when incorporated in CLN by diffusion [92]. The Tm indiffusion leads to a 1/e-penetration depth $d_{1/e}$ of about 6.5 μm. The maximum Tm concentration of about 1.35×10^{20} cm^{-3} corresponds to a concentration 0.74 mole %, which - according to Ref. [92] - is considerably below the solid solubility of Tm in CLN. The next step involved creation of the waveguides themselves, thus titanium was added to the crystal as to provide the increase in index of refraction relative to Tm:CLN only. This was achieved by first depositing a 40 nm thick titanium layer, using electron-beam evaporation, on the Tm-diffusion doped surface of the substrate. From this layer, 3.0 μm wide Ti stripes were photolithographically defined and subsequently in-diffused at

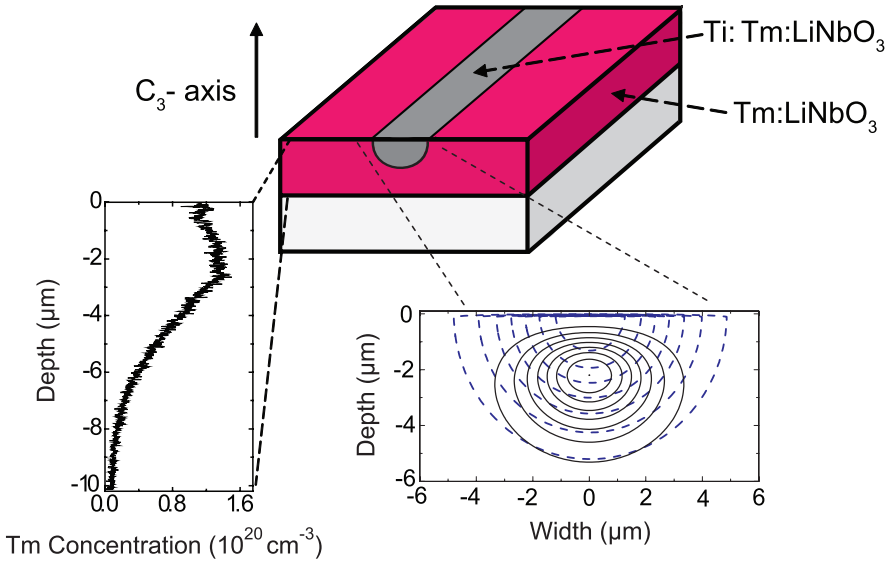

Figure 4.1: Scheme of the waveguide geometry with the measured Tm concentration profile (on the left), and the calculated intensity distribution of the fundamental TM–mode superimposed on the profile of the extraordinary index of refraction induced by the Ti-doping (on the right). The latter data are calculated for 795 nm wavelength. Isolines denote 100%, 87.5%, 75% etc. of the maximum index increase ($\Delta n_{max} = 4.0 \times 10^{-3}$), and the maximum mode intensity.

1060°C for 5 h to form 30 mm long optical strip waveguides. In the wavelength range around 775 nm, the waveguides are single-mode for TE- and TM-polarization (see Fig. 4.1). TE and TM denote tranverse electric and magnetic polarization respectively. To finish the fabrication, the waveguide was cut to 15.7 mm and end faces were carefully polished normal to the waveguide axis.

4.1.2 Cryostat apparatus

A cryostat (Vericold VT4) was used to keep the sample at three Kelvin for the experiments discussed in this thesis. The cryostat, a closed-cycle pulse-tube cooler, keeps two metal plates at croygenic temperatures, one at 50 K and the other at 3 K. The cooling cycle is described as follows. Expansion of compressed helium vapour into the pulse-tube results in heat being drawn away from the cold plates since the tube and plates are in

thermal contact. This keeps any object in contact with a plate at low temperatures once thermal equilibrium is reached. The expanded gas is drawn out of the tube using the rotary valve, back to a water-cooled helium compressor located in another room. During compression, heat is transferred from the helium vapour to the University of Calgary cold water supply. After this the vapour is drawn back to the pulse-tube via the rotary valve.

The waveguide itself is mounted on a titanium tower sitting on the 3 K plate (see Fig. 4.2). Thermal contact is achieved through mechanical pressure and thermal vacuum grease. A ceramic lid holds the crystal in thermal contact with the tower via screws with springs. A resistance thermometer is attached directly to the ceramic lid and reads the crystal temperature. We glued aluminum tape between the ceramic lid and the crystal. It is attached to an external voltage source to allow the application of electric fields for measurements of the Stark effect. To access the nuclear Zeeman levels and reduce spectral diffusion in thulium, the tower assembly sits inside a superconducting magnetic coil that allows generating fields up to two Tesla. The crystal is oriented with its C_3-axis parallel to the magnetic field direction. All electronic wiring connecting to devices outside of the cooler was well thermalized.

Single-mode fiber at 800 nm (OZ Optics) was connected through a home-made vacuum safe connector from outside to inside the cryostat. This allowed light to be externally interfaced. The fiber was thermalized by attaching lengths of single-mode fiber at 800 nm (OZ Optics) directly to the pulse-tube. To couple light in and out of the waveguide we strung fiber inside glass tubes at the input and output ports of the waveguide, see Fig. 4.3. The tubes (and hence the fibers) were positioned using nano-positioning translation stages (Attocube ANP 100). A stage consists of three cubes placed on top of each other, where each cube can be moved in one dimension. The movement is facilitated by piezoelectric actuators that, when voltage is applied to them, move in a 'slip-stick' motion

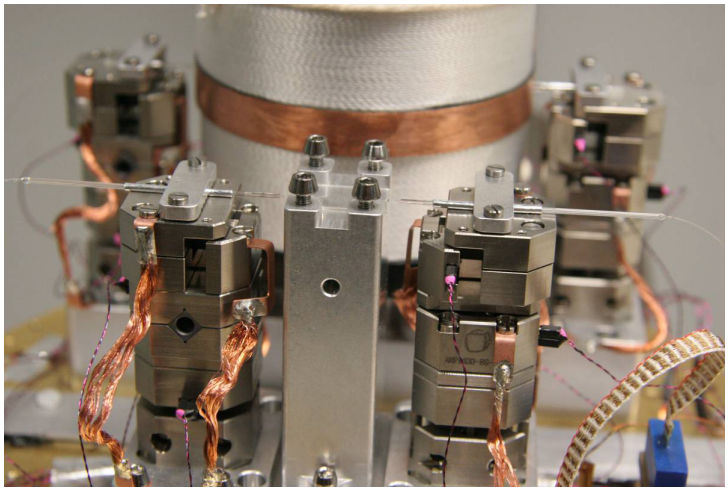

Figure 4.2: Cryostat setup: The rare-earth doped waveguide crystal is mounted on a titanium tower and is cooled down to 3 K by thermal contact with a metal plate. Piezo motors position optical fibers at low temperatures with high precision, thus allowing for efficient coupling to the waveguide. These fibers pass through a home-made vacuum-safe connector from the outside to the inside of the cooler, and are well thermalized before reaching the crystal. The setup shown here is outside of the superconducting coil to display its components clearly. A second identical setup is in the background inside the coil.

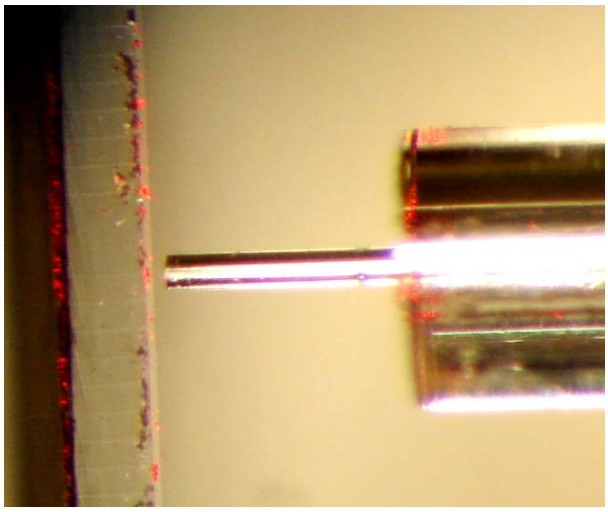

Figure 4.3: A view through a microscope of the fiber-waveguide interface at room temperature. On the left is the Tm:LN crystal containing many waveguides of various diameters. On the right is a single-mode fiber held by a glass tube. This allows selecting and coupling into the 3.5 μm waveguide used for these experiments. The red spots are from injected red light being scattered off crystal imperfections and grit.

(i.e. the piezo is expanded quickly, and when the piezo contracts slowly it translates the cube through friction).

When cooling down the cryostat from room temperature to 3 K, the position of the fibers change due to thermal contractions. This generally results in complete loss of coupling, that can be monitored by sending low intensity light through the fibers and waveguide. Considering a single-mode field dimeter of a few microns, this is not surprising. After many unsuccessful attempts to ascertain coupling, we devised a way to recover transmission through the waveguide blindly and at low temperature. To align both fibers independently with the waveguide we monitored back reflected light from the crystal face using a fiber beam-splitter on the input to the cryostat.

Since the waveguides resided near the top of the crystal, a sudden drop of back reflected light when scanning the fibers in the z-direction allowed locating the waveguide in this z-axis. To locate the waveguide in the y-direction, we positioned non-reflecting paint to both crystal end faces in a region next to the waveguide. The resultant change in back reflection when moving the fiber from crystal face to paint allowed for defining a reference position to align the other y-axis. The last x-axis defines the distance between the fiber tip end and the crystal face. Since a low-finesse Fabry-perot cavity is formed in this region, interference fringes could be seen on the back reflection as this distance is changed. Using broadband light from an optical amplifier (Toptica BoosTA), interference can only be seen when the fibers were close to the waveguide. By positioning each axis on both sides of the waveguide, efficient coupling could be achieved. At room temperature, less than 6 dB loss between input and output of the entire cryostat system was achieved. We allocate these losses to improper fiber assembly away from the waveguide and non-optimized field overlap at the fiber-crystal interface. At low temperature a 10 dB overall loss was achieved due possibly to irreversible contraction of the apparatus, changes in waveguide dimensions or refractive indeces. To reduce this loss, we plan to explore the

effects of different titanium doping concentrations of the waveguide. Furthermore, as a step towards increased robustness we plan on using a crystal that is fiber pigtailed directly.

4.1.3 Equipment

Outside of the cryostat apparatus, we used a different setup for each experiment described in this thesis. When experimental results are discussed in detail, the specific setup used to generate those results will be presented. In general however, both setups featured common elements:

- a laser producing coherent light at a suitable wavelength
- a modulation system shaping the frequency, phase and amplitude of the light
- the waveguide setup cooled to 3 K inside of the cryostat
- a detection system employing photodetectors, avalanche photodiodes and a computer or oscilloscope
- electronic devices, such as a waveform generator, that allowed control of the experiment including timing

In addition to this equipment, a typical setup contains a large number of standard optics components, such as mirrors, lenses, quarter and halfwave plates, beam splitters, mounts, optical attenuators, fiber patchcords, which all sit on an air-supported low-vibration table. Most of the standard components were purchased through Thorlabs [93], with fiber optics purchased from OZ Optics [94].

For a laser source, we used a continuous wave external-cavity diode laser (Toptica DL 100) operating at 795 nm wavelength. Light emission from a laser diode relies upon

injecting a current between n and p layers in the active region of the diode. Current injection produces electron-hole pairs that recombine and emit photons with high quantum efficiency (i.e. the probability that recombination causes photon emission). The semiconductor material band gap, as a function of temperature and carrier density, determines the nominal emitted wavelength. Single wavelength operation of the diode alone requires careful selection of operating temperature in conjunction with the diode laser injection current. However, by using the diode in conjuction with an external cavity, this allows for single-mode operation and tuning to any wavelength within the gain curve of the laser diode. Ideally, the laser diode itself becomes purely a gain element and an external resonator acts as a mode selector, allowing gain for only one mode of the external cavity. Tunability of the laser is achieved by using a diffraction grating in place of the end mirror of the external cavity. Capturing of light at different diffraction angles determines the selected wavelength. There are different laser designs that exploit this tuning method. The grating can be rotated using a fine pitch screw located inside the laser which roughly tunes the wavelength. Continuous wavelength tuning is achieved by applying a voltage to a piezoelectric stack attached to the grating itself. Finer tuning still can be achieved from altering the diode current. This changes the density of charge carriers within the diode, resulting in a change of refraction index within the diode itself. Apart from excellent tuning characteristics, external cavity diode lasers typically have linewidths on the order of 1 MHz over a few milliseconds. To assess the long term stability we measured a drift of tens of MHz in a few minutes for the laser used in this work. This was done using a high finesse Fary-Perot cavity as a frequency reference.

After the laser, the continuous laser beam is intensity modulated to obtain required pulse sequences for the experiment. We employed a 400 MHz acousto-optic modulator (AOM) that allowed pulse shaping, frequency shifting and phase encoding information into the laser light. This device is limited to switching times of 10 ns at best, so for

generation of shorter pulses a 10 GHz polarization modulator (PM) was used in conjuction with a polarizing beamsplitter. For rapidly steering the laser beam into different spatial paths, a fiber-optics based microelectromechanical (MEMS) switch was employed.

An AOM consists of a piezo electric transducer attached to a crystal. A radio frequency signal is sent to the AOM and forces the transducer to vibrate. This oscillation creates an acoustic wave being sent through the crystal causing a periodic modulation of the refractive index. Continuous light is sent into this AOM and diffracted off this acoustic grating. The first order diffracted light is then separated from the non-diffracted beam using an aperature or pick-off mirror. The diffracted light will obtain the properties of the acoustic wave (i.e. the sound wave frequency is added to the laser frequency and phase information of the sound wave is mapped onto the laser beam). Furthermore, the light is intensity modulated by changing the amplitude of the acoustic wave. Using several AOMs in series, or a single AOM in a multiple-pass configuration, a scan bandwidth of hundreds of MHz can be accessed. However the efficiency is usually compromised for frequency tuning by more than 10% of the rated driving frequency of the AOM. In this work, we employed a 400 MHz AOM (Brimrose TEM-400-100-793) driven by a waveform generator through an electrical amplifier, thus allowing for generation of arbitrary pulse sequences.

The polarization modulator used in this work is based upon the principle of the electro-optic effect. If an electric field is applied to a non-centrosymmetric crystal, the refractive index of the crystal changes linearly with the applied electric field amplitude. A higher refractive index results in an increased phase delay for light propagating through the crystal. The π-voltage defines the amount if potential difference that the crystal needs to rotate the phase by 180°. If linearly polarized light is input at an angle to the crystal axis, then the phase of one linear polarization directon is delayed, resulting in an overall polarization rotation of the light. In the setup we employ a commercial modulator

(EOSPACE PM-0K5-10-PFU45-PFU45-800) consisting of an electrode atop a $LiNbO_3$ waveguide. Polarization maintaining fibers are glued to the ends of the crystal where the fiber and crystal axes were rotated by 45°. Since the waveguide is a few microns in width, the π-voltage is 3 V at 1 GHz. This enables the device to be switched quickly with ease, allowing for π phase shifts in 200-300 ps. The modulator was roughly temperature controlled as temperature changes altered the electrooptic coefficient (i.e. relationship between electric field and refractive index) which results in polarization drift. To derive intensity modulation from the polarization modulator we added a polarization beam splitter after the modulator. Since the beam splitter allowed for selecting only a given linear polarization after the modulator, it acted as an intensity discriminator. Therefore, by changing the polarization quickly with the modulator, the beam splitter allowed for generation of pulses with frequencies only limited to the modulator bandwidth (10 GHz here).

To spatially deviate the generated pulse trains, a fiber pigtailed MEMS optical switch was used in the experiment. Using well-understood processes from the integrated circuit industry, a MEMS switch is micromachined from silicon substrates. They range between tens of microns to a millimeter in size and rely upon actuation forces for mechanical movement. The most understood MEMS electrical switches rely upon electrostatic forces that can cause GHz movements with high reliability while being driven by low voltages. The optical MEMS switch consists of an electrically moveable micro-mirror driven by a MEMS switching device. The optical switch used in this work (Thorlabs OSW12-780-SM) was able to switch light of any polarization with high isolation of 100 dB in hundreds of microseconds.

After the waveguide sample, the transmitted light and the echo is detected using a photodetector or an avalanche photodiode (APD) operated at voltages below breakdown. In addition we use an APD that is operated in single photon counting regime, i.e a single

photon detector (SPD). Photodiodes are semiconductor devices that produce a current proportional to the incident light intensity [95]. In principle, one electron-hole pair in the diode can be generated for each incoming photon, provided the photon energy is greater than the energy gap between the valence band and the conduction band in the active region of the diode. In practice, the quantum efficiency, i.e. the probability of a photon generating an electron, is limited to 90% at best depending on material and wavelength. The signal is electronically amplified with tunable gain, if available. Relevant photodetector properties are bandwidth, sensitivity and noise, usually with a trade-off between them. In this work, a sensitive (nW) 10 MHz detector (New Focus 2051), a less sensitive 125 MHz photodetector (New Focus 1801), a fast 1 GHz photodiode (New Focus 1647), or a fast and sensitive 5 GHz detector (Newport AD-200XR) was used.

In a single photon counting APD, the diode is operated under a reverse-bias voltage (past breakdown) that is sufficient to enable avalanche multiplication of the electron-hole pair, resulting in an internal current gain [96]. In this way, signals consisting of few or single photons can be detected. Currently there is much research into developing efficient, high speed, low noise APDs. The most robust and highest performance APD's, like the one used in this work (PerkinElmer SPCM-AQR-14-FC), are based on silicon semiconductors and detect at visible wavelengths. In these diodes quantum efficiencies typically reach 50% with dark count rates around 50 Hz. Dark counts arise from intrinsic electrical or thermal noise stimulating an electron-hole pair when an photon was not detected. APDs also suffer from small detection rates due to the detector dead time or afterpulsing. The dead time occurs because after breakdown the APD needs to be recharged. Afterpulsing results from trapped charge carriers in the diode itself, leading to an avalanche at later times. This is commonly seen when the detector is cooled, usually to reduce dark counts.

To process the information taken from photodection, a 3 GHz (LeCroy wavepro 7300A) or 6 GHz oscilloscope was used with a 10 GS/s sampling rate. When using SPDs, we used a time-to-digital converter (TDC) (ACAM ATMD-GPX) interfaced with a computer. The TDC allowed to convert count rates from photon detection into the time domain to easily interpret the measurements. Thanks goes to Ph.D. student Joshua Slater for programming the electronics and computer interface for the TDC. Electronic control of devices and experimental timing was achieved using a 20 GS/s arbitrary waveform generator (AWG) (Tektronix AWG7102). This allowed programming waveforms to drive the AOM and PM, synchronize the switch or set the TDC start time for example. Since the AWG output was limited to one volt peak-to-peak, electrical amplifiers were used to drive the AOM (Minicircuits ZHL-5W-1) and PM (SHF 826H). In addition, a wavemeter (Bristol 621) was used to set the laser wavelength. It relies on measuring interference fringes of light in a Michelson interferometer and comparing it to that of a stabilized helium-neon reference laser. An optical spectrum analyzer was also employed (Anritsu MS9710C). Its operation depends on a diffraction grating to descriminate the relative spectral intensity the light being measured.

4.2 Spectroscopy of a Ti^{4+}:Tm^{3+}:$LiNbO_3$ waveguide

To successfully implement a quantum memory protocol in a rare-earth ion doped crystal, its spectroscopic properties must be quantified and well understood. It is important to know the limitations of a sample to judge its capabilities as a quantum memory. The quality of a memory starts with its preparation- for AFC a high finesse comb with narrow and high peaks on non-absorbing background is ideal. To assess the possibility to achieve this, one must provide basic spectroscopic information to analyze how capable a given material is for producing a satisfactory memory for quantum repeaters (i.e. having high

efficnecy, bandwidth, etc.). This analysis can be extended to specify exactly what needs to be improved to achieve a better quality memory. For example, a different host crystal, lower temperaure, or less/more doping concentration could change the spectroscopy enough to have a sample satisfy the memory performance criteria. With these ideas in mind, the next section presents first spectroscopic measurements on Ti^{4+}:Tm^{3+}:$LiNbO_3$. We begin by describing the level structure and general crystal properties while highlighting the novelties of this material considering photon echo quantum memory. We then turn to material characterization itself by starting with the waveguide losses and polarization dependence. Spectroscopy of the inhomogeneous broadening is presented next. This allows to assess the material optical depth and for identification of a zero-phonon line. Using spectral hole burning, measurements of the population relaxation dynamics for optical and spin states are then presented. Quantifying optical coherence properties and spectral diffusion is done using photon echoes. These results are discussed next. Finally, electric field control of absorbers is presented by Stark shifting a spectral hole. The strength of this coupling is quantified. This section ends with a brief conclusion on this experiment. More information about these results are in a publication [97] resulting from this thesis.

4.2.1 Ti^{4+}:Tm^{3+}:$LiNbO_3$

In view of photon echo quantum memory, this material combines interesting features arising from the specific rare-earth dopant, the host material, as well as the waveguide structure. As depicted in Fig. 4.4, the thulium (Tm) $^3H_6 \leftrightarrow {}^3H_4$ transition features absorption at 795 nm, which is a wavelength where air has minimal transmission loss, where photon pairs or entangled photon pairs are conveniently created [98, 99, 100, 101], and where high-efficiency and simple-to-operate single photon detectors based on silicon APDs are commercially available [96]. This makes thulium-based quantum memory inter-

esting for applications in quantum communication and linear optical quantum computing for practical reasons alone.

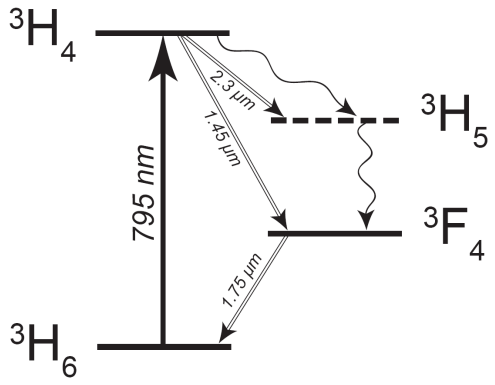

Figure 4.4: Simplified energy level diagram of Tm^{3+}:$LiNbO_3$ showing the electronic levels relevant to this work.

In thermal equilibrium, population is located in the ground state $^3H_6$ level. After optical excitation multiple avenues of decay are available. Decay can occur directly to the long lived $^3F_4$ bottleneck state which could serve as an auxillary storage level for optical pumping. In addition, the bottleneck state, whose energy is situated roughly half way between the $^3H_6$ and $^3H_4$ levels [102], could allow for broadband spectral tailoring [103] since this level is far detuned from the inhomogeneous broadening on the optical transition. This allows us to define a 'branching ratio' in this system which is given by the direct or indirect rate of decay from $^3H_4$ to $^3F_4$ relative to the overall decay rate from $^3H_4$. It is important to have a suitable branching ratio for efficient optical pumping (i.e. remove atomic population from the optical transition). Another relaxation pathway from $^3H_4$ is known to exist, possibly via phonon emission, to the $^3H_5$ level which is known to quickly decay [104, 105].

The rare-earth-ion studied in this work, Tm^{3+}, has an even number of 4f electrons. Therefore the electronic magnetic moment is quenched and thus no hyperfine splitting or electronic Zeeman interactions exist. In addition, the nuclear spin of one-half results in the absence of a quadropole interaction. The application of suitably oriented magnetic

fields results in long-lived nuclear spin levels (i.e. nuclear Zeeman effect in Tm) forming Λ systems which could be used for optical pumping or long-term storage. Storage in the ground state nuclear Zeeman levels can provide a more persistent mechanism than the metastable $^3F_4$ state. In addition, this material features superhyperfine (nuclear Zeeman) interactions, activated upon magnetic field application, due to the nuclear magnetic moments of ^{7}Li (nuclear spin 3/2) and ^{93}Nb (nuclear spin 9/2). The other atomic species, ^{16}O and added ^{48}Ti have zero nuclear spin, therefore do not contribute to this interaction.

During sample fabrication, Tm^{3+} replaces Li^+ in the $LiNbO_3$ lattice, resulting in the ions experiencing an axial symmetry about the crystal's so-called C-axis (C_3 symmetry within the lattice). Yet other studies in bulk Tm^{3+}:$LiNbO_3$ [106] have suggested that this description might not be so straightforward considering possibilities for symmetry deviations. This may account for large inhomogeneous linewidths for optical and spin transitions, and variations of spectroscopic properties acrosss the inhomogeneous line, particularly with application of a magnetic field [106]. To add to the complexity, the sample studied here contains added titanium. Future investigations should uncover effects of adding this dopant.

Due to the lack of inversion symmetry, lithium niobate ($LiNbO_3$) crystals feature non-linear effects [107]. The crystal symmetry also results in permanent electric dipole moments for rare-earth states, i.e. the possibility to externally control resonance frequencies via Stark shifts. Low-temperature properties of rare-earth doped $LiNbO_3$ have been characterized in [108, 109, 110, 111, 112], e.g. for the development of radio-frequency analyzers [113]. Given its non-linear properties, $LiNbO_3$ has become an important material for the telecommunication industry. Procedures to implement waveguides, either through proton exchange [114], or Titanium indiffusion [115], have been well developed, allowing for simple integration with fibre-optics components. In addition, given their small transverse dimensions of 5-10 μm, traveling wave electrodes can be spaced closely,

resulting in commercial intensity and phase modulators with switching π-voltages of only a few volts, and switching times below 100 picoseconds [116].

For photon-echo quantum memory, these properties promise simple integration with fibre quantum networks, sub-ns Stark shifting (for CRIB), and large Rabi frequencies, which will benefit optical pumping procedures in all photon-echo quantum memory protocols. In addition, the unique spectroscopic characteristics (e.g. optical shelving $^3F_4$ level, magnetic sublevels) and exotic characteristics (from added Ti or spectroscopic variations across the inhomogeneous line) make Ti^{4+}:Tm^{3+}:$LiNbO_3$ waveguide attractive for implementing quantum memory and deeper spectroscopic analysis. So far, low-temperature spectroscopic investigations of Tm doped crystals have mostly concentrated on Tm:YAG (see also [82]), and, very recently, bulk Tm:$LiNbO_3$ [104, 106, 109]. For Tm:YAG, they have recently led to implementations of the AFC protocol [117, 118]. $LiNbO_3$ waveguides have been used for studies relevant to quantum memory in [25, 110, 119, 120] where Er^{3+} serves as the rare-earth impurity.

Since this material is a rectangular waveguide, it has propagation losses and a polarization dependence of transmission. Our collaborators in Paderborn measured waveguide losses at room temperature via free space optics to be 0.2 dB/cm for both transverse electric (TE) and magnetic (TM) polarizations using a well understood method [121]. We measured, using off-resonant laser light, strong polarization dependent transmission at 3 K. The exact origin of this difference compared to the room temperature measurements needs further investigation. However, we observed that for polarizations warranting high waveguide transmission, the laser light interacted strongly with the inhomogeneous absorption profile (i.e. we maximally projected the electric field onto the electric dipole moment). This configuration (closest to TM propagation) is where all measurements have been taken. Spectroscopy at other polarizations needs to be further investigated.

4.2.2 Spectroscopy of inhomogeneous broadening

Reversible atom-light interaction requires absorption on the transition between the lowest lying Stark levels in the ground and excited electronic states. To gain information about $^3H_4$ and $^3H_6$ Stark splittings, we injected weak, broadband, polarized light into the waveguide. Using wave plates, we set the polarization close-to TM, and measured power spectra of the transmitted light using an optical spectrum analyzer.

Room temperature characterization– For comparision, we include this measurement from our German collaborators. The transmission through the waveguide for TE and TM-polarized light is shown in Fig. 4.5. It has been normalized to the incident spectral power density of the broadband tungsten lamp used for this experiment. They observed broad absorption, reflecting different transitions between Stark levels in the $^3H_6$ and $^3H_4$ multiplets (superimposed with inhomogeneous broadening), and the thermal distribution of the population in the electronic ground state. In addition, a strong polarization dependence of absorption was observed, confirming previous studies performed on bulk crystals [104, 105].

Low temperature characterization- Using a low-power broadband source, a similar measurement at low temperature resulted, for close-to TM polarization, in the absorption profile shown in the inset of Fig. 4.6. Due to the large optical depth of our sample, reflecting redistribution of population in the ground state Stark levels, we observe an almost flat-lined spectrum.

To resolve the Stark splittings, coherent laser light was coupled into the waveguide, and its frequency was swept between 791 and 796 nm in 0.1 nm steps. The laser intensity was optimized to resolve different Stark transitions after having partially bleached the absorption line. The resulting optical depth, shown in the main plot of Fig. 4.6, was determined at each measured wavelength upon normalization to the probe light. Using results from [106, 122], we can identify four transitions between the ground and excited

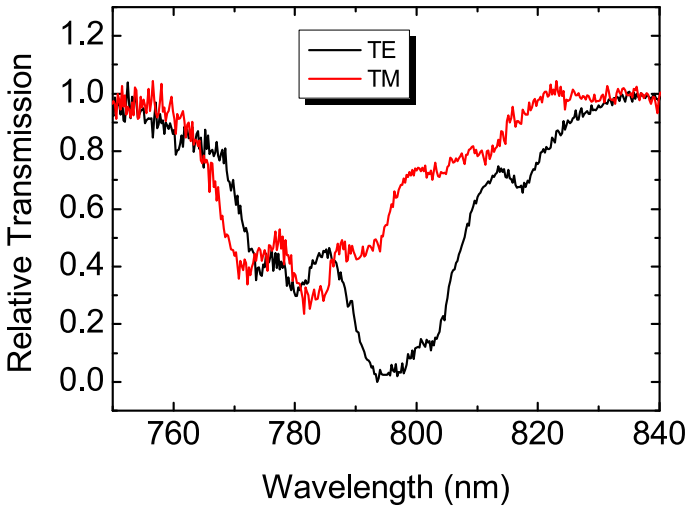

Figure 4.5: Relative transmission through the Ti:Tm:$LiNbO_3$ waveguide for TM- and TE-polarization as a function of wavelength. The transmission has been normalized to the incident light spectral power density. The resolution bandwidth of the optical spectrum analyzer used in this experiment was 2 nm due to the low spectral power density of the thermal radiator. This figure is taken from Ref. [97].

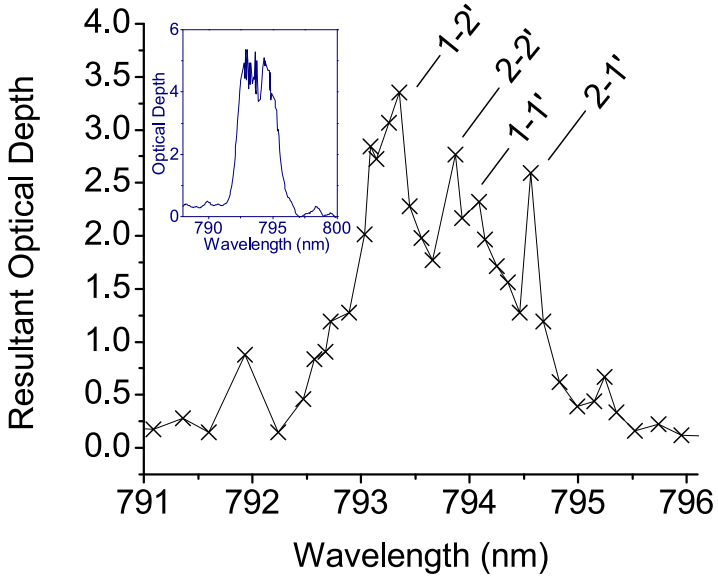

Figure 4.6: Main figure: Absorption profile (after partial bleaching) at 3 K obtained using a single frequency laser. Indicated are transitions between different Stark levels: 1 and 2 denote the lowest energy levels within the $^3H_6$ multiplet, primed labels represent the lowest $^3H_4$ levels. Inset: The same inhomogeneous broadening probed using weak broadband light.

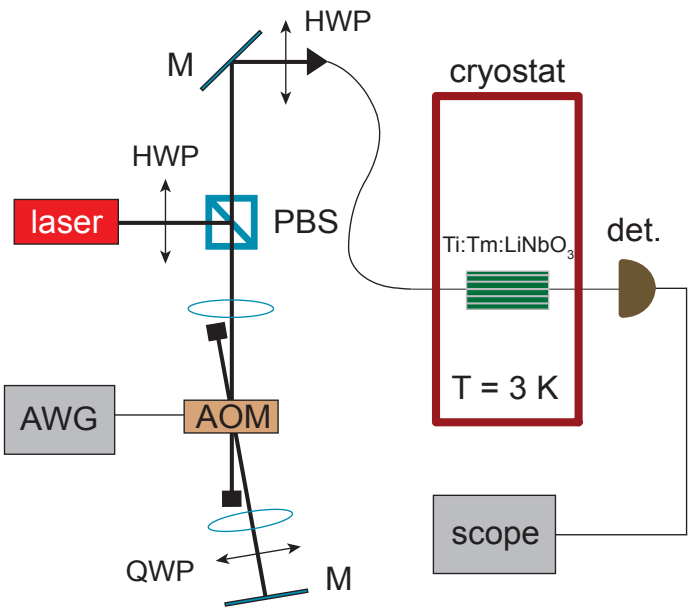

Figure 4.7: Schematic of the experimental setup used for the narrow-band measurements at cryogenic temperature. HWP: half-wave plate; QWP: quarter-wave plate; PBS: polarization beam splitter; AOM: acousto-optic modulator; AWG: arbitrary waveform generator; M: mirror; det.: detector; scope: oscilloscope.

state Stark multiplets, with splittings of 0.48 ± 0.05 nm and 0.93 ± 0.05 nm, respectively (i.e. 7.6 ± 0.8 cm^{-1} and 14.7 ± 0.8 cm^{-1}, respectively). This indicates the presence of a zero-phonon line in the high wavelength region. According to calculations taking into account the observed splittings, only a small fraction of atomic population, $\sim$1%, occupies higher energy Stark levels of the ground state multiplet.

4.2.3 Experimental setup for narrow-band spectroscopic investigations

A schematic of the experimental setup used for the low-temperature spectroscopic measurements described hereafter is depicted in Fig. 4.7.

A continuous wave, external cavity diode laser was tuned to 795.520 nm wavelength, where we found optical coherence properties of our sample in the absence of a magnetic field to be promising. The laser's linearly polarized output was frequency and intensity modulated using a 400 MHz AOM in a double-pass configuration, driven by a 20 GS/s

AWG and an electrical amplifier. This allowed the creation of optical pulses with peak powers up to ∼4 mW and durations between 20 ns and 500 ms for photon-echo sequences and spectral hole burning. Here and henceforth, all pulse powers are specified at the input of the cryostat. After passing a $\lambda/2$ wave plate, the light was coupled into a single-mode optical fiber, and sent into the 3.5 μm wide, single-mode Ti:Tm:$LiNbO_3$ waveguide. The light's polarization, which could be partially controlled using the wave plate, was set as to maximize the transmission, i.e. as to minimize the distance to TM. The overall coupling loss, from before to after the cryostat, was 15 dB for the following measurements in this section. Transmitted pulses and echoes were detected using either a sensitive 10 MHz, or a 125 MHz photodetector, which was then connected to a 3 GHz bandwidth oscilloscope with 10 GS/s sampling rate. All measurements conducted at zero magnetic field were repeated every 100 ms, and generally averaged 300 times. Upon magnetic field application, the repetition period was set to 60 s, which was required to avoid accumulation effects, and the number of averages was reduced to 25.

4.2.4 Population relaxation dynamics

To optimize optical pumping strategies, and determine possibilities for long-term storage, it is important to examine the relaxation avenues and population dynamics in atomic levels involved in the light-atom interaction. The level scheme for thulium doped crystals in the case of zero magnetic field is depicted in Fig. 4.4. Upon excitation of the lowest lying Stark level within the $^3H_4$ manifold, atoms will eventually decay back to the ground state, either directly, or via the $^3H_5$ and $^3F_4$ levels. As the radiative lifetime of the $^3H_5$ level is short compared to the lifetimes of the $^3H_4$ and $^3F_4$ levels [104], we model atomic decay, i.e. radiative lifetimes and branching ratio (given by the rate of decay from $^3H_4$ to $^3F_4$ relative to the overall decay from $^3H_4$), using a simplified three-level scheme comprising only the $^3H_6$ ground state, the $^3F_4$ bottleneck state, and the $^3H_4$ excited state.

As material absorption is dependent upon population differences between the states coupled by the probe light, we can assess population dynamics through time-resolved spectral hole burning. To this end, we first transfer population to the excited state using a 5-10 μs long *burning* pulse with peak power of 7 μW, and then probed the shape and depth of the created spectral hole after a *waiting time* ranging from 10 μs to 15 ms using a chirped *reading* pulse. The power of the reading pulse, around 1 μW, was chosen as to not alter the population distribution created by the burning pulse. Fig. 4.8 depicts the time dependent depth of the spectral hole, which we found to be proportional to the hole area (i.e. the effect of spectral diffusion, leading to a waiting-time-dependent hole width, was not visible in this measurement).

We model the decay using three-level rate equations, leading to

$$\frac{\Delta \mathrm{d(t)}}{\Delta \mathrm{d(0)}} = (1-\mathrm{B})\mathrm{e}^{-\mathrm{t}/\mathrm{T}_{1e}} + \mathrm{B}\mathrm{e}^{-\mathrm{t}/\mathrm{T}_{1b}} \tag{4.1}$$

where Δd(t) denotes the reduction of optical depth d = αL at the centre of the spectral hole at time t after burning, α is the absorption coefficient, L the sample length, T_{1e} and T_{1b} are the T_1 lifetimes of the excited and bottleneck states, respectively, and $B = \frac{\beta}{2}\frac{T_b}{T_b - T_e}$ identifies the branching ratio β. We find the time-dependent population difference to be characterized by a fast exponential decay with a lifetime of $T_{1e} = 82 \pm 2$ μs, and a slower exponential decay from $^3F_4$, characterized by $T_{1b} = 2.364 \pm 0.198$ ms. Both decay constants agree with previous measurements [123]. Furthermore, we find a branching ratio of 0.436 ± 0.017.

We also performed hole burning studies under application of magnetic fields between 100 and 1250 Gauss, oriented parallel to the crystal C_3-axis. For these measurements, we increased the burning time to 500 ms, and varied the waiting time between 100 ms and 6 s so that population in the $^3H_4$ and $^3F_4$ levels could be ignored. As depicted in Fig. 4.9, this allowed the observation of spectral holes persisting during waiting times of up to

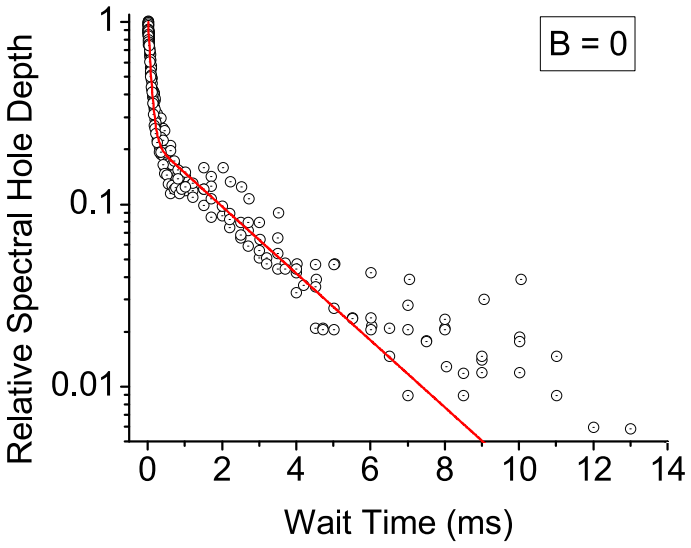

Figure 4.8: Spectral hole decay under zero magnetic field. Plotted circles denote the normalized spectral hole depth as a function of the waiting time between burning and reading pulses. Two exponential decays are easily identified, yielding radiative lifetimes of 82 μs and 2.4 ms for the $^3H_4$ and $^3F_4$ levels, respectively. The branching ratio into the $^3F_4$ level is approximately 44%.

seconds, with the decay of the hole depth being again well described by the sum of two exponentials. Furthermore, the two decay times change with magnetic field, as depicted in Fig. 4.10. This indicates the appearance of two magnetic field dependent atomic levels with long lifetimes, and suggests maximum lifetimes at magnetic fields around 600 G.

While we have not been able to identify the levels involved in the long-term storage, e.g. through the observation of additional holes or anti-holes that indicate field-induced level splitting [48], we believe that $^3H_6$ nuclear hyperfine levels play a role. Note that 90 MHz splitting has been reported at 700 G [109]. We point out that the direct relaxation between different nuclear spin states in the excited and ground state multiplets is likely to be forbidden in the case where the magnetic field is parallel to the crystal C_3-axis [86]. The observed long-lived storage thus probably involves a (spin mixing) relaxation pathway including the $^3H_5$ level. The role of superhyperfine interaction of thulium ions with neighboring lithium or niobium ions, leading to level splitting of $\sim$1 MHz at 700 G

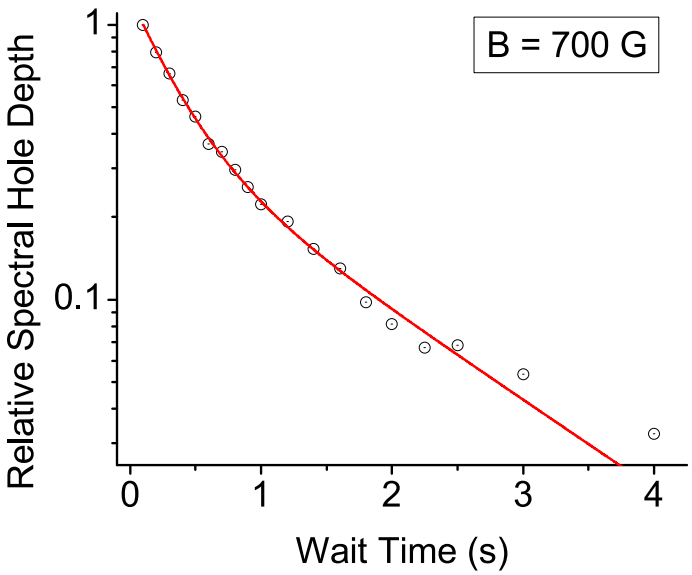

Figure 4.9: Spectral hole depth as a function of the waiting time for a magnetic field of 700 G. The observation of two exponential decays indicates the existence of long-lived, ground state sub-levels.

[109], cannot be assessed from our measurements and requires more investigations.

Furthermore, relaxation between different ground states, which gives rise to the curves shown in Figs. 4.9 and 4.10, is likely to involve several contributions, including spin-lattice relaxation, spin-spin flip flops between neighboring Tm ions, or interactions of Tm ions with other magnetic impurities [81, 124, 125, 126, 127, 128]. Further studies at different temperatures and with crystals with smaller Tm ion concentration are being considered.

To summarize this section, we have observed a short lifetime of the $^3H_4$ level compared to the $^3F_4$, and the $^3H_6$ sub-levels. We have also identified a large branching ratio from $^3H_4$ to $^3F_4$. These observations identify two potential approaches to spectral tailoring, either involving the bottleneck state (maybe taking advantage of stimulated emission [129, 130]), or the magnetic field dependent ground states as an auxiliary state. In this context, the existence of the bottleneck state is of particular interest. Indeed, due to the large energy gap relative to the $^3H_6$ and $^3H_4$ electronic levels, population pumped into this state during spectral tailoring does not interact with light coupling the ground and

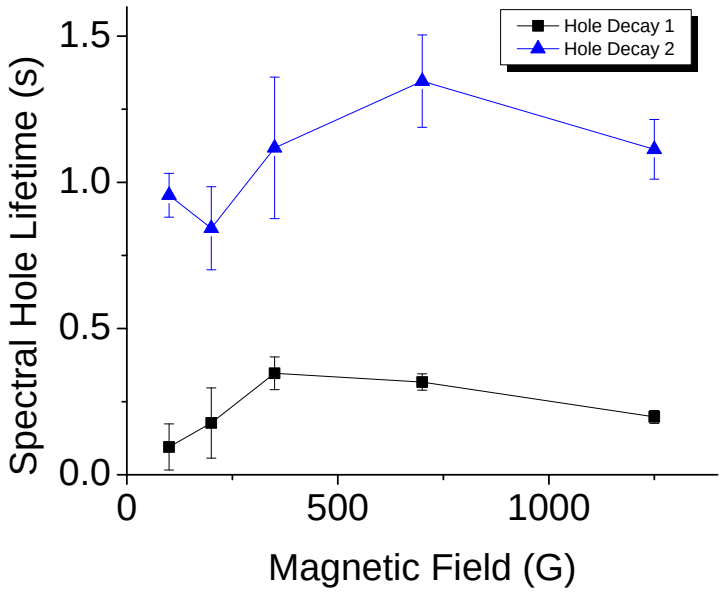

Figure 4.10: Magnetic field dependence of the two decay times extracted from measurements of the spectral hole depth as a function of the waiting time. The case B = 700 G is shown in Fig. 4.9.

excited states. This allows tailoring of the initial absorption line over a spectral interval that is in principle only limited by the inhomogeneous broadening of the $^3H_6 \leftrightarrow {}^3H_4$ transition, and not by energy spacings in the ground or excited levels [131]. In other words, use of the bottleneck state for optical pumping could allow storage of short pulses of light with spectral widths exceeding GHz. Future work includes optimizing optical pumping strategies to achieve efficient population transfer into this level.

Furthermore, it may be possible to reversibly map optically excited coherence (on the $^3H_6 \leftrightarrow {}^3H_4$ transition) onto $^3H_6 \leftrightarrow {}^3F_4$ coherence, or long-lived ground state coherence. However, more investigations are required, for instance concerning the nature of the coupling between the $^3H_4$ and $^3F_4$ states (e.g. studies at different temperatures), or the possibilities for a Raman transfer into $^3H_6$ ground states.

4.2.5 Optical coherence and spectral diffusion

For photon-echo quantum memories, the initial inhomogeneous absorption line must be tailored into one or more narrow lines using frequency-selective optical pumping. In the case of CRIB, the width of the resulting spectral feature determines the time quantum information can be stored in optical coherence [132]. For AFC, it determines the spacing of the teeth in the comb structure, which, in turn, sets the storage time in optical coherence [40]. Material dependent constraints to this time arise from the homogeneous line width Γ_h, limited by the radiative lifetime: $\Gamma_h^{nat} = 1/(2\pi \mathrm{T}_{1e}) \approx 1.9$ kHz, phonon broadening [80], as well as long-term spectral diffusion [81, 133, 134].

To assess the short-term homogeneous line width, we employed two-pulse photon-echoes. Two 20 ns long pulses, with peak powers ~ 3 mW that maximized the observed echo, were sent into the thulium waveguide, and the relative *delay* was varied from 100 ns to 1.8 μs in steps of 25 ns. Fig. 4.11 depicts the resulting peak echo powers for the case of zero magnetic field. We fit the decay of the peak echo intensity I (which is proportional to power) with the Mims expression [135]:

$$\mathrm{I} = \mathrm{I}_0 \exp(-4\mathrm{t}/\mathrm{T}_2)^x \tag{4.2}$$

where I_0 denotes the maximum echo intensity, T_2 is the coherence time and x characterizes spectral diffusion. The fit revealed a coherence time of 1.580 ± 0.008 μs, equivalent to a homogeneous line width of $\sim$200 kHz, and a spectral diffusion parameter x of 1.072 ± 0.009. We obtained similar results for non-zero fields up to 250 Gauss. This indicates that the short-term homogeneous line width at 3 K is dominated by phonon scattering.

Beyond the short-term homogeneous line width, the narrowest spectral feature that can be generated through optical pumping is limited by spectral diffusion. The three pulse photon-echo (3PPE) is a useful tool to investigate spectral diffusion [81].

We performed a series of 3PPE experiments to probe spectral diffusion in our sample.

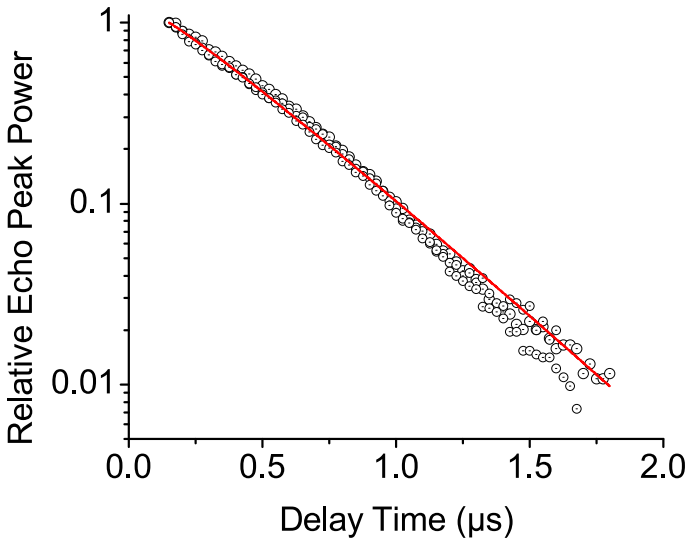

Figure 4.11: Two pulse photon-echo peak powers measured under zero magnetic field. Plotted circles are normalized echo powers as a function of the delay time between the two pulses. Fitted is the Mims expression giving a coherence time of 1.6 μs with nearly absent spectral diffusion.

All experiments were carried out at zero magnetic field. In the measurements, for three different *delay* settings between the first two pulses, we varied the *waiting* time, i.e. the time between the second and the third pulse, from 1 μs to 400 μs with 5-10 μs increments. The echo peak power was measured for each delay and waiting time, and each set of measurements (i.e. measurements with a specific delay time) was normalized to the echo peak power at 1 μs waiting time. The results are illustrated in Fig. 4.12.

To interpret the data, we employed the spectral diffusion model discussed in Ref. [81]. In this model, the peak intensity I of the stimulated echo is determined by the relative dephasing during the delay time t_D, the decay of the excited level population during the waiting time t_W, and diffusion mechanisms which broaden the line into the time-dependent effective line width Γ_{eff}. In its general form, the 3PPE intensity can be written as:

$$I(t_W, t_D) = I_0 F(t_W) \exp\{ -4\pi t_D \Gamma_{eff}(t_D, t_W) \} \tag{4.3}$$

where I_0 denotes the maximum echo intensity, $F(t_W) = (1 - B)e^{-2t_W/T_{1e}} + Be^{-2t_W/T_{1b}}$

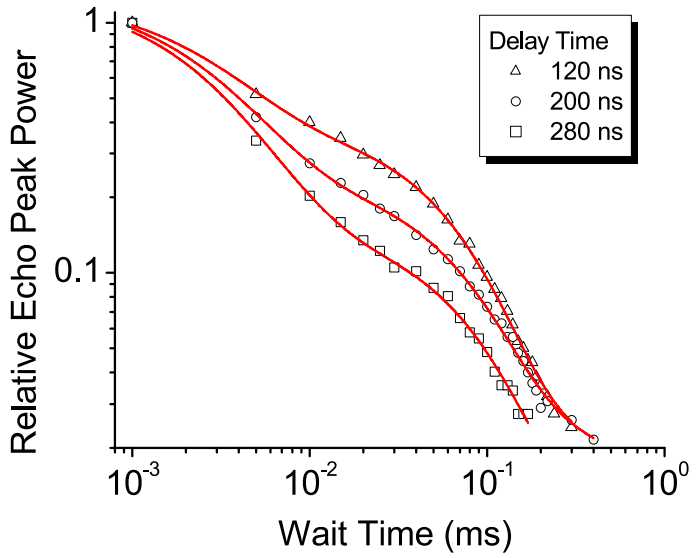

Figure 4.12: Decay of stimulated echo with waiting time for delay times of 120 ns (triangle), 200 ns (circle) and 280 ns (square), respectively.

describes the population decay during t_W, and B is defined as in Eq. 4.1. The effective line width describes spectral diffusion during both the delay and waiting time, and is given by:

$$\Gamma_{eff}(t_D, t_W) = \Gamma_0 + \frac{1}{2}\Gamma_{SD}\left[Rt_D + (1 - \exp(-Rt_W))\right] \tag{4.4}$$

where Γ_0 is the short-term line width in absence of spectral diffusion, and Γ_{SD} denotes the maximum additional line width due to spectral diffusion, which occurs at rate R.

To fit our data, we fixed the bottleneck level lifetime to 2.4 ms, obtained through the spectral hole burning measurements discussed above. This was required due to the echo intensity reaching the noise level after 200 μs, which is too short for the fit to generate a reliable lifetime. By setting $t_W = 0$, we extracted an intrinsic homogeneous line width of Γ_0 =152 $\pm$ 2 kHz via Eq. 4.3, in reasonable agreement with the result of $\sim$ 200 kHz found via Eq. 4.2. Fitting all delay settings yielded an average excited level lifetime and branching ratio of 83 $\pm$ 8 μs and 0.23 $\pm$ 0.03, respectively, in reasonably good agreement with the more reliable values obtained from the spectral hole burning measurements.

Furthermore, the fit yielded $\Gamma_{SD} = 930 \pm 51$ kHz and a spectral diffusion rate of 227

± 24 kHz, and the diffusion model thus predicts that the effective line width

$$\Gamma_{eff}(t_W) = \Gamma_0 + \frac{\Gamma_{SD}}{2}\left[1 - \exp\{-Rt_W\}\right] \tag{4.5}$$

saturates at around 630 kHz after a waiting time of ∼50 μs. When assessed through spectral hole burning, this leads to a homogeneous line width of $\Gamma_0 + \Gamma_{SD}$=1082 kHz [136].

To verify this prediction, we performed another series of spectral hole burning measurements with burning and waiting times of 5 μs and 50 μs, respectively. Varying the power of the burning pulse from 400 to 4 μW, and extrapolating the hole width to zero burning power [54], we find a homogeneous line width of 1.5 ± 0.1 MHz. Taking into account laser frequency jitter of ∼ 1 MHz, this is consistent with the prediction from the spectral diffusion model.

Summarizing results of this section, we have identified spectral diffusion as the limiting factor for storage of quantum information in optical coherence in Ti:Tm:$LiNbO_3$. For instance, assuming an AFC with 3 MHz teeth spacing, the storage time in optical coherence would be limited to ∼ 300 ns. We expect that the application of a magnetic field and the decrease of temperature will lead to an improvement of the short-term linewidth along with a reduction of spectral diffusion, similar to what has been observed for Tm:$LiNbO_3$ bulk crystals [106].

4.2.6 Stark effect

Electric field control, governed by the DC Stark effect, can constitute a key ingredient in photon-echo quantum memory and quantum information processing (e.g. it is critial for controlled and reversible broadening of narrow lines in CRIB). To observe the shift in resonance frequency for different electric fields, we first burned a spectral hole, then applied a variable voltage parallel to the crystal C_3-axis, and assessed the displacement of the hole using a weak, chirped, read pulse, as detailed in [110].

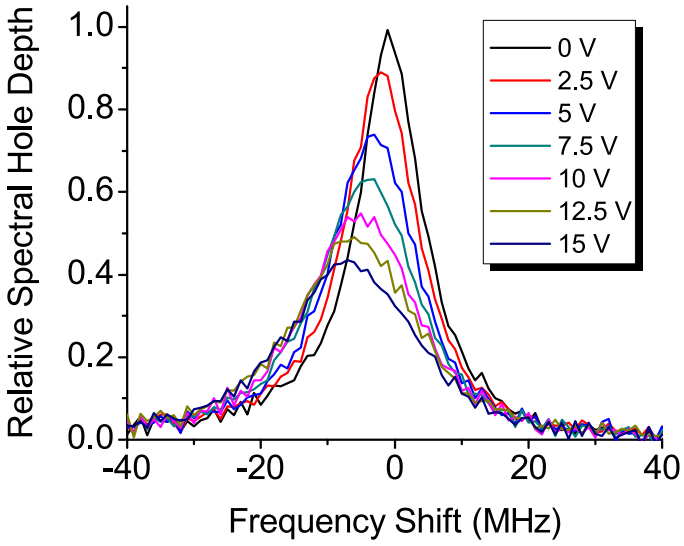

Figure 4.13: Change of a spectral hole under application of different voltages. We attribute the broadening of the spectral hole with increased voltage to the large inhomogeneity of the electric field at the beginning and end of the $LiNbO_3$ waveguide.

As shown in Figs. 4.13 and 4.14, we observe a linear frequency shift of 24.6 ± 0.7 kHz·cm/V. For example, an electric field of 100 V/mm leads to a displacement of the resonance frequency by 25 MHz. In the case of a Tm waveguide, where electrodes can be spaced as closely as 10 μm, this requires the application of 1 Volt. Since low voltages can be switched rapidly with ease, waveguides provide the ability to reversibly broaden and manipulate absorbers within hundreds of picoseconds. We attribute broadening of the hole to electrode fringing effects due to its crude design.

4.2.7 Conclusion

To conclude, our findings demonstrate the suitability of Ti:Tm:$LiNbO_3$ waveguides cooled to 3 K for implementations of photon-echo quantum memory protocols. Level structure, lifetimes, and branching ratios allow tailoring of the natural, inhomogeneously broadened absorption profile – either via optical pumping into the $^3F_4$ bottleneck state (then possibly allowing storage of nanosecond pulses), or into one of the long-lived ground states that

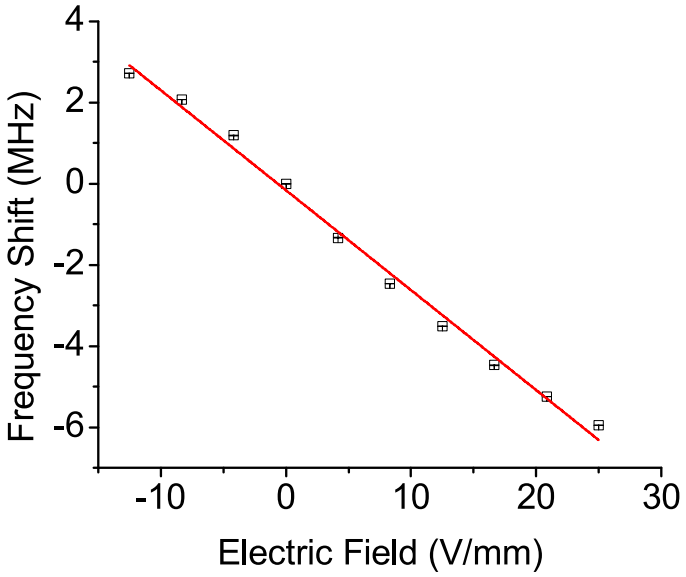

Figure 4.14: Shift of transition frequency of the center of a spectral hole as a function of applied electric field, yielding a shift of 24.6 ± 0.7 kHz·cm/V.

appear under the application of magnetic fields. The minimum width of spectral holes of around one MHz, as determined by spectral diffusion, will limit storage of quantum information in optical coherence to roughly a hundred nanoseconds. While longer times may be achievable at lower temperature, this is still sufficient for mapping coherence onto long-lived ground state coherence, as Rabi frequencies exceeding hundred MHz can be obtained, due to the high power densities achievable inside waveguiding structures. We point out that ground state coherence of 300 μs has been reported for Tm:YAG [89], but investigations for Ti:Tm:$LiNbO_3$ remain to be done. Finally, the existence of a linear Stark shift, together with the possibility to space electrodes closely, allows shifting of resonance frequencies by more than 100 MHz within sub-nanosecond times, thus enabling novel frequency control techniques.

Interestingly, the lifetimes and branching ratio found in our study differ from those reported for Tm:$LiNbO_3$ bulk crystals probed at 794.22 nm wavelength and 1.7 K [106, 109]. The difference could be due to the addition of titanium to our sample, which may alter radiative or non-radiative decay channels [111], to wavelength-dependent spectroscopic

properties as suggested in [106], or to concentration dependence [137].

4.3 Broadband AFC at the single-photon level

Simultaneously satisfying all quantum memory criteria, as specified in Chapter 1, remains an open and challenging persuit. Currently, rare-earths doped into solids hold great promise not only for their material properties, but also due to their theoretical development of protocols suited for these materials- starting with the well-understood traditional photon echo. Separate experiments have already demonstrated storage times of seconds [28], 69% efficiency [42], 100 MHz bandwidths [138], multimode storage of 64 modes [138], mapping of photons of telecom wavelengths [139], and with greater than 90% fidelity [140]. In the following experiment, we employ the studied Ti:Tm:$LiNbO_3$ waveguide to exceed the current benchmarks in bandwidth and multimode capacity. In addition, this experiment is performed in a waveguide: a material of simple and robust design. Specifically we demonstrate mapping of sub-ns photonic wavepackes containing on-average less than one photon on a $\sim$ 1 GHz wide AFC. This allows for a large multimode capacity, from which we demonstrate storage of 128 modes simultaneously. This work marks the first demonstration of a light-matter interface at the single photon level using a waveguide. These findings establish possibility for high bandwidth, Gigabit per second, and integrated quantum memory for future quantum communication networks.

After describing the experimental setup, the results will be presented as follows. We introduce the optical pumping method and show measurement of the comb structure for narrow-band multimode storage of classical light. We then show results from extending the preparation sequence to larger bandwidths and storage of sub-ns weak photon fields (i.e. storage of broadband qubits with less than one photon per pulse). An average fidelity of $\sim$ 98% is obtained by analyzing the error rates in storage of a large variety

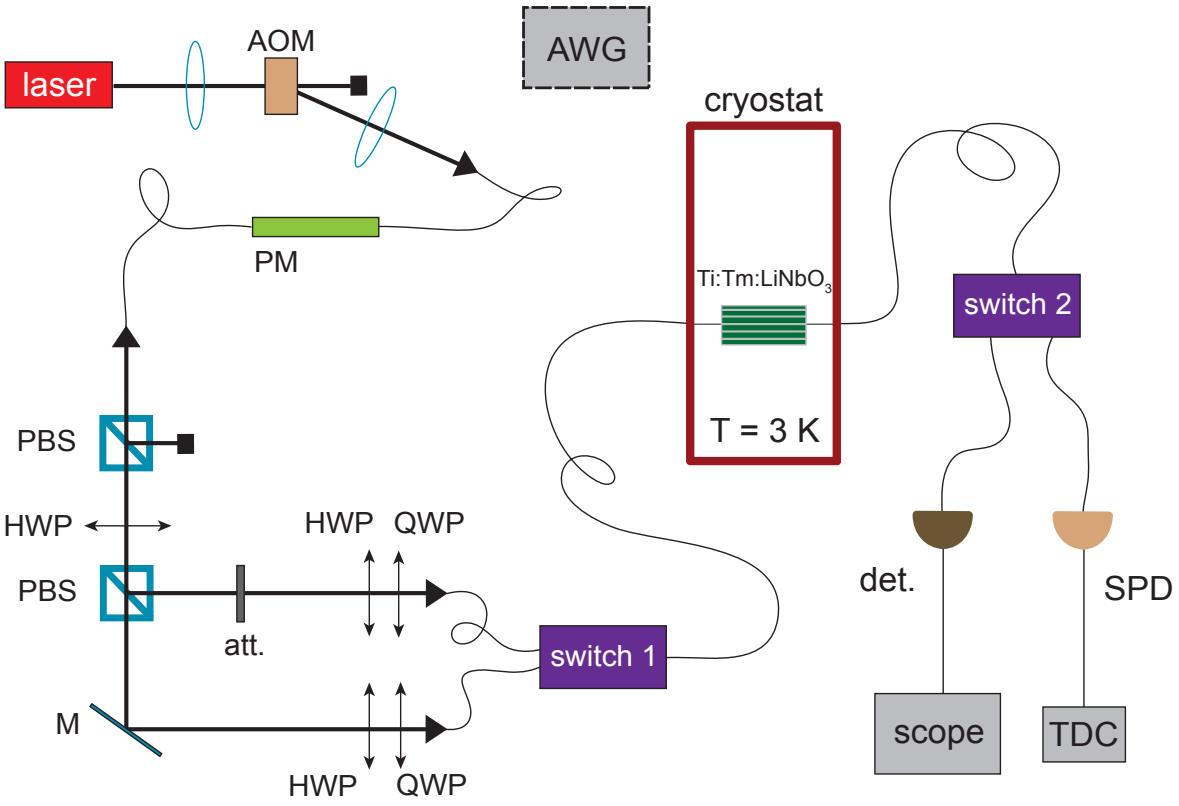

Figure 4.15: Schematic of the experimental setup used for demonstration of broadband storage using AFC. HWP: half-wave plate; QWP: quarter-wave plate; PBS: polarization beam splitter; AOM: acousto-optic modulator; AWG: arbitrary waveform generator (connections not shown); PM: polarization modulator; M: mirror; att.: optical attenuator; det.: detector; SPD: single photon detector; scope: oscilloscope; TDC: time-to-digital converter.

of qubit states. Finally, the simultaneous storage of 128 weak modes is presented. This section ends with a brief conclusion.

4.3.1 Experimental setup

A schematic of the experimental setup used for this experiment is depicted in Fig. 4.15.

The continuous wave external cavity diode laser was tuned to 795.5 nm wavelength. The laser's linearly polarized output was intensity modulated by a 400 MHz AOM. This allowed creation of optical pulses with peak powers up to ∼1 mW and durations between

20 ns and 100 μs for optical pumping and probing the AFC. All powers are specified at the input of the cryostat. To further intensity modulate, light was coupled into a PM. In conjunction with a PBS this allowed reducing the temporal duration of the pulses to $\sim$ 300ps. After modulation, A HWP and PBS allowed to proportion light intensity into two parallel paths. In one path an optical attenuator was placed to regulate pulse intensities to less than one photon per pulse. Both paths contained a HWP and QWP to fully control the linearly polarized input. Both paths were coupled into single-mode fiber and combined at a MEMS switch. The light was then sent into the 3.5 μm wide, single-mode Ti:Tm:$LiNbO_3$ waveguide. The light's polarization, which could be controlled using the wave plates, was set as to maximize the transmission, i.e. as to minimize the distance to TM. The overall coupling loss, from before to after the cryostat, was 10 dB. Behind the cryostat, transmitted and echo pulses passed through another MEMS switch that directed strong light towards a 1 GHz, 2 GHz or sensitive 0.1 GHz photodetector, and weak light to a SPD. The photodetector was connected to a 6 GHz bandwidth oscilloscope with 10 GS/s sampling rate, while the SPD was connected to a TDC that was interfaced with a computer. The AOM, PM, switches and TDC were all driven by an AWG with a 20GS/s sampling rate. All measurements were conducted with a magnetic field (directed parallel to the C_3-axis) of approximately one hundred Gauss, depending on the storage time employed.

4.3.2 AFC for classical data storage

As a first demonstration of a quantum memory protocol in a waveguide, we generate an 80 MHz wide AFC and probe it by sending 20 ns (FWHM) pulses to be stored, or by frequency scanning the grating to reveal its structure.

At this point we will introduce the method of spectral tailoring and optical pumping used to generate the AFC. The most efficient comb requires preparing many narrow

evenly speaced peaks in frequency, each having a large optical depth, on a non-absorbing background. This comb is difficult to generate. A much simpler comb has a sinusoidal modulation of the inhomogeneous broadening. This can be tailored by sending a 'pulse pair' into the ensemble with pulse spacing smaller than T_2. This arises because the Fourier transform of this pair defines a cosine that spans over a bandwidth specified by the inverse of the pulse duration. The optical pumping is achieved by tailoring the comb in a magnetic field of 88 Gauss, thus opening decay avenues to the nuclear Zeeman levels. This method limits the forward recall efficiency (Eq. 2.22) to at most 10% due to the comb finesse $F = 2$.

General spectral features are limited in bandwidth to the ground state splitting as larger bandwidths would reintroduce absorbers into the spectral inteval of interest (i.e. the levels are inhomogeneously broadened). In our approach, we exploit the periodic structure of the comb to avoid this bandwidth limitation. We create a broadband frequency comb by setting the splitting of the excited state Zeeman levels to be equal to the period of the comb and the ground state nuclear Zeeman levels to be half the period of the comb. This allows for accumulation of population into one nuclear Zeeman level (constituing the 'teeth' of the comb), and removal of population from the other Zeeman level (creating the non-absorbing interval between the teeth). One may view this technique as a standard hole burning sequence, where the holes and anti-holes constitute the comb structure. This approach has been explored for photon echoes in Tm:YAG [141].

To generate the 80 MHz wide AFC here, a pair of 20 ns pulses separated by 100 ns was created by the AOM and sent into the medium. To accumulate the grating, we sent 1500 pairs within 3 ms. After waiting 2 ms, either three 20 ns probe pulses were sent into the waveguide, or we sent a 100 μs chirped pulse with chirp rate 1 MHz/μs that was generated by the AOM. Fig. 4.16 depicts storage of the 20 ns pulses and Fig. 4.17 illustrates the measurement of the AFC with optical depth parameters. The sequence

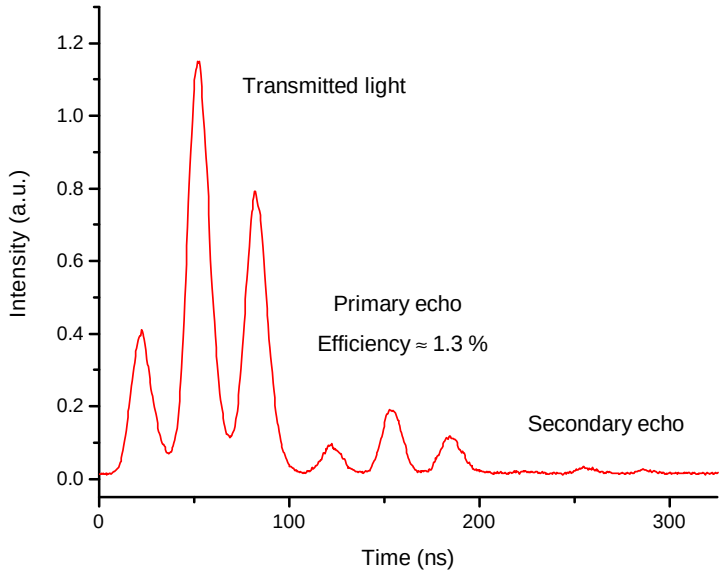

Figure 4.16: Simultaneous storage of three modes of 20 ns duration using an 80 MHz wide AFC. The efficiency is calculated by measuring the optical power ratio of a pulse before the cryostat, and its echo afterwards while removing the attenuation from the 10 dB system loss. Excitation left in the medium allow for a second recall, as seen faintly after the first echoes.

was then repeated to further accumulate population into the Zeeman levels. The the experimental results were averaged 100 times on the oscilloscope to produce Figs. 4.16 and 4.17.

The possibility to store three modes in the AFC is easily seen in Fig. 4.16. The ratio between the pulse width (20 ns) and storage time (100 ns) limits the number of modes to be stored. A second echo is also visible in the figure. Imperfect recall of the primary echo allows for coherences to remain in the medium. If the comb had high and narrow peaks on zero background, this would allow for all the stored energy to be emitted at the first recall.

The comb efficiency η is given by the ratio between the output energy of the pulse and the input pulse energy: $\eta = \frac{E_{input}}{E_{output}}$ where E is the energy of the light. Therefore by measuring the peak power and width of the Gaussian input and output pulses, the efficiency can easily be calculated. The ratio needs to be adjusted by a factor of 10 due

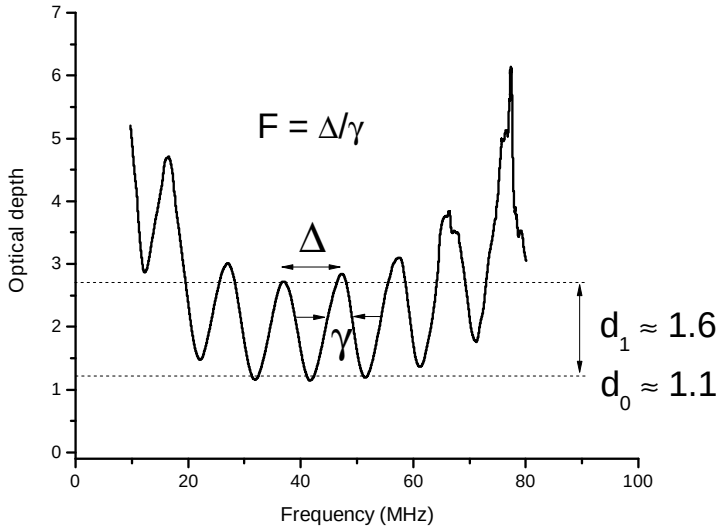

Figure 4.17: Atomic frequency comb absorption profile probed using a 100 μs chirped pulse. A sinusoidal comb is visible with optical depth parameters $d_0 \sim 1.1$, $d_1 \sim 1.6$. This comb predicts a $1.6 \pm 0.6\%$ efficiency (see Eq. 2.22) which is within reasonable agreement with the measured $1.3 \pm 0.3\%$ from a 20 ns probe pulse. The optical depth parameters d_1 and d_0,teeth separation Δ and linewidth γ are shown.

to the cryostat loss to find the efficiency in our measurements. The comb generated here led to a measured efficiency of $1.3 \pm 0.3\%$. This value agrees reasonably well with the one we derive from the optical depth parameters of the comb via Eq. 2.22. To establish depth parameters, the AFC absorption profile shown in Fig. 4.17 was measured using the standard Beer-Lambert law:

$$I_t = 10 I_i e^{-d} \tag{4.6}$$

where I_t and I_i are the transmitted and input light intensities respectively, and d is the optical depth. The factor of ten is included from the cryostat loss. From the AFC, we calculate an efficiency of $1.6 \pm 0.6\%$ using $d_0 \sim 1.1$, $d_1 \sim 1.6$ and a finesse of two (according to the sinusoidal modulation). The finesse is calcuated by the ratio of comb separation Δ to its linewidth γ. The difference in efficiencies between the directly measured and that calculated from the comb absorption profile we attribute to the frequency dependent background absorption. The calculation from the comb absorption assumes a uniform

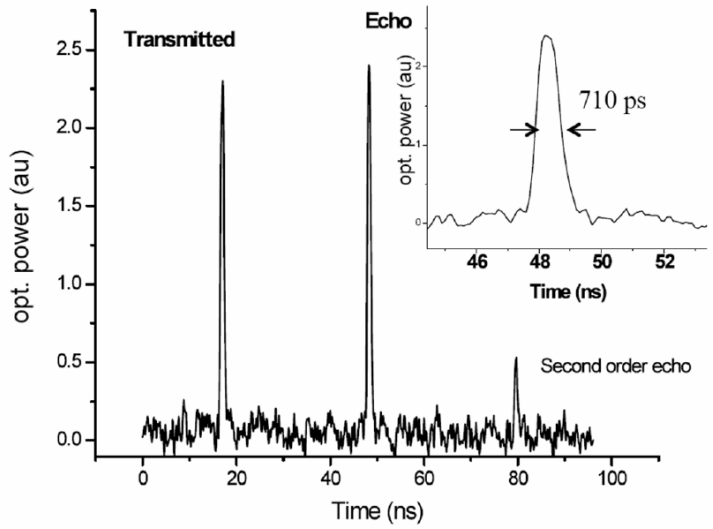

Figure 4.18: 30 ns storage of a 500 ps duration classical pulse in an AFC with ∼4.5% efficiency. Inset: The FWHM of echo pulse is broadened to ∼ 700ps as the comb is not uniform across its entire bandwidth.

comb over the entire spectrum of the 20 ns probe pulse. However, the comb is generated from Gaussian pulses, so the AFC has a spectrum that is modulated by a Gaussian. Thus our 20 ns probe will have frequency components that interact with more background absorption.

To extend the previous experiment to storage of shorter pulses, we prepare the AFC with pairs of ∼ 300 ps duration pulses generated from the PM. Pulse separation is 30 ns in this case, and 1500 pulses are sent during 3 ms. After waiting 2 ms, a 500 ps probe pulse, representing a single classical bit, is sent into the waveguide, resulting in Fig. 4.18. Magnetic field was set to be 133 Gauss to maximize hole burning into the Zeeman levels, hence optimizing efficiency for a shorter 30 ns storage time. The sequence was averaged approximately 100 times on the oscilloscope.

The efficiency increased from the previously discussed case to ∼ 4.5% due to the shorter storage time. This results in a larger separation of the teeth in the AFC, and thus lessens the impact of spectral diffusion. We observed that for even shorter storage times < 5 ns , the echo efficiency plateaus under magnetic field application. We believe

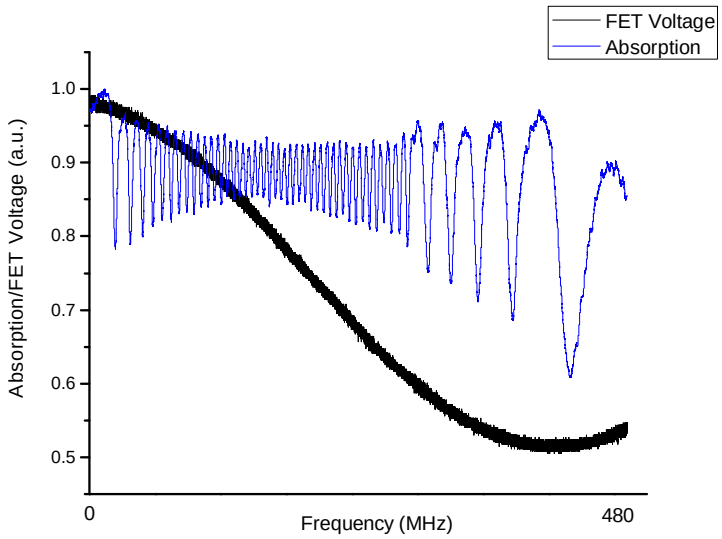

Figure 4.19: Absorption profile of an AFC probed with a 500 MHz frequency scan. The scan voltage, proportional to frequency, is swept using a sinusoidal modulation. The detector's resolution limited observation of comb depth in the most linear region of the scan.

this is due to two long term storage mechanisms, with level spacings, possibly from superhyperfine splitting, that depend differently on magnetic field intensity.

As shown in the figure inset the echo broadens to 700 ps. This is attributed to the non-uniform comb structure across the spectrum. We expect the comb to have its best efficiency at the grating center where the ratio of reversible to irreversible absorption to be the largest, and tapering off at higher bandwidths, similar to measurements with 20 ns preparation pulses.

To further examine comb broadbandness, the AFC was probed by chirping the laser frequency directly through diode current modulation via a field effect transistor (FET). This method limits a scan range to 500 MHz before the laser mode hops. The absorption profile from this scan is presented in Fig. 4.19. A clear comb structure is seen that extends to the limits of the scan, thus verifying some broadbandness. In this measurement, we were not able to accurately measure the absolute optical depth.

4.3.3 Time-bin qubits

As introduced in chapter one, a time-bin qubit represents a basic unit of quantum information. Before we proceed further, we must first discuss how time-bin qubits are generated and measured as to properly interpret further results.

The quantum state of a time-bin qubit can be written as

$$|\psi\rangle = \alpha|\mathrm{t}_0\rangle + \beta \mathrm{e}^{i\phi}|\mathrm{t}_1\rangle \tag{4.7}$$

where α and β are real amplitudes of the time-bins centered at t_0 and t_1 respectively, and the coherence is quantified by the phase ϕ.

A time-bin qubit can be created by coupling a single photon in a well defined temporal mode into an unbalanced Mach-Zehnder interferometer. This results in the photon emerging from the interferometer in a superposition of having travelled along the short t_0 and long t_1 arms of the interferometer. These times may also be referred to as 'early' and 'late' respectively. The state amplitude is adjusted by setting the ratio of the first beamsplitter in the interferometer (assuming the second one to be 50:50) and the relative phase is set by adjusting the phase in one arm of the interferometer. Interestingly, a time-bin qubit can also be created in a photon echo based quantum memory using AFC. By sending a single photon into a memory whose inhomogeneous line has been tailored into a superposition of two AFCs, the photon can be recalled in a superposition of two temporal modes. By adjusting the weights of the gratings (i.e. the amount of reversible absorption contributing to a particular recall time), and the phase (determined by the relative frequency offset of the combs) an arbitary time-bin qubit can be created.

To measure a time-bin qubit, a Mach-Zehnder interferometric setup is used in reverse as depicted in Fig. 4.20. By setting the appropriate delay and phase, this allows interfering the early and late modes on the output port. This corresponds to a projection measurement in the basis defined by amplitude transmissions through the two arms and

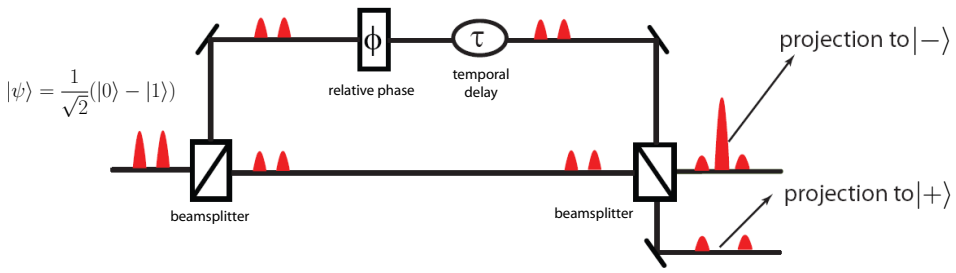

Figure 4.20: A Mach-Zehnder interferometric setup used to perform projection measurements onto time-bin qubit states. The phase and amplitude of the projection is controlled by setting the phase in one arm of the interferometer and controlling the ratio of the first beamsplitter respectively.

the relative phase of the interferometer. For time-bin qubit states lying in the equator of the Bloch sphere, the interference fringes go through maximum and minimmum if a 50:50 beamsplitter is used. In this configuration, if the phase of the interferometer is changed, then a sinusoidal *visibility* curve is generated through the extreme interference points. Conversely, if the interferometer phase is fixed and the qubit phase is changed, then the same curve can be swept out. As for qubit generation, time-bin qubit analysis can be performed in an AFC quantum memory. Using two superimposed AFCs, a stored time-bin qubit can be recalled such that the early and late bins interfere. By changing the relative phase of the AFCs, a visbility curve can be generated. This analysis technique is advantageous as it allows for precise and stable control of the phase, without a bulky interferometric setup requiring stability and alignment. Such a technique also allows for higher dimensional data processing [25].

4.3.4 Broadband storage of qubits

In this section, we extend the previous measurement further to storage of time-bin qubits of 500 ps mode duration encoded into attenuated laser pulses of < 0.4 photons per qubit. To do this, the pumping sequence and wait time remained the same as during the storage of broadband classical pulses. To probe the memory, we generated 1500 qubits with time

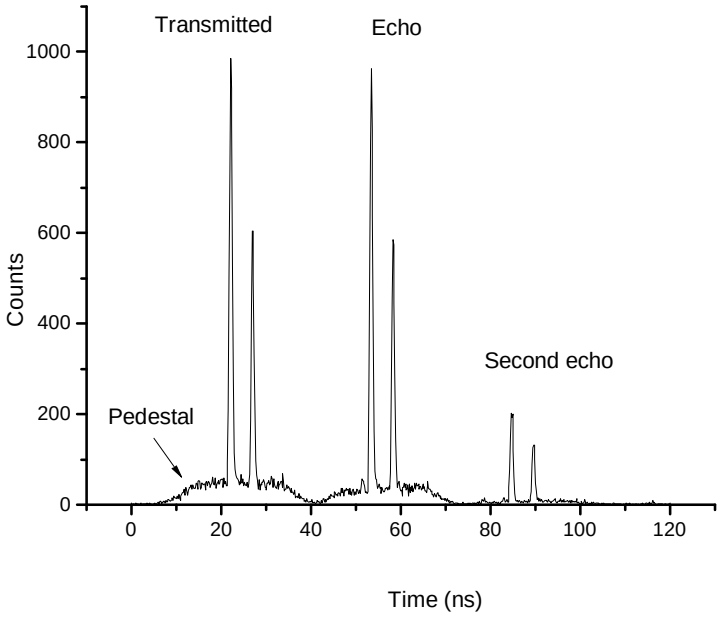

Figure 4.21: Storage of 500 ps duration time-bin qubits with less than 0.4 photons per qubit. The efficiency is $\sim 4.5\%$ for 30 ns storage time. The pedestal is due to voltage drift of the PM.

duration of 500 ps in 3 ms. To do this classical light was sent to the optical attenuators that were pre-calibrated to give 0.4 photons per pulse (of highest intensity) before the cryostat. For this qubit, we set the later time-bin to have an amplitude 60% that of the earlier bin. In this configuration, the optical switches were activated to allow transmission of pump and probe light into the memory, and to direct the pump into the photodiode and probe into the SPD. Measurements of the probe counts were taken over 3 minutes. The results are shown in Fig. 4.21.

When comparing with the results from storage of classical pulses, we find a similarly high signal-to-noise ratio. This demonstrates the versatility of the AFC quantum memory being used for both quantum and classical storage. The only difference is the 'pedestal' which accompanies the pulses here. Due to temperature dependent polarization drift from the PM, we could not constantly maintain a high extinction ratio over the measurement duration. Thus the AOM was gated for 20 ns during the time the PM creates the qubit to extinct DC light around the qubit. Here the echo duration is slightly smaller than 1 ns,

but measured to be slightly broader than the classical case due to detection jitter of the SPD. Nonetheless, storage of these pulses indicate the presence of a ~ 1 GHz broadband AFC.

Storage efficiency was the same here in the quantum case as in the classical case. This can be seen from the echo to transmitted intensity ratio. This ratio R gives information about finesse and optical depth of the comb [41]:

$$R = \frac{\mathrm{e}^{(-\mathrm{d}_0-\mathrm{d/F})}}{(\mathrm{d/F})^2\mathrm{e}^{(-\mathrm{d/F}-7/\mathrm{F}^2-\mathrm{d}_0)}} = (\mathrm{F/d})^2\mathrm{e}^{7/\mathrm{F}^2} \tag{4.8}$$

where the numerator is the probability for light to be transmitted through the comb, while the denominator quantifies the echo efficiency. The finesse is two here so the reversible aborption d is unchanged from the classical case, and because the overall optical depth is the same, the background d_0 is the same. Thus the efficiency here is identical to the classical case. Roughly speaking, the ratio alone gives information about effective reversible absorption which indicates a more or less efficient comb.

4.3.5 Storage fidelity of sub-ns time-bin qubits

As indicated in Chapter 1, high storage fidelity is a necessary component to construct a quantum memory viable in a quantum repeater. We test a large variety of input qubit states in this work to verify that indeed the AFC achieves high fidelity storage of time-bin qubits (i.e. preserves phase and amplitude information). To assess faithful storage of the amplitude information, we first store the so-called 'pole states' on the Bloch sphere. The fidelity F is assessed from this measurement (e.g. comparison of counts in the early bin if early is sent, and vice versa). This measurement allows calculation of the fidelity since a qubit can be written as a statistical mixture of the 'correct' state $|\psi\rangle$ with fidelity F or its orthogonal state $|\psi^{\perp}\rangle$ with probability $1 - F$:

$$\rho = F|\psi\rangle\langle\psi| + (1-F)|\psi^{\perp}\rangle\langle\psi^{\perp}|. \tag{4.9}$$

To probe the coherence preservation, two AFC are created simultaneously, allowing to recall a time-bin qubit in a superposition of two different times. This leads to interference, and from the resultant interference pattern a fidelity is assessed. These two measurements provide the average fidelity of the memory.

Our laboratory generally works with time-bin qubits having 1.44 ns separation between each bin. In this work, we increase the separation between the bins to 30 ns. This allows to control the phase of the qubit using the AOM (i.e. change the phase of the driving voltage) since the AOM rise time is limited to 10 ns. In addition, increasing this separation allows for eliminating the pedestal background, which is merely a technical limitation, impacting the measurement. To account for this increased separation, the storage time was increased to 65 ns. For this, the magnetic field was decreased to 100 Gauss. This experiment uses the same pulse sequence (3 ms burning, 2 ms waiting, 3 ms probeing, repeat) and input pulse duration (500 ps) as before.

High-fidelity storage of amplitude information

Figure 4.22 presents the measurements of the time resolved detection events where we send either $|t_0\rangle$ or $|t_1\rangle$ and look at the detection time. The fidelity is calculated by taking the ratio of the probabiliy P of counts appearing in the correct bin to the sum of probabilities of counts in both bins. Thus the fidelity can be calcualted for the early amplitude as:

$$F = \frac{P_{early}}{P_{early} + P_{late}} = \frac{N_{early}}{N_{early} + N_{late}} \tag{4.10}$$

where N represents the number of counts in the denoted bin. The fidelity for the late amplitude input is calculated similarly. We find $F_{early} = 0.989 \pm 0.01$ and $F_{late} = 0.994 \pm 0.01$ which are both larger than the values 2/3 and the 5/6 for the quantum-classical limit and optimal symmetric universal cloning machine, respectively.

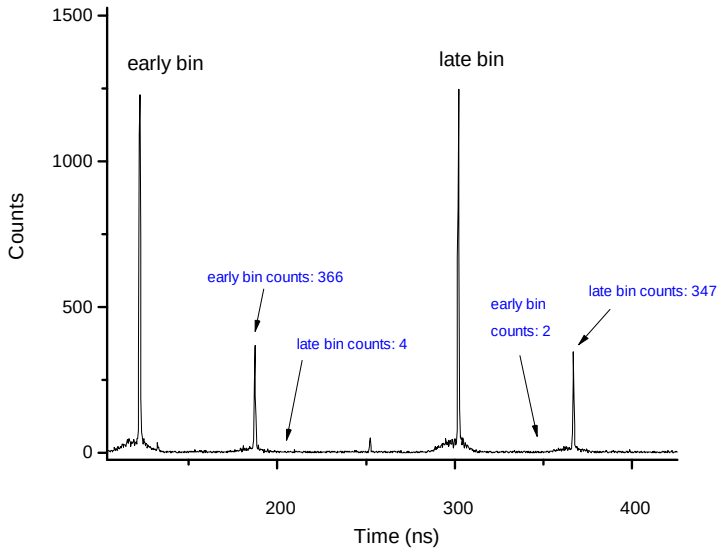

Figure 4.22: Storage of time-bin qubit basis states only (i.e. early and late states). By comparing the number of correct counts to the overall counts in each bin, the average storage fidelity is calcuated to be $F = 0.992 \pm 0.01$. The early and late modes are separated by 30 ns.

High-fidelity storage of superposition states

To probe the coherence preservation of the memory, we use projection measurements to assess the fidelity of time-bin qubits. By coherently splitting each time-bin qubit, and superposing the early with the late wavepacket with variable phase, an interference fringe can be seen (e.g. with a Mach-Zehner interferometer). The quality of this interference, denoted by the visibility is directly related to the fidelity of the time-bin qubits. The following paragraphs will introduce explicitly how this fidelity is measured and draw a relationship to how this can be done using the AFC.

The visibility can be calculated from the count rates in the maximum and minimum of an interference fringe as

$$V = \frac{I_{max} - I_{min}}{I_{max} + I_{min}} \tag{4.11}$$

where I is the count rate at the denoted interference extremum. Since the visibility curve

traces a sinusoid, the average visibility can be interpolated using:

$$I_{norm} = 1 + V\cos(\phi) \tag{4.12}$$

where I_{norm} is the count rate normalized to maximum interference and ϕ is the phase setting of the readout. For a qubit prepared in an equally weighted superposition state, the visibility directly determines the quality of this state. The visibility determines the state fidelity through the following relation:

$$F = \frac{1+V}{2} \tag{4.13}$$

In this experiment, the superimposed AFC is generated by setting half the pulse pairs in the 3 ms burning sequence to have 65 ns separation, and the other half to have 95 ns. This results in two storage times: 65 and 95 ns. The visibility curves are generated by changing the relative phase between the 95 ns separated pulse pairs used to generate the comb. This results in generation of the '65 ns comb' where the center frequency of the light is at at a maximum absorption point (phase of zero for a cosine), and the '95 ns comb' is frequency detuned relative to the light frequency. This relative phase shift between the combs is mapped onto the recalled photons. Phase control was achieved using the AWG by changing the phase of the waveforms driving the AOM. Since the optical pumping dynamics are dependent upon magnetic field strength, the field was set to give the same recall efficiency for both combs. We set 95 Gauss for this experiment and the data accumulation time was 3 minutes.

For a first interference experiment, a double AFC is generated with a relative phase difference of zero. This corresponds to a projection onto the state $\frac{1}{\sqrt{2}}|\mathrm{t}_0\rangle + \frac{1}{\sqrt{2}}|\mathrm{t}_1\rangle$. Four states having 0.4 photons per qubit were sent: $\frac{1}{\sqrt{2}}|\mathrm{t}_0\rangle + \frac{1}{\sqrt{2}}|\mathrm{t}_1\rangle$, $\frac{1}{\sqrt{2}}|\mathrm{t}_0\rangle - \frac{1}{\sqrt{2}}|\mathrm{t}_1\rangle$, $\frac{1}{\sqrt{2}}|\mathrm{t}_0\rangle + i\frac{1}{\sqrt{2}}|\mathrm{t}_1\rangle$, and $\frac{1}{\sqrt{2}}|\mathrm{t}_0\rangle - i\frac{1}{\sqrt{2}}|\mathrm{t}_1\rangle$. The resultant transmitted and echo sequence is depticted in Fig. 4.23.

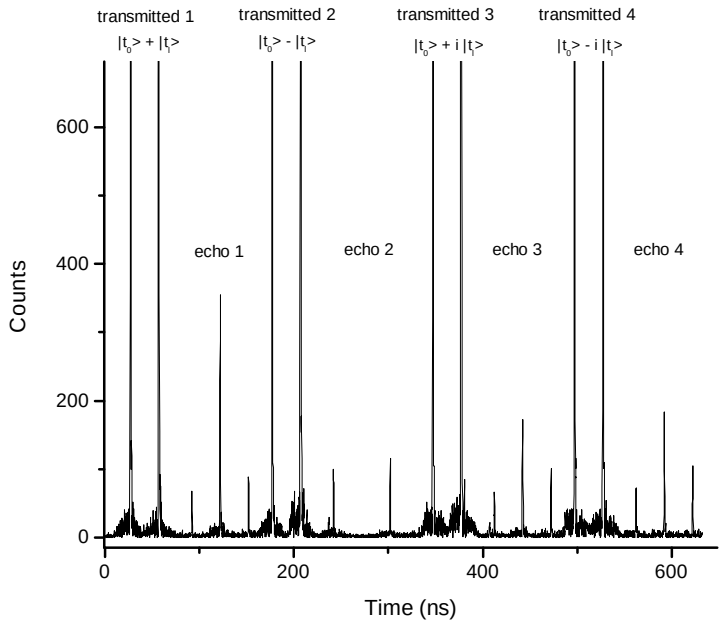

Figure 4.23: Transmitted and echo pulses from four input states indicated on top of the pulse sequence. The state amplitudes are equal so are removed in the labels for clarity. Two superimposed AFCs are used to generate storage times of 35 and 65 ns. This is equivalent to a projection measurement onto the state $\frac{1}{\sqrt{2}}|t_0\rangle + \frac{1}{\sqrt{2}}|t_1\rangle$. Probabilities for input states to project onto this state are given by the counts in the middle, interfering, echo bin.

The interference in the centre bin gives information about the projection measurement. Since the projection measurement is in the same direction on the Bloch sphere as the first input state, maximum counts are seen in the center bin here. Thus the projection of the state is maximal. Conversely, the second input (orthogonal) state produces an interference minimum. Therefore this state has a small probability to project onto $\frac{1}{\sqrt{2}}|\mathrm{t}_0\rangle + \frac{1}{\sqrt{2}}|\mathrm{t}_1\rangle$. The last two inputs both have a 50% chance of projecting onto this state resulting in center bin counts in between maximum and minimum, and being the same for both states. The unequal heights of the side peaks, denoting projections onto explicitly early and late, is due a magentic field slightly weighting the later recall and a relatively short data acquisition time (longer time would average the counts in both bins).

To calculate the fidelity, we then examine only interference from the first two states shown in Fig. 4.23: $\frac{1}{\sqrt{2}}|\mathrm{t}_0\rangle + \frac{1}{\sqrt{2}}|\mathrm{t}_1\rangle$, and $\frac{1}{\sqrt{2}}|\mathrm{t}_0\rangle - \frac{1}{\sqrt{2}}|\mathrm{t}_1\rangle$. The relative phase of the gratings are varied in steps of 15° and the number of counts in the center, interfering, bin is recorded and plotted against the phase. Results from this measurement are shown in Fig. 4.24.

We fit each of the curves using Eq. 4.12 giving a visibility of $V_+ = 0.964 \pm 0.03$ and $V_- = 0.974 \pm 0.06$. This results in an average fidelity of 0.985 ± 0.02 that exceeds both the quantum-classical bound and that set by the optimal symmetric universal cloner, and closely matches the fidelity extracted from the time-bin qubits in the early or late states. This results in an overall average qubit storage fidelity of $\frac{1}{3}(\frac{1}{2} \times 0.989 + \frac{1}{2} \times 0.994) + \frac{2}{3}(\frac{1}{2} \times 0.964 + \frac{1}{2} \times 0.974) \approx 98\%$. This confirms the high quality storage mechanism of a quantum memory using atomic frequency combs in this material.

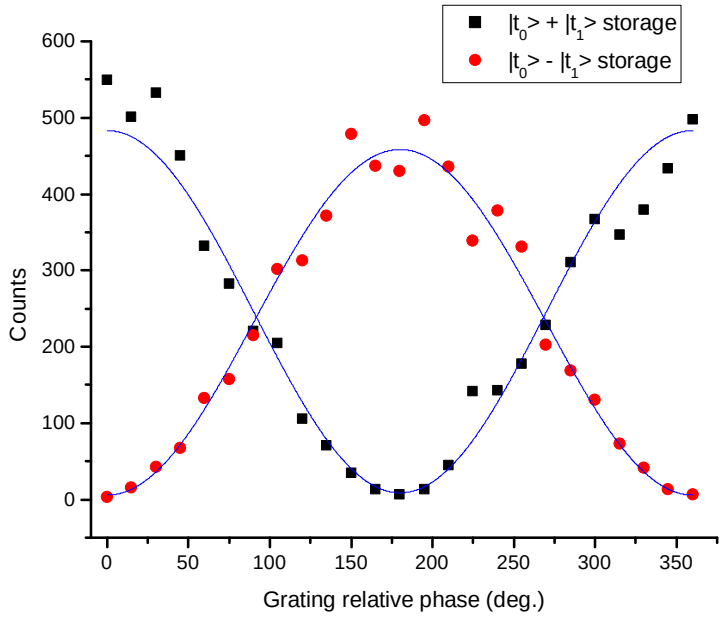

Figure 4.24: Interference fringes generated by varying the relative phase of the gratings for the input states $\frac{1}{\sqrt{2}}|t_0\rangle + \frac{1}{\sqrt{2}}|t_1\rangle$, and $\frac{1}{\sqrt{2}}|t_0\rangle - \frac{1}{\sqrt{2}}|t_1\rangle$.

4.3.6 Multimode storage of 128 faint pulses

Multimode memories are an important requirement for decreasing the time it takes to establish entanglement in a quantum repeater. Up to now, 64 modes at the single photon level have been stored simultaneously [138]. In this section, the multimode capabilities of our sample is demonstrated by storing 128 temporal modes of 0.4 photons per mode for 256 nanoseconds. The broadbandness of the comb and our ability to create short pulses allowed for such a demonstration.

We generate the AFC using the same experimental configuration as in the broadband single qubit storage except the pairs were separated by 256 ns (the magnetic field was adjusted to 88 Gauss) and the probe constituted 128 modes with 1 ns duration and separation of 2 ns. Fig. 4.25 presents the photon echoes produced from storing 128 modes in the AFC. In principle, this setup has the capability to easily double the number of modes stored (0.5 ns per pulse with 0.5 ns separation), however the timing jitter of the silicon SPD caused a reduced resolution of the stored pulse train. Notice the storage

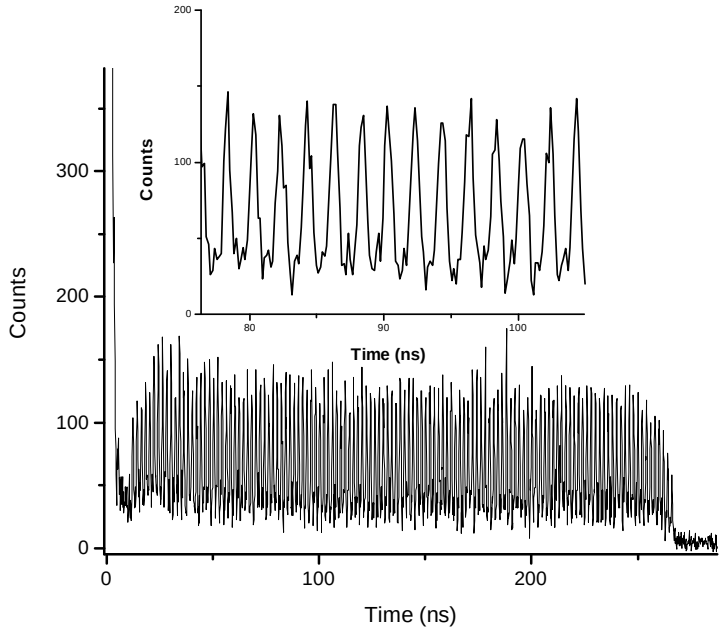

Figure 4.25: Photon echoes from storage of 128 modes of 0.4 photons per pulse in the waveguide. Here the maximum number of stored modes is limited to SPD jitter. Inset: Zoomed in shot of the stored pulses. This shows that each pulse is easily resolvable.

efficiency is quite low ($< 1\%$) for this storage time.

As a practical example of the multimode storage, sixteen 8-bit characters replaced the 128 modes in this experiment. The results are shown in Fig. 4.26. This indicates the versatility of the memory for classical data processing or simultaneous storage of qubits for synchronization in a quantum repeater or computing scheme.

4.3.7 Conclusion

To conclude, this experiment has established the potential for Ti:Tm:$LiNbO_3$ waveguides as a candidate material for a quantum memories in quantum repeaters. Using weak pulses containing 0.4 photons per qubit, we demonstrated an average (post-selected) storage fidelity of 98% which is an essential requirement for a quantum memory. This work also extends the current bandwidths of quantum memories from 100 MHz to $\sim$1 GHz. As an essential requirement to increase entanglement distribution rates in a quantum repater,

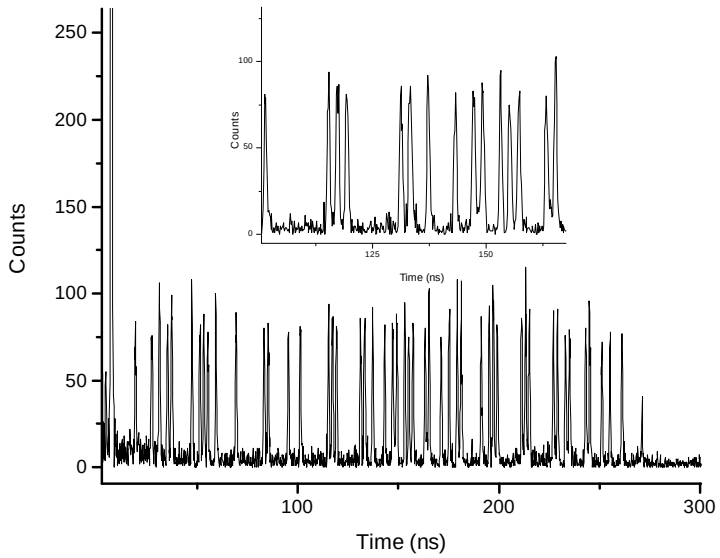

Figure 4.26: Echoes produced from storing weak pulses encoding sixteen 8-bit characters. Inset: A close-up displays that the pulses are easily resolvable.

we demonstrate simultaneous storage and recall of 128 temporal modes in the atomic frequency comb, doubling the current benchmark. Our results demonstrate the viability of a thulium doped waveguide for use as a integrated quantum memory for quantum networks. Current investigations aim to increase the efficiency by optimization of optical pumping, or using radio-frequency fields for spin-mixing in the excited state, thereby increasing the branching ratio into the ground states. In addition, we aim to increase the storage time by examining possibilities to map optical coherence into a longer lived level.

Chapter 5

Summary and outlook

Quantum communication relies on encoding information into quantum states of light, which can be used to perform tasks, like provable secure key distribution, that is classically unfeasible. To date, quantum communication links are bound to distances of a hundred kilometers or so. To extend this distance, quantum repeaters have been proposed, which include reversible transfer of quantum states between light and matter as a central ingredient. Hence, the construction of a robust quantum memory is a necessary step for future applications of quantum communication. It allows for the synchronization of quantum data, which is important for quantum computing, quantum repeaters, and quantum networking. Focusing on two experiments, this thesis highlights important steps to creating a practical quantum memory for quantum communication.

In the first experiment, a novel material candidate, a Ti:Tm:$LiNbO_3$ waveguide, was spectroscopically investigated at a temperature of 3 Kelvin. This rare-earth-ion doped crystal combines a desirable level structure and good coherence properties for photon echo quantum memory with waveguide functionality for an integrated approach. We quantified atomic level structure, important decoherence mechanisms, as well as effects arising from the application of external electric and magnetic fields. This provides the basis for subsequent implementations of photon echo quantum memory protocols. The investigation revealed previously unknown material properties and generated questions to be addressed in future investigations.

With the result of this characterization at hand, we were able to implement a quantum memory protocol based on atomic frequency combs at the single photon level. In this second experiment, we extended the current benchmarks on material storage bandwidth

from 100 MHz beyond 1 GHz, the multimode storage capacity from 64 to 128 temporal modes, and we confirmed the quantum nature of our memory through a notably high fidelity of 98 %. This experiment motivates additional spectroscopic studies as well as further investigations of optical pumping strategies.

The results from these two experiments provide the foundations for a large amount of future work. Experiments pertaining to spectroscopic material studies include the following:

- Quantification of the Rabi frequency in Ti:Tm:$LiNbO_3$.
- Determining the origin and the magnetic field dependence of the sub-level structure in the material. A method to address this question is the measurement of holes and anti-holes.
- Further spectroscopy under various magnetic fields and temperatures, including the investigation of these parameters on spectral diffusion.
- Determining the roles of the $^3H_5$ and $^3F_4$ levels in thulium for population relaxation and the generation of persistent spectral holes.
- Additional spectroscopy across the inhomogeneous line. This may lead to understanding of the difference between our results and results recently obtained in a bulk crystal [106] and maybe to improved material parameters for quantum state storage.

Future investigations in terms of the implementations of photon echo quantum memory protocols should specifically focus on increasing the storage efficiency as well on on-demand readout. This includes:

- New samples with varying titanium doping concentrations should be studied, and the possibility to fiber-pigtail the waveguides should be explored. We expect this

to lead to improved coupling loss and to a simplified and more robust experimental setup.

- Investigating radio-frequency spin mixing of population in the excited state that may allow for a more efficient optical pumping into persistent ground state levels.

- Using the waveguide end-faces to create an asymmetric, impedance matched cavity, which can increase efficiencies by tens of percent.

- Optimization of pumping strategies beyond pulse pairs. This includes hole burning sequences or linear frequency chirps [142] to increase the spectral width of the comb. An increased width would allow the reversible mapping of entangled photons generated in the widely employed process of spontaneous parametric down conversion.

- Studying the reversible mapping of optically excited coherence onto the $^3F_4$ electronic level. This may allow read-out on demand in a protocol based on AFC.

- Studying the implementation of CRIB. To facilitate the required electric field control, our collaborators are currently electrodes with a waveguide 'on chip', thus enabling fast electric field switching with small voltages.

We point out that the AFC approach to storage and its connection with interferometry opens new possibilities for state manipulation, similar to investigations reported in [25]. Furthermore, we point out that rare-earth-ion doped crystals are not only interesting for photon echo quantum memory, but also for quantum state storage employing electromagnetically induced transparency and slow light [16]. The combination of both protocols may open new avenues, including a direct Raman transfer of coherence onto ground-state coherence [143].

Bibliography

[1] N. Gisin *et al.*, Rev. Mod. Phys. 74, 145195 (2002).

[2] W. K. Wootters, and W. H. Zurek, Nature (London) 299, 802803 (1982).

[3] C. H. Bennett, and G. Brassard, 1984, in Proceedings of the IEEE International Conference on Computers, Systems and Signal Processing, Bangalore, India, (IEEE, New York), pp. 175179.

[4] I. Lucio-Martinez *et al.*, New J. Phys. 11, 095001 (2009).

[5] A. K. Ekert, Phys. Rev. Lett. 67, 661663 (1991).

[6] A. Einstein *et al.*, Phys. Rev. 47, 777 (1935).

[7] J. S. Bell, Physics 1, 195 (1964).

[8] M. Nielsen and I. L. Chuang. Quantum Computation and Quantum Information. Cambridge, Cambridge UK, (2000).

[9] X. Ma *et al.*, Phys. Rev. A 76, 012307 (2007).

[10] T. Scheidl *et al.* New J. Phys. 11 085002.

[11] C. H. Bennett *et al.*, Phys. Rev. Lett. 70, 1895 (1993).

[12] M. Zukowski *et al.*, Phys. Rev. Lett. 71, 4287 (1993).

[13] D. Bouwmeester *et al.*, Nature 390, 575 (1997).

[14] R. Ursin *et al.*, Nature 430, 849 (2004).

[15] H. Briegel *et al.*, Phys. Rev. Lett. 81, 59325935 (1998).

[16] K. Hammerer *et al.*, Rev. Mod. Phys. 82, 10411093 (2010).

[17] M. Lukin, Rev. Mod. Phys. 75, 457472 (2003).

[18] A. I. Lvovsky *et al.*, Nature Photonics 3, 706 - 714 (2009).

[19] C. Bennett *et al.*, Phys. Rev. Lett. 76, 722725 (1996).

[20] L. Duan *et al.*, Nature 414, 413 (2001).

[21] N. Sangouard *et al.*, arXiv:0906.2699.

[22] C. Simon *et al.*, Phys. Rev. Lett. 98, 190503 (2007).

[23] M. Nilsson *et al.*, Physica Scripta T102, 178-185 (2002).

[24] M. Tian *et al.*, Phys. Rev. A 79, 022312 (2009).

[25] A. Delfan Abazari *et al.*, arXiv.org:0910.2457.

[26] D. N. Matsukevich *et al.*, Phys. Rev. Lett. 97, 013601 (2006).

[27] D. Oblak *et al.*, Phys. Rev. A 71, 043807 (2005).

[28] J. J. Longdell *et al.*, Phys. Rev. Lett. 95, 063601 (2005).

[29] K. F. Reim *et al.*, Nature Photonics 4, 218 - 221 (2010).

[30] M. Mucke *et al.*, Nature 465, 755758 (2010).

[31] J. Nunn *et al.*, arxiv:1007.4444.

[32] R. Young *et al.*, New J. Phys. 9, 365 (2007).

[33] J. Wrachtrup and F. Jelezko, J. Phys.: Condens. Matter 18, S807S824 (2006).

[34] W. Tittel et al. *et al.*, Laser Photon. Rev. doi:10.1002/lpor.200810056 (2009).

[35] R. Cone, Uninversity of Calgary colloquium, March 18 2010.

[36] A. Levine and F. Palilla, Applied Physics Letters, Vol. 5, p.118-120 (1964).

[37] R. M. Macfarlane and R. M. Shelby, in: A.A. Kaplyanskii, R.M. Macfarlane (Eds.), Spectroscopy of Solids Containing Rare Earth Ions, North-Holland, Amsterdam (1987).

[38] U. G. Kopvilem and V. R. Nagibarov, Fiz. Metall. Metalloved 2, 313 (1963).

[39] N. A. Kurnit *et al.*, Phys. Rev. Lett. 13, 567 (1964).

[40] M. Afzelius *et al.*, Phys. Rev. A 79, 052329 (2009).

[41] H. de Riedmatten *et al.*, Nature 456, 773 (2008).

[42] M. Hedges *et al.*, Nature 465, 10521056 (2010).

[43] C. Simon *et al.*, European Physical Journal D 58: 1 - 22 (2010).

[44] F. Bussières *et al.*, Opt. Express 16, 17060-17069 (2008).

[45] S. Massar and S. Popescu, Phys. Rev. Lett. 74, 12591263 (1995).

[46] V. Scarani *et al.*, Rev. Mod. Phys. 77, 12251256 (2005).

[47] N. Sangouard *et al.*, Phys. Rev. A 81, 062333 (2010).

[48] R. M. Macfarlane and R. M. Shelby, in *Persistant Spectral Hole Burning: Science and Applications*, edited by W.E. Moerner, Springer (1988).

[49] R. Griffiths, Elements of Electromagnetics, Prentice-Hall (1999).

[50] P. Meystre and M. Sargent, Elements of Quantum Optics, Springer-Verlag (1989).

[51] T. Bottger, PhD Thesis, Bozeman State University, 2002.

[52] W. E. Moerner *et al.*, Persistent spectral hole-burning: Science and applications, Moerner, W. E. (Ed.), Springer-Verlag, Berlin (1988).

[53] A. J. Meixner *et al.*, J. Chem. Phys. 91, 6728-6736 (1989).

[54] E. S. Maniloff *et al.*, Chem. Phys. 193, 173 (1995).

[55] S. Hastings-Simon, PhD Thesis, University of Geneva, 2008.

[56] A. Louchet *et al.*, Phys. Rev. B 75, 35131 (2007).

[57] R. Macfarlane, J. Lumin. 125, 156 (2007).

[58] A. Szabo, Frequency selective optical memory, U.S. Patent No. 3,896,420 (1975).

[59] J. J. Longdell and M. J. Sellars, Phys. Rev. A 69, 032307 (2004).

[60] D. Allen and J. Eberly, Optical resonace and two-level atoms, Wiley, New York (1975).

[61] W. H. Hesselink, and D. A. Wiersma, Phys. Rev. Lett. 43, 1991 (1979).

[62] J. Ruggiero *et al.*, Phys. Rev. A 79, 053851 (2009).

[63] R. H. Dicke, Phys. Rev. 93, 99 (1954).

[64] T. Mossberg, Opt. Lett. 7, 77 (1982).

[65] M. Mitsunaga *et al.*, Opt. Lett. 16 (4), 264 (1991).

[66] M. Afzelius *et al.*, Phys. Rev. Lett. 104, 040503 (2010).

[67] M. Afzelius *et al.*, Phys. Rev. A 82, 022310 (2010).

[68] S. Moiseev *et al.*, arXiv:1004.1370.

[69] S. A. Moiseev, and S. Kröll, Phys. Rev. Lett. 87, 173601 (2001).

[70] M. Nilsson, and S. Kröll, Opt. Comm. 247, 292 (2005).

[71] A. Alexander *et al.*, Phys. Rev. Lett. 96, 043602 (2006).

[72] B. Kraus *et al.*, Phys. Rev. A. 73, 020302(R) (2006).

[73] G. Hetet *et al.*, Phys. Rev. Lett. 100, 023601 (2008).

[74] A. Alexander, PhD Thesis, Australian National University, 2007.

[75] US geological survey <http://pubs.usgs.gov/fs/2002/fs087-02/>

[76] A. J. Freeman and R. E. Watson, Phys. Rev. 127, 20582075 (1962).

[77] B. R. Judd, Phys. Rev. 127, 750 (1962).

[78] K. H. J. Buscchow (1998) Permanent-Magnet Materials and their Applications, Trans Tech Publications Ltd., Switzerland.

[79] R. Yano *et al.*, Opt. Lett. 16, 1884-1886 (1991).

[80] R. S. Meltzer, in Spectroscopic Properties of Rare Earths Optical Materials, G. Liu and B. Jacquier Eds., Springer (2005).

[81] T. Böttger *et al.*, Phys. Rev. B 73, 075101 (2006).

[82] R. Macfarlane, Opt. Lett. 18 (22), 1958 (1993).

[83] D. R. Taylor and J. P. Hessler, Phys. Lett. A A50, 205-207 (1974).

[84] F. Konz *et al.*, Phys. Rev. B 68, 085109 (2003).

[85] M. Ohlsson *et al.*, Opt. Lett. 28, 450 (2003).

[86] O. Guillot-Noël *et al.*, Phys. Rev. B 71, 174409 (2005).

[87] P. Goldner *et al.*, Opt. Materials 28, 649 (2006).

[88] F. de-Seze *et al.*, Phys. Rev. B 73, 85112 (2006).

[89] A. Louchet *et al.*, Phys. Rev. B 77, 195110 (2008).

[90] S. A. Moiseev and W. Tittel, Phys. Rev. A 82, 012309 (2010).

[91] See group website <http://fb6www.uni-paderborn.de/ag/ag-sol/>

[92] M. Quintanilla *et al.*, Optical Materials 30, 1098-1102 (2008).

[93] See company website <http://www.thorlabs.com/>

[94] See company website <http://www.ozoptics.com/>

[95] P. Horowitz and W. Hill, The Art of Electronics 2d Edition. Cambridge, Cambridge UK (1989).

[96] See PerkinElmer single photon counting modules <http://optoelectronics.perkinelmer.com>

[97] N. Sinclair *et al.*, J. Lumin. 130(9), 1586 (2010).

[98] P. J. Kwiat *et al.*, Phys. Rev. Lett. 75 4337 (1995).

[99] G. Ribordy *et al.*, Phys. Rev. A 63, 012309 (2001).

[100] M. Halder *et al.*, Opt. Express 17, 4670 (2009).

[101] J. Slater *et al.*, arXiv:0908.3516.

[102] J. Gruber *et al.*, Phys. Rev. B 40, 9464 (1989).

[103] M. Tian *et al.*, J. Opt. Soc. Am. B 18, 673 (2001).

[104] L. Núñez *et al.*, J. Lumin. 55, 253 (1993).

[105] E. Cantelar *et al.*, J. Lumin. 128, 988 (2008).

[106] C. Thiel *et al.*, J. Lumin. 130, 9 (2010).

[107] D. N. Nikogosyan, Nonlinear Optical Crystals: A Complete Survey, Springer, (2005).

[108] R. K. Mohan *et al.*, J. Lumin. 127, 116 (2007).

[109] C. W. Thiel *et al.*, Workshop on the Storage and Manipulation of Quantum Information in Optically-Addressed Solids, January 2008, Bozeman, Montana.

[110] S. R. Hastings-Simon *et al.*, Opt. Comm. 266, 716 (2006).

[111] V. Dierolf *et al.*, Appl. Phys. B 72, 803 (2001).

[112] Y. Sun *et al.*, J. Lumin. 98, 281 (2002).

[113] M. Colice *et al.*, Appl. Opt. 45, 6393 (2006).

[114] Y. N. Korkishko *et al.*, Appl. Opt. 35, 7056 (1996).

[115] R. V. Schmidt and I. P. Kaminov, Appl. Phys. Lett. 25, 458 (1974).

[116] E. L. Wooten *et al.*, IEEE J. Sel. Top. Quant. Electron 6, 1 (2000).

[117] T. Chanelière *et al.*, arXiv:0902.2048.

[118] T. Chanelière *et al.*, arXiv:0911.3328.

[119] M. Staudt *et al.*, Phys. Rev. Lett. 98, 113601 (2007).

[120] M. Staudt *et al.*, Phys. Rev. Lett. 99, 173602 (2007).

[121] R. Regener and W. Sohler, Appl. Phys. B 36, 143 (1985).

[122] L. F. Johnston and A. A. Ballman, J. Appl. Phys. 40, 297 (1969).

[123] E. Cantelar *et al.*, Physica Scripta T118 69 (2005).

[124] D. A. Davids and P. E. Wagner, Phys. Rev. Lett. 12, 141 (1964).

[125] G. H. Larson and C. D. Jeffries, Phys. Rev. 141, 461 (1966).

[126] I. N. Kurkin and K. P. Chernov, Physica B & C 101, 233 (1980).

[127] S. R. Hastings-Simon *et al.*, Phys. Rev. B 77, 125111 (2008).

[128] S. R. Hastings-Simon *et al.*, Phys. Rev. B 78, 085410 (2008).

[129] B. Lauritzen *et al.*, Phys. Rev. A 78, 043402 (2008).

[130] G. Gorju *et al.*, J. Phys.: Condens. Matter 19, 386226 (2007).

[131] M. Nilsson *et al.*, Phys. Rev. B 70, 214116 (2004).

[132] N. Sangouard *et al.*, Phys. Rev. A 75, 032327 (2007).

[133] W. B. Mims *et al.*, Phys. Rev. 123, 2059 (1961).

[134] Y. S. Bai and M. D. Fayer, Phys. Rev. B 39, 11066 (1989).

[135] W. Mims, Phys. Rev. 168, 370 (1968).

[136] M. Staudt *et al.*, Opt. Comm. 266, 720 (2006).

[137] M. Quintanilla *et al.*, J. Lumin. 128, 927 (2008).

[138] I. Usmani *et al.*, Nature Comm. 1, 12 (2010).

[139] B. Lauritzen *et al.*, Phys. Rev. Lett. 104, 080502 (2010).

[140] X.-M. Jin *et al.*, arXiv:1004.4691.

[141] M. Bonarota *et al.*, arXiv:0911.4359.

[142] R. Reibel *et al.*, J. Lumin. 98, 355365 (2002).

[143] S. A. Moiseev and W. Tittel, arXiv:0812.1730.